Characterization and Through Process Modelling of Large Strain Phenomena for Aluminum Alloys at Room and Elevated Temperatures

Usman Ali

A thesis

presented to the University of Waterloo

in fulfillment of the

thesis requirement for the degree of

Doctor of Philosophy

in

Mechanical and Mechatronics Engineering

Waterloo, Ontario, Canada, 2017

I hereby declare that I am the sole author of this thesis. This is a true copy of the thesis, including any required final revisions, as accepted by my examiners.

I understand that my thesis may be made electronically available to the public.

Abstract

The objective of this research is to model and analyze large strain problems (rolling, hot compression) in FCC polycrystals. In the first part of this research, a rate-dependent crystal plasticity based Element Free Galerkin (CPEFG) model was incorporated in commercial software LS-DYNA to simulate cold rolling of AA 5754. Unlike classical Finite Element Methods, EFG methods are meshless and hence can accommodate large strains. It is well known that rolling produces inhomogeneous microstructure in the through thickness of the sheet. Therefore CPEFG model used in this work accounted for the complete through thickness microstructure in the sheet. Through thickness deformed microstructure and strain distribution obtained from CPEFG simulations were validated with published results.

CPEFG simulations provide elemental texture data which can provide insight into the microstructural changes during processing. Therefore, an in-house 3D framework (gCode) was developed. In-house gCode is based on a path finding algorithm and calculates the element neighbors to analyze subgrain formation and other grain metrics. Initial and final grain size in CPEFG rolling simulations was found using the gCode and validated against published experimental data. Results show a marked reduction in subgrain formation down the sheet thickness due to the reduction in shear. Further analysis showed that there was a 8 μm change in grain size between the initial and deformed sheet. However, there was a 7 μm change in grain size between the top and center of the deformed sheet. Thus highlighting the importance of capturing the complete microstructure of the sheet. In-house gCode was also used to study the relationship of grain size and texture across the sheet thickness. It is observed that small grains near the center of the sheet prefer Brass, S and Copper while large grains near the center of the sheet prefer Cube, S and Copper.

Plane strain compression is often used to model cold rolling. Therefore, plane strain compression simulations were also performed and predictions from both simulations were compared. Volume fraction evolution of several texture components from the center section of the sheet show similar values between the two processes However, normal strains, shear strains and microstructure evolution near the top section show considerable difference between the two processes. Hence, highlighting the importance of using proper microstructure and boundary conditions for rolling simulations.

The second part of this work focuses on through process modelling of hot compression of cast AA 6063. A Taylor based rate-dependent polycrystal crystal plasticity framework was used to predict the texture and stress-strain evolution at various temperatures (from 400^0C to 600^0C) and strain-rates (from 0.01 s^{-1} to 10 s^{-1}). Crystal plasticity framework was modified to incorporate the effects of temperature and strain-rate. Proposed framework was calibrated, verified and validated with experimental AA 6063 hot compression Gleeble data. Simulated stress-strain results for all temperatures and strain-rates showed good agreement with experimental results. It is known that AA 6xxx alloys undergo static recrystallization at high temperatures. Therefore, a probabilistic integration point based static recrystallization (SRX) code was developed to study the texture and grain size evolution at various temperatures and strain-rates. SRX model used texture and resolved shear stress as inputs to calculate potential nuclei and their growth. After SRX simulations, experimental and simulated texture and grain size results were compared and showed good agreement with minor deviations at different temperatures and strain-rates and also predicted the correct trends.

Acknowledgements

This work was supported by the Natural Sciences and Engineering Research Council - Automotive Partnership Collaboration (NSERC-APC) Program and General Motors of Canada. I would also like to acknowledge the High Performance Computing Center at the University of Sherbrooke.

I would like to thank my supervisor Prof. Kaan Inal for his constant help, guidance and support throughout my PhD. I would like to thank Dr. Abhijit Brahme for his help in creating synthetic microstructures and helpful discussions and guidance throughout my PhD. I would like to thank Dr. Raja K. Mishra of General Motors Research and Development Center for helpful discussions and technical expertise. I would also like to thank Dr. Sugrib Kumar Shaha for helping with 2D X-Ray Diffraction experiments, Daniel Odoh for helping me with experiments and Waqas Muhammad for helpful discussions and experimental data. I would also like to thank Dr. Jonathan Rossiter, Dr. Dariush Ghaffari Tari, Dr. Reza Bagheriasl, Prof. Hamid Jahedmotlagh, Prof. Mohsen Mohammadi, Prof. Sanjeev Bedi, Prof. Naveen Chandrashekar, Prof. Michael Worswick, Dr. Jose Imbert, Dr. Ricardo Lebensohn, Ed Cyr, Reza Mirimiri and Jaspreet Nagra for their helpful discussions, support and encouragement throughout this journey. I would also like to thank all those who directly or indirectly helped me in completing my PhD.

Lastly, I would like to thank my wife, Safiya and parents for their support and prayers.

Dedication

To the past, present and future

Table of Contents

List of Figures

List of Tables

Nomenclature

F	Deformation gradient
τ_α	Resolved shear stress on slip system (α)
$\dot{\gamma}_{(\alpha)}$	Slip rates on slip system (α)
$g_{(\alpha)}$	Slip system (α) hardness
$h_{(\beta)}$	Single slip hardening
$\emptyset_1, \emptyset, \emptyset_2$	Bunge Euler angles
q_0, q_1, q_2, q_3	Quaternion set
b	Magnitude of burgers vector
t	Time
μ	Shear modulus
ρ	Dislocation density
$\dot{\varepsilon}$	Strain-rate
k	Boltzmann constant
ω_{switch}	Switching parameter
ξ	Random number between 0 and 1
CPFEM	Crystal plasticity finite element model
CPEFG	Crystal Plasticity Element Free Galerkin Model
CA	Cellular automata
JMAK	Johnson Mehl Avrami Kolmogorov
SRX	Static recrystallization
PSC	Plane strain compression
gCode	Grain Analysis Code
FE/FEA	Finite element analysis
AAxxxx	Aluminum alloy xxxx
FCC	Face centered cubic
XFEM	Extended finite element method
IPF	Inverse pole figure

Chapter 1
Introduction

Aluminum alloys are increasingly being used in automotive applications due to their light weight, strength, formability and resistance to corrosion [1, 2]. Use of aluminum results in lighter cars with higher fuel efficiency while still meeting all the safety standards. As fuel costs rise, aluminum alloys provide the same or better cost-to-benefit ratio than steels and therefore are an ideal candidate for automotive industry. Automotive industry has been using aluminum alloys namely; AA 5754, AA 5182, AA 5083 from the early 1980's for various automotive parts. The average net increase in rolled, extruded and die cast parts in automotive industry was around 20 Kg between 2012 and 2015 with the most increase in sheet and extrusions [3]. However, in recent years, many automotive manufacturers have substantially increased the aluminum content in their vehicles. For example, Fiat 500 has around 252 lbs. of aluminum while SUV's like Chevy Suburban use 410 lbs. of aluminum [3].

Automotive manufactures use aluminum for manufacturing of car bodies, enclosures, transmission and subframe components [4]. Recently, Ford has designed the 2015 Ford F-150 Truck with an all aluminum body resulting in over 700 lbs. of weight reduction in saved body weight over previous models. This weight reduction has also led to an improved fuel consumption [3]. Similarly, 2007 Cadillac CTS uses aluminum alloys in chassis applications as a hollow casting/extruded welded cradle [4]. Audi R8, Honda NSX and many other vehicle manufacturers have also used various aluminum alloys for chassis applications [5]. Not only chassis or body, some automotive manufacturers have also used aluminum in transmission components. For example, Ford Motor Company's Lincoln Mark VIII uses aluminum alloys in transmission components and recently even transmission blocks are being manufactured with aluminum alloys [5]. From the examples presented above, it is clear that there is a massive use of aluminum alloys in automotive applications and is expected to more than double in the next 10 years [3].

Use of aluminum sheet and extrusions shows the highest growth for automotive applications [3]. Aluminum sheets are produced from aluminum billets and are used in body panels such as doors, hoods, etc. Similarly, aluminum extrusions are used in body closures and body structures such as chassis, cradle, etc. In addition, use of aluminum sheets in automotive bodies is expected to drive the increase in aluminum content in automotive vehicles by 2025 [3]. As use of aluminum sheets and

extrusions increases, designers need to consider various parameters during sheet forming and extrusion processes to optimize and increase the efficiency of these processes.

To date, experimentation is the most common design approach for material and process characterization [4]. However, as experimental methods consume time and resources, there is an ever increasing need of numerical models to characterize material behavior to save experimental costs [6]. Numerical models generally require high computation and storage and there is a direct relationship between the model complexity and computation resources. With the advent of ever faster and efficient computers, numerical models are more accurate and can simulate more detailed/complex models. For example, earlier crystal plasticity models could only model single crystal under basic loading conditions to save computational resources [7]. However, recent models are able to simulate complex loading conditions with a polycrystal model that accounts for the complete material through thickness [8].

Finite element phenomenological models are commonly used to simulate deformation problems. Phenomenological models simulate the material behavior by fitting the simulated material response to experimental results under different loading conditions. However, phenomenological models are unable to capture the microstructure evolution in the material. Therefore phenomenological models cannot capture texture effects such as earing [6]. In addition, it is well known that mechanical properties such as ductility, strength and surface finish are directly affected by the sheet microstructure [9] and cannot be captured using phenomenological models. Crystal plasticity models offer a viable solution as they capture the material physics on each crystal/grain and are able to predict the material stress-strain and texture evolution during deformation. Crystal plasticity theory is the study of plastic behavior in materials due to crystallographic slip that accounts for the anisotropic material behavior in the material [10].

Crystal plasticity models require the starting texture of the material and therefore it is important to use the correct starting textures in crystal plasticity models. Experimental methods used to capture the texture and grain size information often do not match the model size in the simulation. Therefore, it is necessary to have a tool that creates synthetic textures that statistically match the bulk experimental texture. In addition, it should be possible to tailor these synthetic textures to any model size [11]. These synthetic textures, also known as synthetic microstructures, can then be used as inputs to crystal plasticity models.

Typical material testing processes such as tensile, compressive, etc. involve small strains. These have been simulated and validated for various materials using conventional phenomenological [12, 13] and crystal plasticity models [14, 15]. However, sheet forming (usually performed by rolling) and extrusions involve huge strains in the material and fall in the category known as large strain problems. As rolling and extrusion are large strain problems, conventional finite element methods are unable to simulate them. This is due to the mesh distortion and local inaccuracies in finite element methods at high strains. In order for automotive designers to simulate large strain problems, it is important to have a framework that is able to simulate large strain problems. In addition, large strain problems also involve huge microstructural changes. Therefore it is important to simulate the texture evolution (crystal plasticity) during these processes.

Currently, literature presents several methods to simulate crystal plasticity based large strain problems such as rolling. Taylor type models are the most commonly used models in literature as they provide fast and efficient solutions to crystal plasticity problems [16, 17]. However, Taylor type models assume constant strain in each grain which can result in erroneous stress states in the material.

Taylor type and other crystal plasticity models have been used to simulate rolling by assuming a plane strain compression condition (e.g. [18, 19]). Yet, they are unable to capture the through thickness of the sheet. Experimental results show that it is important to capture the through thickness of the sheet as the material undergoes inhomogeneous deformation due to different strain paths experienced at different material thickness in the rolled sheet [20, 21]. For example, Figure 1 shows that the volume fraction of Rolling Texture and Shear Texture increases down the sheet thickness. In addition experimental results from literature also show a change in the grain size across the thickness of the sheet [21]. Therefore it is important to capture the through thickness of the sheet with the correct loading conditions when simulating cold rolling.

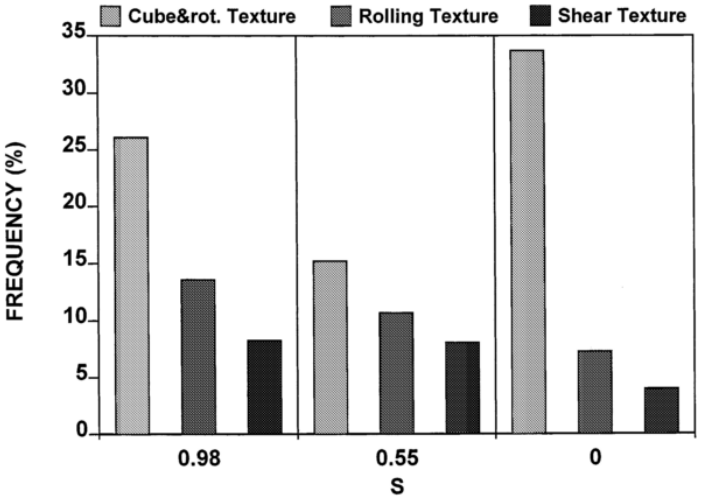

Figure 1: Volume fraction of different texture components at various sheet thickness depths [21]

It is important to consider the complete through thickness of the sheet with the correct loading conditions to capture the material stress-strain and texture evolution during cold rolling. FEM are the most common tool used to simulate large strain problems. However, as conventional FE cannot capture the texture evolution, crystal plasticity theory has been implemented to classical Finite Element Methods (CPFEM) to capture the texture evolution. In addition, literature presents various applications of CPFEM models (e.g. [10]). However, finite element formulations are prone to errors at higher strains due to high element distortion. Re-meshing is the most common technique used to overcome this problem. Re-meshing has been used successfully to model large strain problems such as extrusion. However, CPFEM models cannot work with re-meshing as each new element needs to be assigned a new orientation. Element Free Galerkin (EFG) methods provide a viable solution to this problem [22]. EFG problems have also been used to model crack and fracture problems [23]. EFG methods are meshless methods. They have also been shown to be more accurate than finite element methods as they do not accumulate numerical errors caused by distorted elements in FE models (Figure 2). Therefore an EFG based crystal plasticity framework needs to be developed to accurately model large strain problems such as rolling.

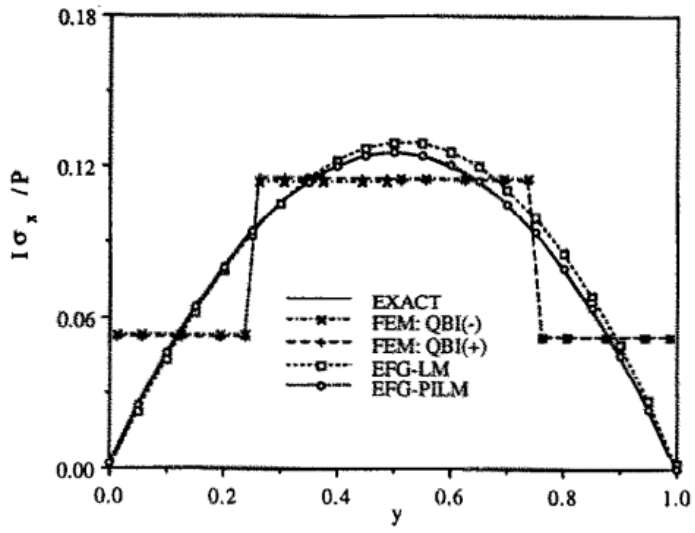

Figure 2: Experimental (Exact), simulated Finite Element Methods (FEM) and Element Free Galerkin (EFG) results for hole in an infinite plate [23]

Like rolling, hot compression is also a large strain problem and induces huge strains in the material. Hot compression is used as a stepping stone to understand the extrusion processes as they are both performed at high temperatures. In addition, like extrusion, hot compression can also be performed at different strain-rates. As hot extrusion can be carried out at various temperatures and strain-rates, it is important to include those effects in the crystal plasticity model. Currently, literature lacks modelling approaches to characterize and model the flow behavior and texture evolution of aluminum alloys (such as AA 6xxx) under different temperatures and strain-rates. Therefore there is a need to develop a strain-rate and temperature dependent crystal plasticity model to simulate large strain processes such as hot compression.

Experimental results show that aluminum alloys (e.g. AA 6xxx) undergo static recrystallization (Figure 3) at high temperatures [24, 25]. Static recrystallization involves identifying potential nuclei and their growth. Material that undergoes SRX results in a different material texture and grain size than the one without SRX. Therefore, material with and without SRX result in different mechanical properties. Therefore, it is very important to consider the effects of SRX after hot deformation to predict the correct texture and grain size. Hence, a through process model (crystal plasticity and SRX) is needed to model the material behavior, texture and grain size during hot compression.

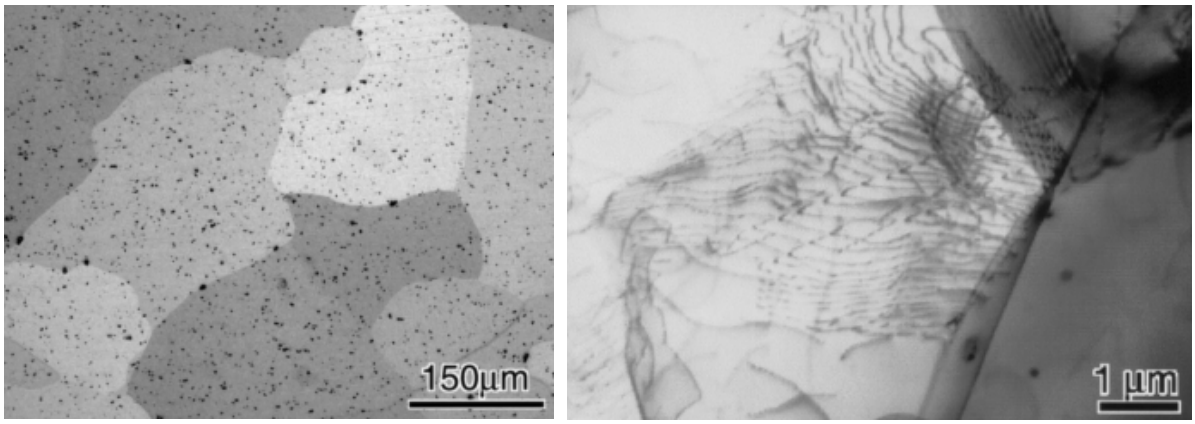

(a) (b)

Figure 3: (a) Optical micrograph and (b) TEM images for AA 6063 under high temperatures [25]

The main objective of this research is to model and analyze the stress-strain and microstructure changes during large strain problems namely; cold rolling and hot compression. A rate-dependent crystal plasticity based Element Free Galerkin (CPEFG) constitutive model was developed to model cold rolling in AA 5754. CP model was implemented in commercial software LS-DYNA as a user defined EFG material model (UMAT) to simulate the 3D microscopic response of AA 5754 under cold rolling. Simulated model captured the complete through thickness of the sheet. Results from CPEFG simulations were compared to experimental data and showed good agreement. A more detailed description of the CPEFG model, validation and implementation to cold rolling is given in Section 6.1.

Crystal plasticity simulations predict the overall texture and grain size in the material. However, this information can be used to calculate other grain metrics such as grain size, subgrain formation, texture preference, etc. Accurate grain size predictions during and after rolling are important as they relate to the material properties such as yield strength through the Hall-Petch effect [26]. It is well known that under certain deformations such as shear [27], FCC materials prefer certain texture components and predicting the development of these texture components is essential to any model. To study the evolution of texture components and other grain metrics, new tools need to be developed. Therefore, in this research, grain size and preferred textures for small and large grains near the top and center of the sheet were studied using an in-house grain analysis framework (gCode). In-house gCode is based on a neighbor misorientation path finding algorithm [28] to study the subgrain formation. More details about the gCode are discussed in Section 6.1.5.

In the second part of this work, hot compression was modelled using an in-house crystal plasticity Taylor model. A modified hardening CP model was used to model hot compression in AA 6063 under different temperatures and strain-rates. As hot compression involves SRX, a probabilistic integration point based SRX model was developed to model SRX at various temperatures and strain-rates. Simulated stress-strain, texture and grain size results were compared to experimental results. The Electron Back Scatter Diffraction (EBSD) on the initial AA 6063 was performed by Waqas Muhammad (a fellow student) while the hot compression Gleeble experiments were performed by Daniel Ohoh (PhD student with Prof. Marry Wells at University of Waterloo). More details about the modified hardening crystal plasticity model and SRX are discussed in Section 6.3.

In summary, the main objective of this work is to model and analyze the microstructure changes during large strain processes in FCC polycrystals. To accomplish this objective, this thesis is arranged as follows: Chapter 2 discusses the crystal plasticity theory, numerical models and microstructures used in numerical models. Chapter 3 discusses recrystallization and various approaches to simulate recrystallization. Chapter 4 discuss the overall scope and objectives of this work. Chapter 5 discusses the crystal plasticity and static recrystallization frameworks used in this work. Chapter 6 discusses the main results and presents the simulated cold rolling results from CPEFG simulations. Next, gCode is used to analyze various through thickness grain metrics under cold rolling. Chapter 6 also discusses the stress-strain, texture and grain size evolution during hot compression and validates the simulated results with experimental data. Lastly, Chapter 7 looks at limitations of current work and future work to improve the various modelling approaches presented in this work.

Chapter 2
Numerical Modelling

Computer simulations provide a huge advantage over conventional experimental approaches to model material behavior such as cost, time, etc. Therefore there is a huge push to accurately model the material behavior under different loading conditions using different types of numerical techniques. Conventional phenomenological models [29, 30, 12, 31–33] provide material stress-strain response and are adequate for most applications but do not account for material texture evolution. Crystal plasticity approaches solve this problem by accounting for material texture and are discussed below.

There are a number of ways to model large strain crystal plasticity problems. Taylor and Sachs approaches have been used with great success in literature [16, 17, 14] and can account for material texture evolution on an average sense. Other approaches such as Crystal Plasticity Finite Element Methods (CPFEM) are also used to model large strain problems. CPFEM methods can account for the complete material microstructure. In addition, CPFEM approaches provide full-field solutions and are discussed in more detail in Section 2.2. However, finite element methods do not allow for severe deformations due to mesh restrictions. In addition, high mesh distortion during deformation affects the final results in FEA simulations. FEA has been modified to Extended Finite Element Method (XFEM) which allows the study of failure and fracture in materials. New approaches such as meshless methods (EFG) provide the flexibility of severe deformations without mesh dependence. All the methods mentioned above solve a finite element ordinary differential equation with minor changes to its implementation in the final framework. These methods are briefly summarized below.

2.1 Crystal Plasticity Theory

2.1.1 Introduction

Metals are crystalline solids consisting of atoms arranged in different patterns. These patterns are repeated in all directions. This atomic arrangement can be described using unit cells as shown in Figure 4 [34]**.** Figure 4 shows the unit cells for typical metallic unit cells namely; face-centered cubic (FCC), body-centered cubic (BCC) and hexagonal close-packed (HCP). Some of the metals that have FCC crystal lattice structure are aluminum, γ-iron, copper, brass, nickel etc. β-iron, potassium and molybdenum belong to BCC while magnesium, titanium and zirconium belong to HCP lattice. In the present research proposal, focus is on FCC metals only.

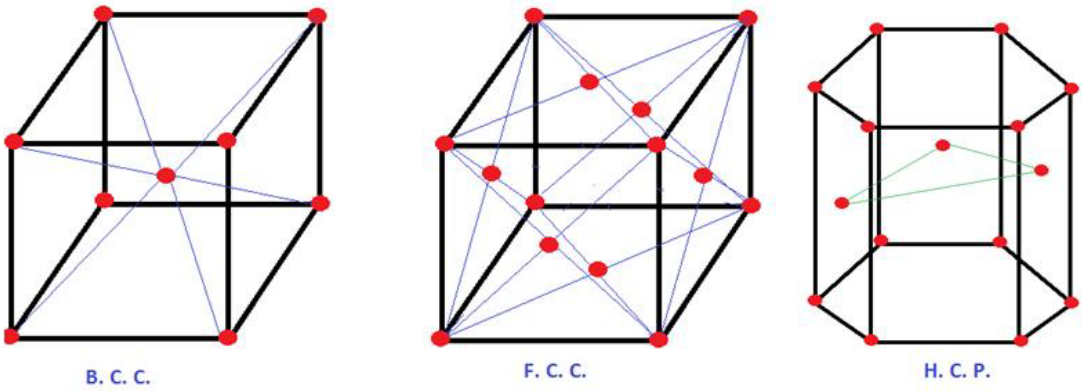

Figure 4: Unit cells of BCC (Body-centered cubic), FCC (Face-centered cubic) and HCP (Hexagonal closed packed) [34]

Real crystals contain imperfections in their lattice. These lattice imperfections could be as a point, line or interfacial defects. Point defects include interstitial atoms, vacancies and impurity atoms. Most important line imperfections are known as dislocations. Dislocations can be described as areas where atoms are out of place in the crystal lattice. This results in namely two type of dislocations; edge and screw. Edge dislocation centers on a line that is defined along an extra half-plane of atoms. Some atoms above this line are squeezed together and some are pulled apart. Screw dislocation is thought to be formed due to shear stress where one part of the crystal lattice moves relative to the other by one atomic distance. Interfacial defects include boundaries which separate crystallographic regions with different crystallographic orientations and include grain boundaries, twins, stacking faults and phase boundaries [35].

Plastic deformation occurs mostly due to movement of dislocations (line-defects). Concept of dislocations was proposed by Taylor [36] as the shearing of rows of atoms in a crystal propagating throughout the crystal with change in temperature and strain. Any applied stress can be transformed into shear stress on the glide plane of any dislocation. This is known as the resolved shear stress and is the cause of dislocation movement. FCC metals at room temperature have several plastic deformation mechanisms namely; slip, twinning and grain boundary sliding. However, slip is the principal mechanism of deformation. Therefore, only this mechanism is considered in this research proposal.

Dislocations have preferred planes and directions within those planes where motion occurs. The planes are called slip planes and directions are called slip directions. The combination of these is called a slip system. Slip systems depend on the crystallographic structure of the metal. Due to different slip systems, crystallographic slip is anisotropic. A FCC unit cell is shown in Figure 5a. A [1 1 1] type plane

is shown in the unit cell. Slip occurs along the <1 1 0> directions within the [1 1 1] slip plane. The number of independent slip systems represents the different combinations where slip can occur. For FCC, there are four unique [1 1 1] planes and three <1 1 0> directions per plane resulting in 12 unique slip systems.

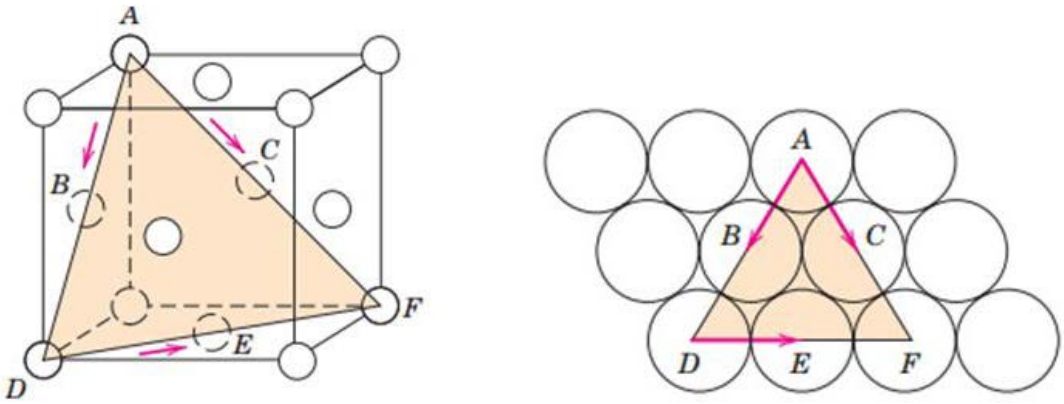

(a) (b)

Figure 5: (a) A [1 1 1] <1 1 0> Slip System in FCC unit cell (b) [1 1 1] Plane from (a) and three slip directions within the [1 1 1] plane (shown by arrows) [35]

Stress applied to a material can be resolved into shear stresses on slip planes and directions. On application of a stress, there is a most favorable slip system for a crystal. When the resolved shear stress reaches a critical value, this slip system undergoes slip. This shear stress is called the critical shear stress. This is known as the Schmid's Law [37]. Schmid Law is used to serve as a yield criterion for a single crystal. Schmid's Law states that extensive slip occurs when the resolved shear stress reaches a critical value. Therefore, a single crystal yields or deforms plastically, when the resolved shear stress reaches the critical resolved shear stress; i.e. when,

$$\tau_\alpha = m_{\alpha,ij}\sigma_{ij} = \tau_{y,\alpha}(i,j = 1,2,3) \quad \textbf{(1)}$$

where $\tau_\alpha$is the resolved shear stress for a slip system (α). σ_{ij} is the stress acting on the crystal, τ_y is the yield strength of α slip system and $m_{\alpha,ij}$ is defined as,

$$m_{\alpha,ij} = s_{\alpha,i}b_{\alpha,j} \quad \textbf{(2)}$$

where $s_{\alpha,i}$ and $b_{\alpha,j}$ are the components of the slip vectors $s_\alpha$and slip normal b_α for slip system α respectively. It should be noted that throughout this report, the usual convention of tensor summation is implied on i,j whereas α refers to the slip system.

2.1.2 Single Crystal Deformation Models

Properties of polycrystals can be derived from single crystal properties. This section discusses the rate-dependent and independent crystal plasticity formulations. Both formulations account for plastic deformation using crystallographic slip but have certain advantages.

2.1.2.1 Rate Independent Models

Schmidt law yields simple flow rules for shear rates ($\dot{\gamma}_\alpha$) for a slip system according to the rate independent crystal plasticity theory. Rules state that;

a. $\dot{\gamma}_\alpha = 0$ when current value of yield stress ($\tau_{y,\alpha}$) is greater than the resolved shear stress (τ_y).
b. $\dot{\gamma}_\alpha = 0$ when $\tau_{y,\alpha} = \tau_y$ and rate of resolved shear stress is less than slip system hardening matrix ($h_{\alpha\beta}$) times the increment of rate of shear ($\dot{\gamma}_\beta$) and
c. $\dot{\gamma}_\alpha = 0$ when $\tau_{y,\alpha} = \tau_y$ and rate of resolved shear stress is equal to the slip system hardening matrix ($h_{\alpha\beta}$) times the increment of rate of shear ($\dot{\gamma}_\beta$)

These rules characterize inactive, active and potentially active systems. Crystal plasticity theory by Taylor [38] states that only five independent slip systems out of 12 slip systems (for FCC) are required to completely prescribe any arbitrary strain. To select these active slip systems, it was suggested to use the combination of slip systems that yield the minimum shear rates. This was suggested based on single crystal experimental results [38]. This theory was also explained by the principle of maximum work [39]. It was shown by Chin and Mammel [40] that the theory of maximum work and minimum shear works out to be the same [41].

2.1.2.2 Rate Dependent Models

Yield surface of a rate-independent formulation is a polyhedron which has sharp corners. Sharp corners results in lack of uniqueness in the choice of actively yielding slip systems due to lack of uniqueness of the strain-rate vector perpendicular to the edges of the polyhedron. Another problem is that if the stress is on the corner of this yield surface, six or eight slip systems could be activated simultaneously corresponding to non-unique slips.

In order to resolve the ambiguities mentioned above, rate sensitivity was introduced into Taylor type models [42]. This method did not have explicit yielding of slip systems but assumed that all slip systems slip at a rate based on the current value of resolved shear stress. Due to the unique relation

between slip rates and stress states, the slip rate on each slip system could be determined uniquely. This solved the problem of non-uniqueness in stress states of rate independent solutions.

2.1.3 Polycrystal Models/Mean Field Homogenized Approach

In order for crystal plasticity models to predict real material response, they have to capture polycrystalline response. However, a polycrystal model must be able to offer more than a phenomenological model. It should be able to capture and explain phenomenon that phenomenological models are unable to e.g. texture, microstructure evolution, grain morphology. Accurate prediction of texture evolution is very important as many forming operations (e.g. stamping) are texture dependent. In general single crystal models which already have the required parameters such as slip, twinning, etc. included in them can be adapted to polycrystal models. Polycrystal models discussed below are mean field models and provide average response of the crystal. They are known as mean field or homogenized models as they capture the polycrystalline response in the average sense.

2.1.3.1 Sachs Model

Early polycrystalline models made some continuity assumptions across grains. Sach's model [43] assumes that all grains in a model are subjected to the same stress state. Sach's model also assumes that only one slip system is active at any moment in time in each grain. This model was later modified so that each grain was assumed to be subjected to the same strain [44]. The assumption that each grain experiences the same stress ignores the strain continuity across grain boundaries [39]. In addition, some numerical inconsistencies were also observed by Asaro and Needleman [42].

2.1.3.2 Taylor Model

Taylor's model assumes the same strain per grain but requires 5 slips systems to be active at once (for FCC). Selection of five slip systems to minimize slip results in checking all possible combinations (384 for FCC structure). Strain is found by applying a volume average across all grains and hence is known as a full constraint model. The Taylor model also accommodates for the strain continuity across grain boundaries.

Taylor model was based on experimental observations of a cross-section of a drawn wire. Taylor observed that all grains were elongated in the direction of extension. This lead to the conclusion that each grain experienced the same strain. In addition, each grain deforms in exactly the same way inside a polycrystal and satisfies:

$$\frac{\sigma_g}{\tau} = \frac{d\gamma}{d\varepsilon} = M \quad \textbf{(3)}$$

where σ_g is the axial stress in a grain, τ is the shear strength, $d\gamma$ and $d\varepsilon$ are the increments in shear-strain and aggregate strain and M is the orientation factor that depends on the lattice orientation. However this implies abrupt changes in stress between neighboring grains based on their orientations. This can cause numerical instabilities as reported by Bishop and Hill [45, 46].

The simplicity of the Taylor approach has been applied in combination with other numerical methods such as Finite Element Methods. Experimental works have proven that the equal strain assumption used in the Taylor model is not true. However, the Taylor model has been used in simulating various problems with accurate results particularly in the prediction of forming limit diagrams [16, 17, 14].

A modification of the Taylor model, known as the relaxed constraints model has also been implemented [47]. By relaxing the compatibility constraints, this type of model has been used to predict texture evolution in FCC metals. Relaxed constrains model has also shown improvements over the Taylor model under simple shear [48].

2.1.3.3 Viscoplastic Self Consistent Model (VPSC)

A self-consistent polycrystal model was proposed by Kroner [49] and Hill [50]. This was a self-consistent model, based on Eshelby's formulation [51], that treated the deformation of each grain as the solution for an elastic elliptical inclusion within a homogenous matrix average across all the grains.

Lebensohn et al. [52] extended this model to predict the stress-strain as well as texture evolution. This model was later revised to include plasticity by introducing the viscoplastic self-consistent (VPSC) scheme[53]. Self-consistent models find the local strains by averaging the response between different grains. VPSC model uses the Eshelby's inclusion model [51] and links the average strain-rate ($\bar{\varepsilon}^{(r)}$) to the average eigen strain-rate ($\bar{\varepsilon}^{*(r)}$) using the Eshelby tensor (S). The model assumes each grain as an elliptical inclusion in a viscoplastic medium where the material response for the grain and medium is given by:

$$\varepsilon^{(r)} = \gamma_0 \sum_k m^{k(r)} \left[\frac{m^{k(r)} : \sigma^{(r)}}{\tau_0^{k(r)}} \right]^n \quad \textbf{(4)}$$

where $\varepsilon^{(r)}$ is the strain on each grain (r), $\tau_0^{k(r)}$ is the resolved shear stress on each slip system (k), γ_0 is the normalization factor and n is the rate-sensitivity exponent.

The VPSC model has been used extensively for FCC, BCC and HCP materials (such as [54, 55]). VPSC model has been shown to accurately predict the stress-strain response and texture evolution under complex strain paths, such as rolling [56].

2.2 Full-Field Models

Mean field models mentioned in the previous section provide the average behavior of the material but are unable to capture important material phenomenon such as intra-granular stresses, grain breakage, grain-to-grain interaction, etc. Full field models provide the ability to study these phenomenon in detail as they do not use any averaging scheme to find local strains and are discussed below.

2.2.1 Finite Element Analysis (FEA)

Finite Element Analysis has been used extensively to model deformation problems. Phenomenological models try to model the physics of deformation by incorporating various mathematical expressions to experimental results. Phenomenological models have been shown to predict material response under all types of loading conditions, strain-rates and temperatures (such as [12, 31, 57–59]). Unlike earlier models [60], recent phenomenological models can account for the material asymmetry and anisotropy [12, 31]. However, FE based models can also be implemented with crystal plasticity framework to account for the texture evolution. FE models provide the advantage of full-field approach which can accurately account for the texture evolution and intra-granular material behavior [8, 61–64]. As mentioned earlier, FE models can also be combined with other models e.g. Taylor model to provide full and relaxed constraints model. Basic FE models try to find the solution to the momentum equation

$$\sigma_{ij} + \rho f_i = \rho \ddot{x}_i \tag{5}$$

Satisfying the traction and displacement boundary conditions

$$\sigma_{ij} n_i = t_i(t) \tag{6}$$

$$x_i(X_a, t) = D_i(t)$$

$$\left(\sigma_{ij}{}^{+} - \sigma_{ij}{}^{-}\right) n_i = 0$$

where σ is the Cauchy stress, ρ is the density of the material, f is the body force, t is the traction, $\ddot{x}$ is the acceleration of the body and ${\sigma_{ij}}^{+}$ and ${\sigma_{ij}}^{-}$are the stresses on boundary. This leads to the weak form of the equilibrium equation:

$$\delta\pi = \int_v \rho\ddot{x}_i\delta x_i dv + \int_v \sigma_{ij}\delta\varepsilon_i dv - \int_v f_i\delta x_i dv - \int_b t_i\delta x_i ds = 0 \quad \textbf{(7)}$$

This equation complies with the principle of virtual work that states that a body in equilibrium and subjected to displacements will have the virtual work of external forces on the body equal to the virtual strain energy of the internal stresses [65].

Next, introduce the mesh in finite elements and re-write Equation 7 in terms of shape functions (N_i)

$$\sum_{m=1}^{n}\left[\int_{v_m}\rho\ddot{u}_i N_i^m dv + \int_{v_m} {B_{ij}^m}^t D_{ij}^m B_{ij}^m N_i^m u_i^m dv - \int_{v_m} f_i^m N_i^m dv - \int_b t_i^m N_i^m ds\right] = 0 \quad \textbf{(8)}$$

where strain (ε) and stress (σ) is written in terms of nodal displacements and displacements are approximated by nodal displacements (u) using:

$$\varepsilon = Bx, x = Nu, \sigma = D\varepsilon \quad \textbf{(9)}$$

We can re-write this equation in matrix form,

$$\sum_{m=1}^{n}\left[\int_{v_m}\rho N^t N\ddot{u}dv + \int_{v_m} B^t DBdvu - \int_{v_m} N^t f dv - \int_b N^t t ds\right] = 0 \quad \textbf{(10)}$$

These expressions can be expressed as

$$[M][\ddot{u}] + [K][u] = [F] \quad \textbf{(11)}$$

and integrated to find the nodal displacements (u).

2.2.2 Extended Finite Element Method (XFEM)

Extended Finite Element Method (XFEM) was developed to predict crack initiation and propagation [66, 67]. The key idea is that the displacement equation incorporates the crack discontinuity as an additional term in the finite element formulation [68]. Displacement is given as [69]:

$$u^h(X,t) = \sum N_I(X)\{u_I(t) + H\big(f(X)\big)H\big(g(X,t)\big)q_I\} \quad \textbf{(12)}$$

where $N_I(x)$ is a shape function, and u_I and q_I are the regular and enriched nodal values respectively. $H\big(f(X)\big)$ is the Heaviside function which is active only when $f(X)$ is greater than zero. Functions f(x) and g(x) define the continuous crack geometry in the material shown in Figure 6.

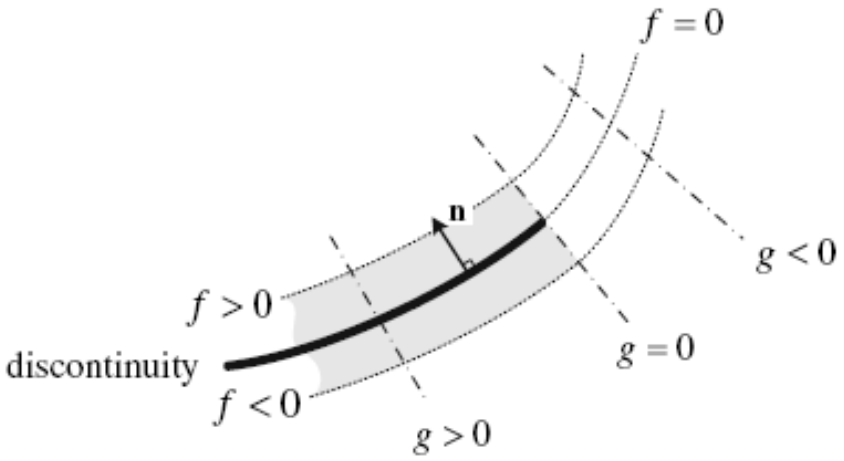

Figure 6: Discontinuity representation in XFEM [69]

The main disadvantage of XFEM is the additional CPU time. In addition, XFEM simulations cannot predict crack speeds and multiple cracks unless the model is tuned with the experimental results [69]. XFEM simulations also require the user to input the discontinuity on the basis of some failure criterion to predict cracks.

As discussed, XFEM was developed for crack problems and does not provide the flexibility of incorporating severe deformations in its formulation. Severe deformation can be incorporated with XFEM by using adaptive meshing techniques. However, these techniques require huge computational times.

2.2.3 Element Free Galerkin (EFG)

EFG is a relatively new mesh-less numerical method [70]. Unlike classical FE simulations, EFG methods use only nodes and do not require elements. This makes it easier to mesh complex parts and geometries. Even though re-meshing allows FE models to simulate complex strain paths [71], nodal mesh in EFG simulation allows for simulating high deformation problems without re-meshing.

EFG is based on the partition of unity method [72] and elements in EFG are called cells. In FE methods, cells are known as elements and are predefined by the user. However, in EFG, cells are calculated based on the problem definition and can be calculated based on a fixed or variable radius from the current point. This could result in different cells with different number of points. In addition, cells in EFG could also be squares, circles (2D) or cubes, spheres (3D). These cells can be static or evolve during simulations. A sample of circular cells in a given domain is shown in Figure 7.

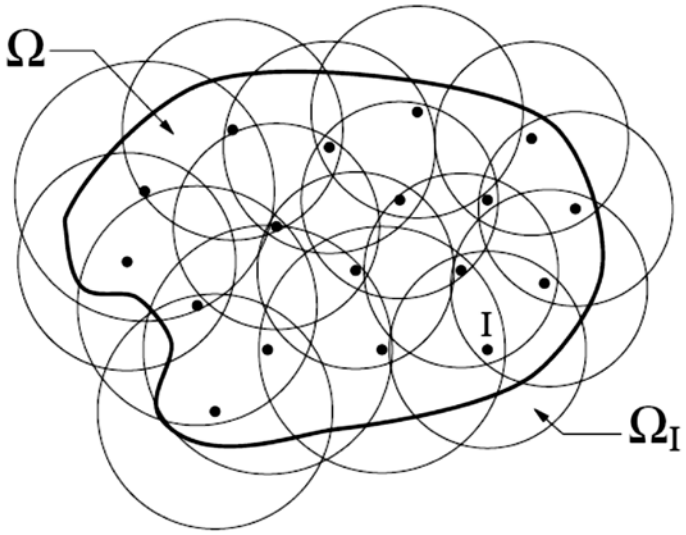

Figure 7: EFG cells in a sample [73]

EFG employs moving least square (MLS) approximants to approximate the displacement functions. These approximations consist of a weight function, a polynomial basis and position based coefficients. A linear approximation of displacement (u) can be written as:

$$u^h(x) = a_0(x) + a_1(x)x \quad \textbf{(13)}$$

where the unknown parameters (a_i) change with x.

The MLS approximation in the whole domain is given by [23]:

$$u^h(x) = \sum_{i=1}^{m} p_i\,(x) a_i(x) = p^T(x) a(x) \tag{14}$$

where p_i are the components of the monomial basis function and a_i are their coefficients. The coefficients are found by minimizing a weighted discrete L_2 norm and depends on the weight function and the neighborhood of x. A linear basis in 3D is given as:

$$p^T(x) = [1, x, y, z] \tag{15}$$

This stationarity of the L_2 norm with respect to $a(x)$ to the following linear relation:

$$A(x)a(x) = B(x)u \tag{16}$$

where $A(x)$ and $B(x)$ are defined in terms of the weight functions (w) and monomial basis (p). Weight function (w) should be constructed to be positive and guarantee a unique solution to $a(x)$. Generally EFG weight functions are more complicated than finite element weight functions and are available as exponential, cubic and quartic-spline functions. A simple weight function (based on distance) can be written as:

$$w(x - x_i) = ||x - x_i|| \tag{17}$$

Substituting 14 into 16 results in

$$u^h{}_i(x) = \sum_{i=1}^{m} N_i(x)\, u_i \tag{18}$$

where $N_i(x) = p^T A^{-1} B_i$ is the shape function to approximate the nodal displacement (u_i).

The rest of the EFG problem simplifies to a set of integrals, similar to any other finite element problem. Unlike finite element problems, that loop on each element, EFG problems loop on each quadrature point (m). The main disadvantage of the EFG method is that they require very large CPU time and EFG simulations can take 2-3 times longer than “classical” FE models for the same problem. This is due to the relatively complicated weight functions and shape function approximations used in EFG.

2.2.4 Fast Fourier Transform Method (FFT)

As discussed above, Finite Element Methods have been used extensively to account for different types of material problems. However, due to the large number of degrees of freedom required by FE methods, there is an inherent size limitation based on the computational resources. FFT methods provide an effective alternate solution as they can account for fine-scale microstructural information that is hard to achieve with FE methods. However, FFT methods assume periodicity and require periodic conditions across the length of the sample. Hence FFT methods are not as versatile as FE methods.

Moulinec and Suquet [74] initially proposed a FFT based method for composites which was later used by Lebensohn [75] to model viscoplastic polycrystals and then elasto-viscoplastic polycrystals [76]. The basic FFT framework works on a 3D point grid with a fixed amount of Fourier points in each direction and a periodic boundary across the RVE where the total strain and stress are given by:

$$\epsilon(x) = \tilde{e}(x) + E \qquad \sigma(x) = C_0 : \epsilon(x) \tag{19}$$

where $\tilde{e}(x)$ is the strain fluctuation in the crystal, $\epsilon(x)$ is the local strain field, E is the average strain in the material, $\sigma(x)$ is the stress field and C_0 is the initial local elastic stiffness matrix.

The local fluctuation of the displacement field is calculated using the Green function as:

$$\tilde{e}_k(x) = \int_{R^3} G_{ki}(x - x')\tau_{ij,j}(x')dx' \tag{20}$$

where $G(x - x')$ is the Green function and τ is the shear stress. Using Equation 19 and converting this expression into Fourier space results in:

$$\tilde{e}_{ij}(x) = \hat{\Gamma}_{ijkl} * \hat{\tau}_{kl} \tag{21}$$

where $\hat{\Gamma}$ can be calculated as:

$$\hat{\Gamma}_{ijkl} = -\frac{1}{2}(\xi_i \xi_j A'^{-1}_{ik} + \xi_i \xi_j A'^{-1}_{ik}) \tag{22}$$

where ξ is a Fourier point and A is the product of initial local elastic stiffness matrix (C_0) for each ξ.

2.3 Orientation Space

Orientations are used to completely describe a relation between two coordinate frames. Similarly, material texture is defined as a set of orientations corresponding to all the crystals in the material. Orientations are represented usually in Euler space as Bunge angles $(\varphi_1, \emptyset, \varphi_2)$ to describe the crystal orientation with respect to the global space [77]. This space is finite and is used to describe any texture component by a single point where texture is defined as a non-uniform distribution of crystallographic orientations in a polycrystalline aggregate [78]. Bunge angles describe this point as an anticlockwise rotation about z-x-z axis. As shown in Figure 8, this can be described as a rotation about [0 0 1] (ND - Red), [1 0 0] (Green) and [0 0 1] (Blue) crystal direction.

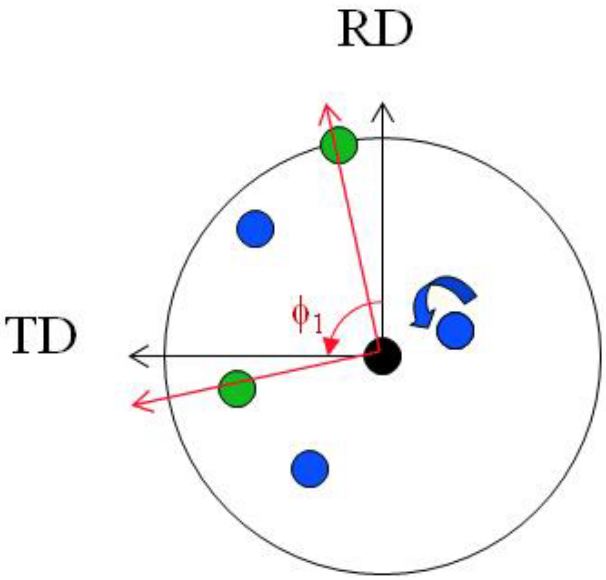

Figure 8: Rotation in Euler space on crystal axis [79]

Orientations in 3D space can also be represented using quaternion's (q_0, q_1, q_2, q_3) such that $\sum q_i = 1$. Quaternion space is defined by a scalar (q_0) and a vector. Quaternions are used due to the ease of normal mathematical operations when using multiple quaternion's [80]. For example, addition of two quaternions (a, b) is given as:

$$a + b = (a_0 + b_0), (a_1 + b_1), (a_2 + b_2), (a_3 + b_3) \quad \textbf{(23)}$$

Crystal plasticity framework implemented in this work use Euler space while all the calculations to calculate misorientation are performed in quaternion space. Therefore it was necessary to define functions that could be used to switch between these spaces while maintaining the FCC symmetry conditions.

A rotation angle/axis pair (w, n) can also be used to describe a quaternion [81] and the relationship between a quaternion and Euler angles can be written as:

$$\pm q = \pm\left[cos\left(\frac{w}{2}\right), sin\left(\frac{w}{2}\right)n_1, sin\left(\frac{w}{2}\right)n_2, sin\left(\frac{w}{2}\right)n_3\right] \quad (24)$$
$$= \pm\left[cos\left(\frac{\beta}{2}\right)cos\left(\frac{\alpha+\gamma}{2}\right), -sin\left(\frac{\beta}{2}\right)sin\left(\frac{\alpha-\gamma}{2}\right),\right.$$
$$\left. sin\left(\frac{\beta}{2}\right)cos\left(\frac{\alpha-\gamma}{2}\right), cos\left(\frac{\beta}{2}\right)sin\left(\frac{\alpha+\gamma}{2}\right)\right]$$

where (α, β, γ) are the Roe/Matthies angles and are related to the Euler angles by:

$$\alpha = \varphi_1 - {}^{\pi}/_{2} \quad (25)$$
$$\beta = \emptyset$$
$$\gamma = \varphi_2 - {}^{3\pi}/_{2}$$

Conversion from Euler to quaternion (q) or vice-versa requires the selection of the quaternion that results in the minimum misorientation angle out of the 24 possibilities. Possible symmetry operations (S_i) that can be performed on a quaternion for an FCC crystal are given as:

q(1; 0,0,0)	q(0.5; 0.5,-0.5,0.5)	q(1/√2; 1/ √2 ,0,0)	q(0; 1/√2, 1/√2,0)
q(0; 1,0,0)	q(0.5; -0.5,0.5,-0.5)	q(1/√2; 0, 1/√2,0)	q(0; -1/√2, 1/√2,0)
q(0; 0,0,0)	q(0.5; -0.5,0.5,0.5)	q(1/√2; 0,0, 1/√2)	q(0; 0, 1/√2, 1/√2)
q(0; 0,0,1)	q(0.5; 0.5,-0.5,-0.5)	q(1/√2; - 1/√2,0,0)	q(0; 0,- 1/√2, 1/√2)
q(0.5; 0.5,0.5,0.5)	q(0.5; -0.5,-0.5,0.5)	q(1/√2; 0,- 1/ √2,0)	q(0; 1/√2,0, 1/√2)
q(0.5; -0.5,-0.5,-0.5)	q(0.5; 0.5,0.5,-0.5)	q(1/√2; 0,0,- 1/ √2)	q(0; -1/√2,0,1/ √2)

The 24 possible quaternions (Q) are found using:

$$Q = qS_i \quad (26)$$

Final quaternion is the one with the minimum misorientation angle chosen from the results obtained using Equation 26. The procedure for finding misorientation between two quaternions is presented in the next section.

2.3.1 Misorientation

Misorientation provides an insight into the difference between the orientations of two neighboring grains. Misorientation angles are used in recrystallization models to calculate potential nuclei. Misorientation angles are also used to find the volume fraction of different texture components in a sample. Given two grains (A and B), misorientation between these grains is the crystal rotation required to bring the crystal lattice of grain A in coincidence with the crystal lattice of grain B [78]. There are multiple ways to represent the misorientation between grains. In this work, we use the angle/axis method where the misorientation is described by an angle and a rotation axis. This method results an angle of rotation between two grains which makes it easy to compare misorientation between multiple grains in the sample.

Misorientation (M) is found between two elements or two grains with orientations q^1 and q^2(Equation 27). Crystal symmetry solutions are important here as discussed in the previous section and are found using Equation 28.

$$\Delta q = \Delta q(q^1, q^2) = (q^1)^{-1} q^2 \tag{27}$$

$$M = \Delta q S_i \tag{28}$$

2.3.2 Metrics for Texture Evolution

A grain is made up of a cluster of elements that share the same orientation in the initial texture. Difference between two grains is based on the misorientation between element neighbors. Results presented in this thesis also look into volume fractions of different texture components during the deformation process. Volume fraction for a texture component was found by comparing the orientation of each element to the component orientation within a 10 deg minimum Gaussian misorientation spread. The process of finding volume fractions of texture components comes from the orientation distribution function (ODF). The basic expressions used to calculate volume fraction are:

$$V_f = \int f(g)\, dg \tag{29}$$

$$f(g) = \frac{\Delta V_f}{\Delta \Omega} \tag{30}$$

where V_f stands for physical volume fraction of grain, $f(g)$ is the orientation distribution function and $\Delta\Omega$ is the increment in volume [82].

Misorientation distribution function (MDF) is also a continuous function like the ODF and looks at the grain boundary misorientation. However, MDF is based on the area fraction instead of volume fraction as grain boundaries represent 2D areas and is defined as:

$$\frac{\Delta A}{A} = \frac{\int_{\Delta\Omega} \int f(\Delta g)\, d\Delta g}{\int_{\Delta\Omega_0} \int f(\Delta g)\, d\Delta g} \quad (31)$$

where V_f stands for physical volume fraction of grain, $f(\Delta g)$ is the misorientation distribution function and $\Delta\Omega_o$ is the total volume of misorientation space considered [78].

2.4 Microstructures in Numerical Modeling

Metals used in industry are polycrystalline with different orientations. Metals do not have random orientations; instead they have preferred orientations or textures. Textures are developed at all stages of any forming process and affect the mechanical, thermal and electrical properties of a material. For example rolling of aluminum results in γ-fiber which is a combination of Cube, Copper, Brass and S components. Formation of γ-fiber is very important in enhancing the formability of aluminum [83]. Some common texture components and their corresponding Euler angles $(\varphi_1, \emptyset, \varphi_2)$ and Miller indices are given in Table 1. Miller indices represent the crystal direction parallel to the sample Z-axis as {h k l} and the corresponding crystal direction as <u v w>. The corresponding pole figures are shown in Figure 9.

Table 1: Typical texture components in FCC metals [84]

Component	Bunge Euler Angles (deg)	{h k l} <u v w>
Cube	(0, 0, 0)	{0 0 1}<1 1 0>
Copper	(0, 35, 45)	{1 1 2}<1 1 1>
S	(64.93, 74.5, 33.69)	{2 3 1}<1 2 4>
Goss	(0, 45, 0)	{0 1 1}<1 0 0>
Brass	(35, 45, 0)	{0 1 1}<2 1 1>

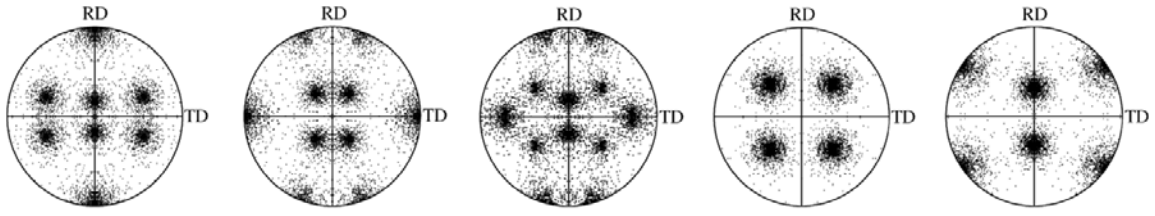

(a) (b) (c) (d) (e)

Figure 9: 15^0 Gaussian spread <1 1 1> pole figures for (a) Copper (b) Brass (c) S (d) Cube (e) Goss [85]

Prediction of these texture evolutions is important as many forming operations are carried out on rolled sheets. Hence, formability of metals depends highly on their textures. In addition, undesirable forming effects such as earing [6], Lüders bands [86], roping [87], etc., are easily solved by understanding the microstructure changes during forming.

Material crystal plasticity simulations is simulated as a representative volume element (RVE). RVE's assume a repetitive symmetry in the actual material texture [88]. Some examples of simulations involving RVE's include phase changes [89] and multi-scale analysis [90]. RVE's can also predict forming effects such as, earing during stamping and through thickness texture differences during rolling [64].

Accuracy of crystal plasticity simulations depends on the quality of microstructural information (RVE) used in the model. Microstructural information includes the orientation for each element, grain morphology, etc. Grains are formed by elements with the same orientation. 2D RVE's have been used extensively to simulate many problems in literature (e.g. [91]). However, due to the availability of faster computers, numerical models use 3D microstructures as they carry more microstructural information and accuracy. This entails developing techniques to develop 3D microstructures and meshes for finite element simulations. A few approaches are discussed in the following sections.

2.4.1 Material Data

Microstructure data characterization for materials in either 2D or 3D is a difficult task. It becomes even more difficult for generation of 3D microstructures as the standard grain orientation technique, EBSD (Electron Backscatter Diffraction), produces 2D data [92]. A 2D scan done by an EBSD is for a single plane of a material. Material is serially sectioned and polished and scanned again and again to get multiple 2D surfaces to create a reasonable estimate of the real microstructure. Several numerical techniques are also used to develop 3D microstructures without the use of serial sectioning to avoid high equipment costs, alignment of scans and time consuming material removal. A number of methods currently exist to produce 3D microstructures by using 2D EBSD data without doing serial sectioning and will be discussed in the following sections.

2.4.1.1 Structured Microstructures

Series of uniform volume filling shapes (bricks, octahedrons, pyramids, etc.) are considered as grains and are used to create 3D microstructures (Figure 10). Each shape/grain is assigned an orientation based on the measurements from the 2D EBSD scans. The downside of this approach is that each grain is based on the same shape and size which is not in-lieu with experimental results. Another downside of this method is that all inter-grain boundary angles are exactly the same throughout the material.

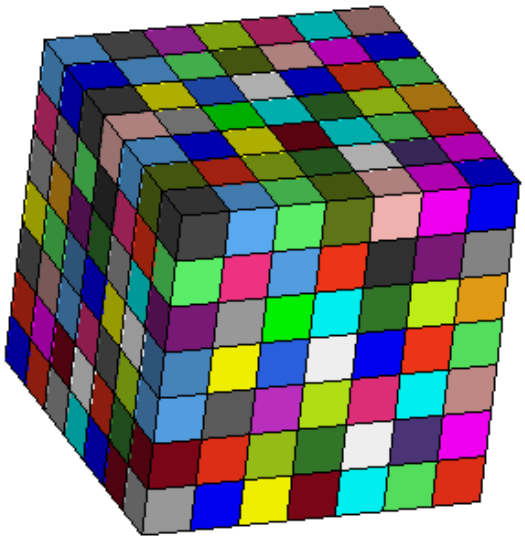

Figure 10: Random microstructure example [93]

2.4.1.2 Columnar Microstructures

The simplest method of creating 3D microstructures is to extrude the 2D grain structure from an EBSD scan to form columnar microstructures [94]. This creates 3D columnar grains as shown in Figure 11. One of the problems with producing columnar grains is that grains in most real materials do not resemble this format. The problem is that all scans perpendicular to the extrusion produce the same 2D picture. This means that a single 2D cross-section of the material is not sufficient to represent the grain morphology inside the material. Another problem is that all grain boundaries are exactly aligned with the extrusion direction.

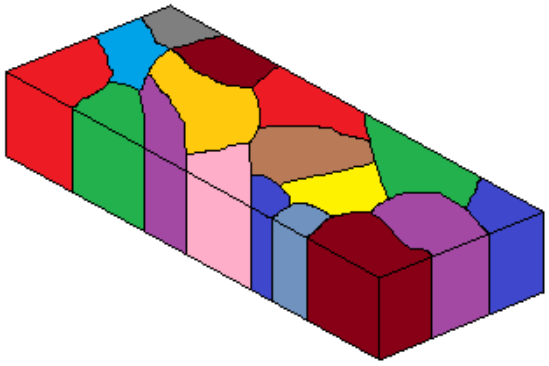

Figure 11: Columnar microstructure example [93]

2.4.1.3 Statistically Equivalent Microstructures

Microstructure generators, such as M-Builder, create statistically equivalent microstructures [11, 95]. M-Builder takes in two orthogonal 2D scans of the material and analyses them to identify grain size, aspect ratio, orientation distribution, misorientation distribution and grain size. A volume of space in the material is filled with ellipsoids of different sizes (around the average grain size) with measured material aspect ratios (Figure 12). Points are then randomly introduced and Voronoi tessellation is performed to make non-interference, volume-filled structure. All the created Voronoi cells that reside within the same ellipsoid are merged to make a single grain. Grain orientations are assigned next based on the orientation and misorientation distribution in the real material. An iterative approach is used to compare and reduce the discrepancies between the experimental and calculated orientation space, misorientation distribution and average grain size.

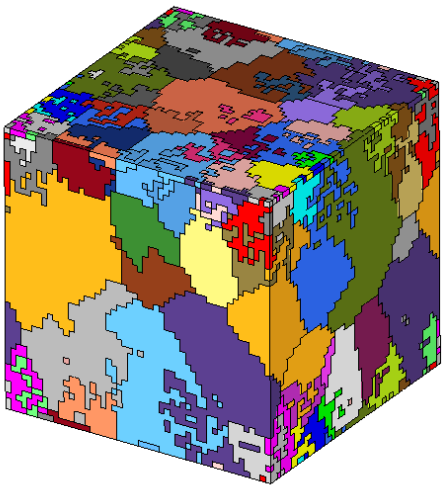

Figure 12: Statistically equivalent microstructure (M-Builder) example [93]

2.4.1.4 Point Data

Point data technique uses a set of points with Euler angles that represent the overall texture of the material [17]. The overall texture of the material matches the ODF and pole figure data of the bulk material. This technique is used in Taylor type homogenized full constraint models and has been used to predict material stress-strain response and texture evolution [16] as well as Forming Limit Diagrams (FLD) [17] for FCC and BCC materials. The main disadvantage of this technique is that it does not account for grain size and morphology.

2.4.2 Mesh from Microstructure for Finite Element Analysis (FEA)

Accuracy of FEA results depends heavily on the generated mesh. There are multiple ways of building/generating a mesh to represent the grain morphology of the material [93]. One of the ways is to represent multiple grains by a single element and a polycrystal model can be used to approximate the behavior of the material. Similarly, every grain can be represented by an element that behaves like a single crystal [96]. Lastly, every grain could be represented by multiple elements such as each element in the grain is assigned the same orientation and acts as part of the grain [15]. The final methodology is used in this work due to its ability to model complete grains. This also allows the study of sub-grain formation, inter and intra-granular parameters.

CPEFG model is created from 3D grain data obtained from statistically equivalent microstructures as discussed in Section 2.4.1. This 3D microstructure data is typically in voxelized (3D pixels) form. In this research, brick elements are created around the voxelized data. Next, each element is assigned the orientation of the voxel it represents. This method is relatively fast and efficient and gives complete control over element size. The elements produced by this method are perfect cube elements with no distortion in element shapes [88].

2.5 Summary

In this Chapter, various single crystal plasticity approaches namely; rate-dependent and rate-independent formulations have been presented. Rate independent models derive from the Schmidt law which is based on inactive, active and potentially active slip systems. In addition, yield surface from a rate-independent formulation results in sharp corners which results in uneven stress states. To solve these inherent problems with rate-independent models, Taylor type rate –dependent models were introduced [42]. Rate-dependent models assume slip on all slip systems. Thus Taylor type models do not result in uneven stress states.

As crystal plasticity models have to capture polycrystalline response, crystal plasticity models use polycrystal models to simulate material behavior. Sach [43] and Taylors [42] crystal plasticity models have been used extensively in literature to predict material response and texture evolution on various materials due to the ease of implementation. However, both Sach and Taylor models make unrealistic assumptions to simulate material behavior. In comparison, VPSC models provide a more flexible solution where each grain is assumed as an elliptical inclusion in a viscoplastic medium. However, VPSC models find the local strains by averaging the response between two grains. Hence VPSC models are unable to capture full-field response.

Full-field models are able to overcome all the limitations over other models. Full-field models capture the local strains at each point. However, there are various approaches to model full-field crystal plasticity simulations. Finite element models have been used extensively to model all kinds of material response under all types of loading conditions with crystal plasticity models. In addition, XFEM models provide enrichment to CPFEM models to capture the material behavior under fracture. However, both these techniques are mesh dependent. Therefore both these techniques cause numerical instabilities under large strains. Therefore meshless methods like EFG methods were introduced but have not been used with crystal plasticity formulation. EFG methods are independent of mesh and do not cause numerical instabilities at large strains. Recently, FFT methods have also been introduced to model crystal plasticity problems. However, FFT methods assume periodicity and cannot model complex deformation paths.

Unlike phenomenological models, crystal plasticity models require material texture data as inputs and provide the deformed material texture as one of the outputs. In this research, Bunge Euler angles are used to define texture at each material point and are converted to quaternions before calculating the volume fractions and misorientation for each element.

There are several ways to incorporate texture data into crystal plasticity simulations. Experimental EBSD data can be used directly as inputs to crystal plasticity simulation. However, as EBSD provides data in 2D, 3D crystal plasticity models require the need for synthetic microstructures [88]. In this research, 3D model is created from grain data obtained from synthetic microstructures where each grain is represented by multiple elements. More details about the crystal plasticity framework and CPEFG are provided in Sections 5.1 and 6.1 respectively.

Chapter 3
Recrystallization

Reconstruction of grain structure at higher temperatures is known as recrystallization [97]. This change in grain structure is caused by high-angle grain boundary motion which results in orientation change in the grains [98]. This results in a decrease of the free energy in the polycrystalline material as more grains are recrystallized during or after deformation. Recrystallization during deformation is known as dynamic recrystallization (DRX) and after deformation is known as static recrystallization (SRX) [99, 100]. Recrystallization is a very important phenomena as it effects the final texture and grain size of the material which subsequently effect the material properties. A sample of Al-0.1% Mn during annealing process (SRX) is shown in Figure 13. Figure 13 shows that as time progresses, grain size increases (from left to right).

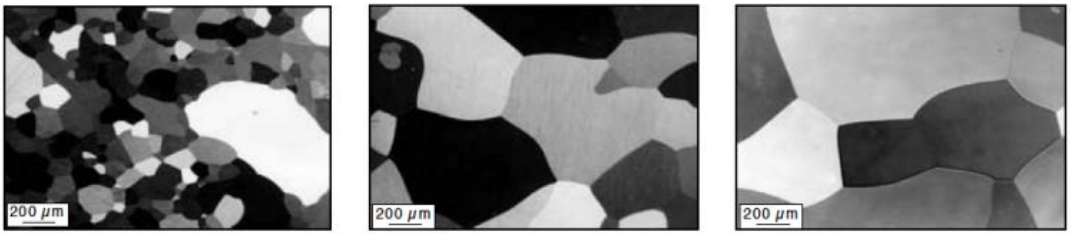

Figure 13: Microstructure change during annealing (Al-0.1% Mn) after 95% cold rolling [97]

Experimental results from literature break down DRX and SRX into continuous and discontinuous recrystallization. Continuous recrystallization happens evenly across the material while discontinuous recrystallization (abnormal grain growth) happens in only a few orientations at the expense of other nuclei [98].

Recrystallization during heat treatment of a deformed material starts with generation of small grains that grow at the expense of the deformed microstructure until the matrix is entirely consumed. At this point, the old microstructure has been completely replaced by a new microstructure [97]. This process is characterized by nucleation and grain growth. The work presented in this thesis focuses on SRX and will be discussed in more detail.

3.1 Static Recrystallization (SRX)

Static recrystallization deals mostly with the change in microstructure after deformation and is found to occur in FCC [101], BCC [102] and HCP [103] metals. As deformation proceeds, the free energy in a polycrystalline material increases due to the presence of dislocations and remains in the material even after deformation. These material defects (dislocations, etc.) can change material properties due to their effect on grain morphology, texture, stress-strain behavior, etc. and may be removed by thermomechanical processing of the material at high temperatures (SRX, annealing).

The response of polycrystalline metallic structures to external loading/forming is mainly controlled by the dislocation content and the microstructure. As dislocation density increases, the strength increases and ductility decreases in the material [104]. Furthermore, annealing of the deformed microstructure causes annihilation of these dislocations by SRX, which involves formation of new grains and hence controls the grain size and texture of the resulting material. Thus the material microstructure is linked with the dislocation substructure (crystallographic orientation of nuclei) [105].

Carpenter and Elam [106] and Alterthum [107] showed that the stored energy of the dislocations (ρ), due to deformation, provides the driving force for recrystallization and is affected by the strain (deformation) and temperature. The energetics of recrystallization imply that if a grain boundary element of area dA is displaced by dx, the Gibbs free energy dG will be changed by:

$$dG = -\rho dA dx = -\rho dV \quad \textbf{(32)}$$

Therefore, during recrystallization as energy in the system is reduced, dislocations are swept as grain boundaries move, resulting in lower dislocation density in the material and a change in the material texture. This also results in the change in grain size and texture of the resulting material.

3.2 Modelling Static Recrystallization

Recrystallization has been modelled using analytical and numerical methods [108]. Analytical methods such as JMAK usually simulate recrystallized volume fraction in the material [109]. Sandström et al. [110] have presented a subgrain growth model during annealing and applied it to pure and two-phase materials. Additionally, analytical models that account for the stress-strain behavior and grain size have been used successfully to account for dynamic recovery and predict the stress-strain response [111].

Analytical methods provide fast solutions but are limited in their applications, since they cannot predict the local texture evolution and material response because they look at the overall material response. Numerical methods provide a flexible robust solution and have been used to model a variety of annealing and recrystallization problems. These range from, Anderson et al. [112], who have simulated grain growth in 2D, whereas Srolovitz et al. [113] and Popova et al. [114] have shown to predict nucleation and growth during SRX and DRX respectively. Most common numerical models namely; Monte Carlo method, phase-field models, vertex models and cellular automata models are briefly discussed below.

3.2.1 Johnson Mehl Avrami Kolmogorov (JMAK) Approach

Analytical approaches used to simulate recrystallization focus on volume fraction of recrystallized grains (X_v). These approaches are easy to implement and provide fast and accurate solutions to many problems. However, these approaches make a lot of assumptions such as constant grain growth, etc.

The JMAK approach proposed by Johnson and Mehl [115], Avrami [116, 117] and Kolmogorov [118] in separate works, and modified by Sebald and Gottstein [119] is commonly used to simulate recrystallization problems. JMAK model works by assuming random nuclei with each nuclei growing as spherical grains with constant growth rate for all grains written as:

$$X_v = 1 - exp(-Bt^n) \tag{33}$$

where X_v is the volume fraction of recrystallized grains and $B$and n are temperature dependent and independent constants. JMAK models give the growth rate of recrystallized region as a function of time. The exponent n can also be associated with dimensionality of the problem. For a truly random site saturated (no nucleation during grain growth) nucleation, the exponent will be close 3. Thus indicating that the new grains grow as spheres. A departure from this would indicate non-random nuclei placement or early impingement of the new grains.

3.2.2 Monte Carlo Models

Models that involve random number sequences to find approximate solutions are known as the Markov chain Monte Carlo (MCMC) models [120] and have been used to simulate all kind of problems including recrystallization (e.g. Potts Model [121]). In Markov chain models, step at time $(t + 1)$ is only determined by the previous step at time (t) and the previous history does not have any bearing on the following step.

The Potts model [121] is derived from the Monte Carlo model and is an extension of the Ising model [122]. Monte Carlo models divide the domain into subdomains (sites) with unique indices and state variables [84]. This helps in clearly identifying grain boundaries between two subdomains (Figure 14). The energy (E) of the system is defined as:

$$E = \sum_{i=1}^{N}\left[\sum_{j=1}^{n}\frac{1}{2}\gamma(s_i, s_j) + E_s(s_i)\right] \quad \textbf{(34)}$$

where E_s is the stored energy, $\gamma(s_i, s_j)$ is the boundary energy which is a function of the current site (s_i) and neighboring sites (s_j) and N and n are the total number of sites and neighbors for each site.

The kinetics of growth in the Monte Carlo method are controlled via a probabilistic approach that describes how a site is recrystallized by its neighbor. Using the Metropolis method [123], the transition probability P at a certain temperature T is based on the change in energy between the current site and its neighbor j and is given by:

$$P = \begin{cases} 1 & \Delta E \leq 0 \\ exp\left(-\frac{\Delta E}{2kT}\right) & \Delta E > 0 \end{cases} \quad \textbf{(35)}$$

where k is the boltzman constant.

Another way to calculate the transition probability is the symmetric method and is given as [124]:

$$P(\Delta E) = \frac{1}{2}tanh\left(-\frac{\Delta E}{2kT}\right) \quad \textbf{(36)}$$

Figure 14: Schematic representation of domain and subdomains used in Monte Carlo method [125]

The algorithm proceeds by allowing every site in the domain a chance to flip or change the spin. However, based on Equation 35, only those moves that reduce the system energy are accepted.

3.2.3 Phase Field Models

Phase field models use continuous parameters to describe each simulation cell at each time step [126]. The basic algorithm is formulated to reduce the total free energy within each cell. Total free energy ($F(t)$) proposed by Chen [127] is given as:

$$F(t) = \int [f_0(\eta_1(r,t), \eta_2(r,t), \ldots., \eta_Q(r,t)) + \sum_{q=1}^{Q} \frac{K_q}{2} (\nabla \eta_q(r,t))^2] \, dr \quad \textbf{(37)}$$

where $\eta_q(r,t)$ are the set of order parameters at position r and time $t$and f_0 is the local free energy density.

Phase-field models represent grain boundaries as different phase with different gradients across the structural order parameters (Figure 15). These models can be computationally expensive as many iterations could be required to reach the minimal energy for the system.

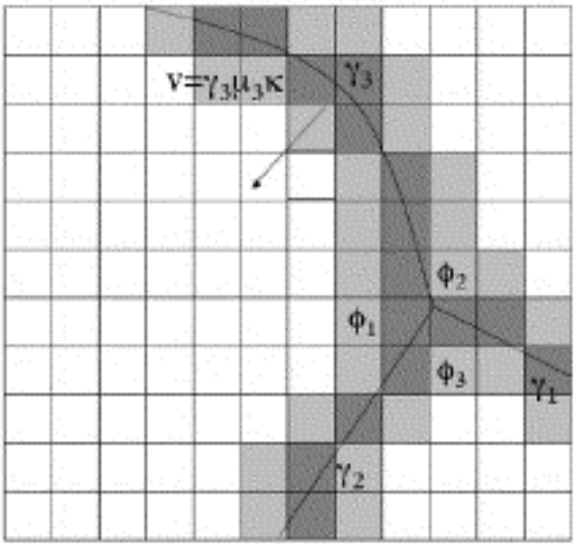

Figure 15: Grain growth simulation in phase-field models. Grain boundaries show high gradient [128]

Phase field models have been used to simulate 2D grain growth [127, 129] and can easily incorporate the effects of mobility, grain boundary energy and boundary plane orientation. Dynamic recrystallization with phase-field models has also been performed [130] to predict the stress-strain response and texture evolution during DRX.

3.2.4 Vertex Models

In vertex models, grain boundaries are based on local grain boundary curvature and are treated as continuous interfaces so that:

$$v = \mu(\theta, T), \gamma(\theta, T)\kappa \quad \textbf{(38)}$$

where v is the migration velocity, μ is the grain boundary mobility, γ is the surface tension of the grain boundary, κ is the local grain boundary curvature, and θ and T are the misorientation and temperatures respectively.

In vertex models, the grain boundaries are discretized and 'tracked' by a variable number of points and move perpendicular to the boundary plane to simulate grain growth. The corresponding nodes are repositioned accordingly based on normal or special (triple points) grain boundary features (Figure 16). Vertex models typically assume local equilibrium at grain boundary junctions to find angle between two nodes.

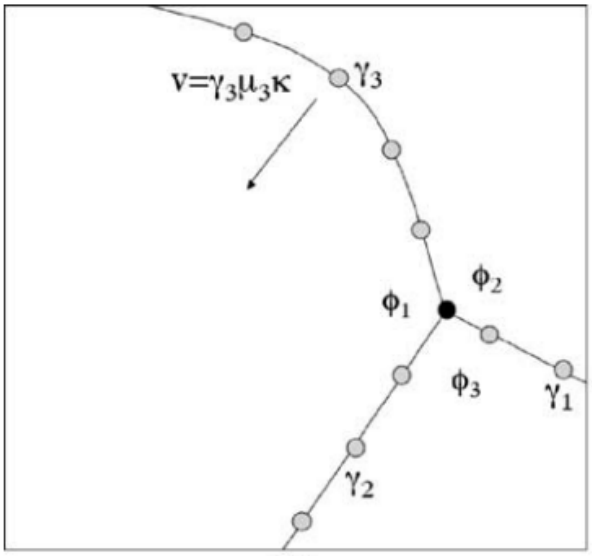

Figure 16: Grain growth simulation in vertex models [128]

Vertex models in 2D have been used to simulate grain growth [131] and recrystallization in cold rolled copper [132]. However, application to 3D becomes technically and computationally expensive as grain boundaries are represented as surfaces. This increases the topological changes due to grain growth, hence complicating the problem [133]. Weygand et al. [134] have simulated 3D grain growth using vertex models.

3.2.5 Cellular Automata Models

Due to its flexibility, cellular automata models (CA) are used extensively in literature to simulate recrystallization problems [135]. CA method discretizes the time and physical space where discrete point is known as a cell. Each cell is assigned its own state variables which can be constant or evolve with time. In recrystallization problems, dislocation density and cell orientations are chosen as state variables [114]. Based on the local driving forces, CA models can be easily adapted to 2D [114] and 3D [136] problems with different types of neighborhood [114, 135] and can easily incorporate the effect of grain boundaries (Figure 17) as region between 2 neighboring cells or a grain boundary region. As CA models are discretized into cells, their implementation to Finite Element Analysis is relatively easy as each element can be treated as a cell and have been used to model SRX [137] and DRX problems [114]. Monte Carlo (MC) models can also be discretized into cells but as MC models offer random texture update, it is very important and challenging to correctly define the nucleation sites. However, Raabe [138] have successfully used MC models for simulating SRX problems in aluminum.

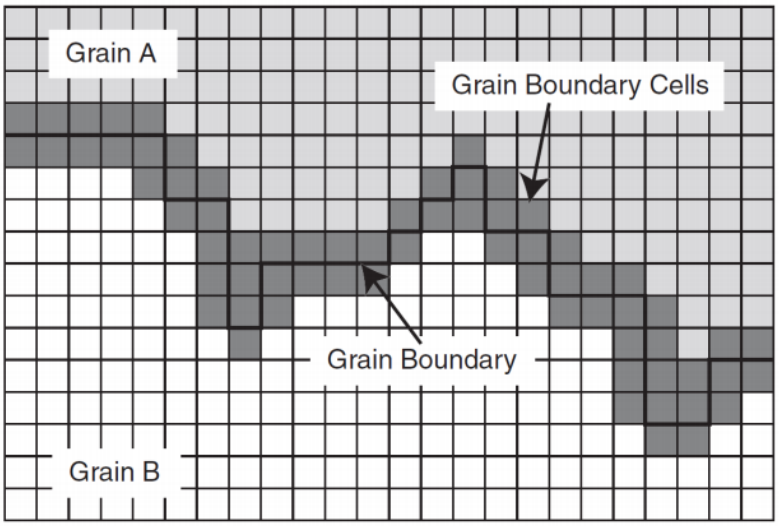

Figure 17: Grain boundaries in cellular automata models [139]

Unlike Monte Carlo models, CA models can easily update all the cells simultaneously [114]. Each neighboring cell is recrystallized based on a switching rule and takes on the state variables of its neighbors when recrystallized. Raabe and Becker [138] have stated the switching rule as:

$$\dot{x} = n v_D \lambda_{gb} c \left\{ exp\left(-\frac{\Delta G + \Delta G_t/2}{k_B T}\right) - exp\left(\frac{\Delta G - \Delta G_t/2}{k_B T}\right) \right\} \quad (39)$$

where $\dot{x}$ is the grain boundary velocity, $v_D$is the Debye frequency which is a constant for a given crystal, $\lambda_{gb}$is the jump width through the grain boundary, c is the intrinsic concentration of grain boundary vacancies, n is the normal of the grain boundary, ΔG is the Gibbs enthalpy of motion, ΔG_t is the Gibbs enthalpy of transformation, $k_B$is the Boltzman constant and $T$is the temperature [138]. As is presented in this work, this state switch can also be done using a probabilistic step. Probabilistic step allows for a simpler approach with the same level of accuracy as a boundary dynamics model [140]. State switch in probabilistic CA is based on probability of a random number [114, 138] and is explained in next chapter.

3.3 Summary

Various approaches to model static recrystallization are presented in this section. SRX approaches can be broken down into analytical and numerical models. Analytical models like the JMAK approach provide fast solutions but are limited as they cannot predict the complete texture evolution. On the other hand, numerical models are relatively slow but robust and flexible.

Monte Carlo Potts models are one of the most widely used numerical models to simulate SRX. Monte Carlo models divide the model domain into subdomains with unique indices to identify grain boundaries. Monte Carlo model kinetics calculate the system energy and try to minimize it by using various approaches such as probabilistic step approach.

Phase field and Vertex models use mesh gradients and curvature to represent grain boundaries. Phase field models can be computationally expensive as it can take multiple iterations to reach the minimal energy. Similarly, Vertex models can be computationally challenging in 3D, as Vertex models simulate grain boundaries as surfaces which evolve as grains grow in the system.

Lastly, Cellular Automata (CA) models offer a flexible solution to model SRX and have been used to model all kinds of SRX problems. CA models discretize the time and physical space and assign a state to each cell. This state governs the function of each cell (nucleus, recrystallized, etc.) and its neighbors to achieve the final microstructure. Even though CA models work on stored energy, they can easily be adapted to work on boundary curvature problems by using an advanced probabilistic step [141]. More details about the SRX model used in this work are presented in Section 5.2.

Chapter 4
Scope and Objectives

Literature review performed in Chapter 2 discusses the various crystal plasticity techniques used in literature. In addition, various numerical models used to simulate crystal plasticity problems have also been discussed along with texture and microstructure implementation in these numerical models. Chapter 3 discusses the various numerical techniques used to model static recrystallization along with some experimental insight. Background information about various numerical models discussed in the previous sections provides the layout for the current work.

The main objective of this research is to provide a framework to model large strain processes namely; cold rolling and hot compression. The research framework shown in Figure 18 shows that in this thesis, cold rolling and hot compression are modelled using a crystal plasticity model that takes in inputs as texture, loading and boundary conditions. The model then calculates the final microstructure and stress-strain data.

Cold rolling (Section 5.1) simulations are performed using an Element Free Galerkin Crystal Plasticity model in commercial software LS-DYNA on AA 5754. Crystal plasticity framework is implemented in LS-DYNA EFG formulation. Cold rolling simulations account for the complete through thickness of the sheet and are validated with experimental results from Jin and Lloyd [142]. To analyze various grain metrics, an in-house grain analysis code (gCode) is developed. In house gCode is used to analyze various through thickness subgrain metrics during cold rolling (Figure 18). As rolling is often simulated with plane strain compression, plane strain compression simulations are also performed and compared with rolling simulations to access the validity of this assumption.

Hot compression (Section 5.2) simulations are performed on AA 6063 using an in-house Taylor based crystal plasticity model at various temperatures and strain-rates. Crystal plasticity hardening model is modified to include the effects of temperature and strain-rate. As AA 6xxx undergo static recrystallization at high temperatures, an in-house integration point based static recrystallization code is developed (Figure 18). Stress-strain response from the crystal plasticity model and texture and grain size results from static recrystallization model are validated with experimental results.

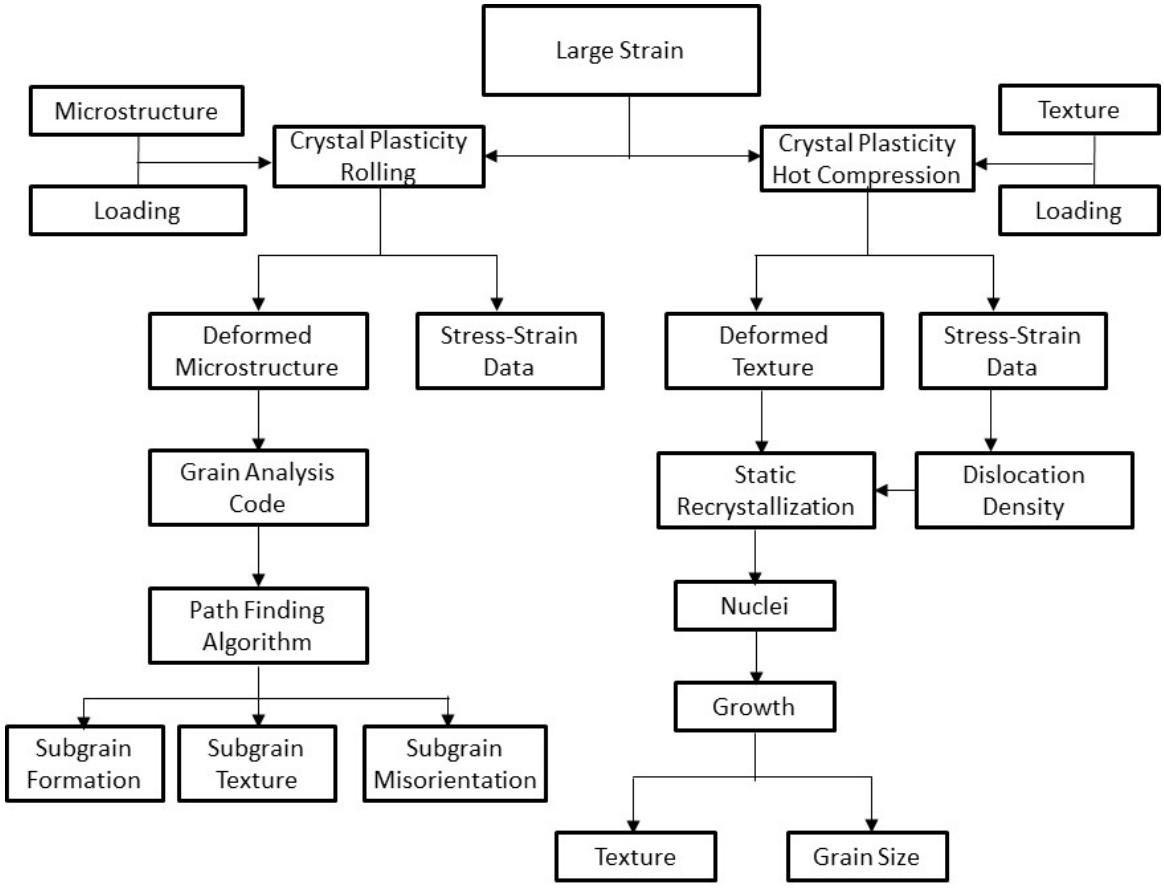

Figure 18: Research framework

Detailed objectives of this research are summarized below:

- Develop numerical models based on Crystal Plasticity Theory to simulate large strain phenomena as well as the effects of temperature and strain-rates on large deformations in polycrystalline metals
- Develop a numerical framework based on crystal plasticity theory for through process modelling
- Investigate evolution of microstructure (morphology, texture, etc.) during cold rolling
- Investigate evolution of microstructure (static recrystallization, etc.) during hot compression

Chapter 5
Modelling Frameworks

5.1 Crystal Plasticity Formulation

Total deformation of a single crystal is the result of two mechanisms; crystallographic slip due to dislocation motion and elastic lattice distortion [143]. Within an FCC crystal, plastic deformation occurs by crystallographic slip on twelve [1 1 1] <1 1 0> slip systems (α). Slip planes have normals (m) [1 1 1] and slip directions with shear directions (s) <1 1 0>. Plastic deformation is defined to occur as a set of simple shears (plastic) along various slip systems. This leaves the lattice and slip system vectors ($s_{(\alpha)}, m_{(\alpha)}$) undistorted and unrotated. The material and lattice are also considered to deform elastically and rotate rigidly from the plastically deformed state to current configuration (Figure 19). This formulation is used to decompose the deformation gradient (F) into the elastic and plastic parts to achieve the final deformation.

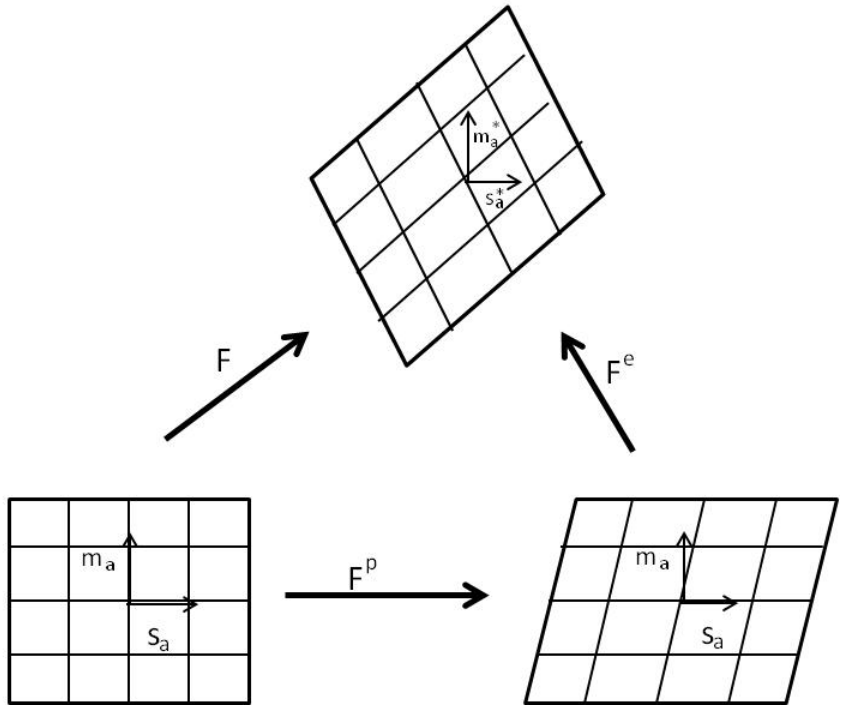

Figure 19: Decomposition of deformation gradient matrix F

Due to the decomposition of deformation tensor (F), the deformation tensor is written as:

$$F = F^e F^p \quad \textbf{(40)}$$

where F^p is the plastic part of the deformation gradient and consists solely of crystallographic slip along any specific slip system and F^e is the elastic part of the deformation gradient and includes rigid body rotation. From (40), the spatial gradient of velocity (L) can be written as:

$$L = \dot{F}F^{-1} = L^e + L^p \tag{41}$$

where L^e and L^p are the elastic and plastic parts of the spatial gradient of velocity and defined as:

$$L^e = \dot{F}^e F^{e-1}, L^p = F^e (\dot{F}^p F^{p-1}) F^{e-1} \tag{42}$$

The vectors $s_{(\alpha)}$ and $b_{(\alpha)}$ are regarded as lattice vectors and therefore they rotate and stretch by:

$$s^e_{(\alpha)} = F^e s_{(\alpha)}, b^e_{(\alpha)} = b_{(\alpha)} F^{e-1} \tag{43}$$

Taking the symmetric and antisymmetric parts of (40) and (41) results in the elastic and plastic strain-rates D^e and D^p, and plastic spin (N^p) and elastic spin (N^e) associated with rigid lattice rotation.

$$D = D^e + D^p, N = N^e + N^p \tag{44}$$

where,

$$D^p = \sum_{\alpha=1}^{n} \dot{\gamma}_{(\alpha)} \frac{1}{2} \left(s^e_{(\alpha)} \otimes b^e_{(\alpha)} + b^e_{(\alpha)} \otimes s^e_{(\alpha)} \right) \tag{45}$$

and

$$N^p = \sum_{\alpha=1}^{n} \dot{\gamma}_{(\alpha)} \frac{1}{2} \left(s^e_{(\alpha)} \otimes b^e_{(\alpha)} - b^e_{(\alpha)} \otimes s^e_{(\alpha)} \right) \tag{46}$$

By introducing the following the symmetric and skew symmetric tensors for each slip system (α)

$$P_{(\alpha)} = \frac{1}{2} \left(s^e_{(\alpha)} \otimes b^e_{(\alpha)} + b^e_{(\alpha)} \otimes s^e_{(\alpha)} \right) \tag{47}$$

$$W_{(\alpha)} = \frac{1}{2} \left(s^e_{(\alpha)} \otimes b^e_{(\alpha)} - b^e_{(\alpha)} \otimes s^e_{(\alpha)} \right) \tag{48}$$

The plastic strain-rate (D^p) and plastic spin (N^p) for the crystal can be defined as:

$$D^p = \sum_{\alpha} P_{(\alpha)} \dot{\gamma}_{(\alpha)}, N^p = \sum_{\alpha} W_{(\alpha)} \dot{\gamma}_{(\alpha)} \tag{49}$$

where $\dot{\gamma}$ is the shear rate on any slip system α.

The elastic constitutive equation for a crystal is specified by:

$$\hat{\tau}^e = \dot{\tau} - N^e\tau + \tau N^e = ED^e \tag{50}$$

where $\hat{\tau}^e$ is the Jaumann rate of Kirchhoff stress tensor (τ) based on the lattice rotations and E is the tensor of elastic moduli. These elastic moduli are based on the anisotropic elastic constants of a material crystal and exhibit the appropriate crystal symmetry. Elastic moduli for this work are for FCC polycrystals reported in literature. Use of E is a simplification of the work presented by Asaro and Needleman [42] by using an explicit small time-step finite element implementation. An implicit method with rate-tangent would use a different form of these moduli.

In order to represent (50) in terms of the Jaumann rate $\hat{\sigma}$ of Cauchy stress $\sigma = \det(F^{-1})\tau$, based on continuum slip (W), we introduce a second order tensor $R_{(\alpha)}$for each slip systemα.

$$R_{(\alpha)} = EP_{(\alpha)} + W_{(\alpha)}\sigma - \sigma W_{(\alpha)} \tag{51}$$

Using (44) - (49) and (51), the elastic constitutive equation can be written as:

$$\hat{\sigma} = ED - \dot{\sigma}_0 - \sigma\, trD \tag{52}$$

where $\hat{\sigma}$ is the Jaumann rate of Cauchy stress, E is the elastic stress tensor, D is the strain-rate tensor and $\dot{\sigma}_0$ is the viscoplastic type stress state based on slip rates defined by:

$$\dot{\sigma}_0 = \sum_{\alpha} R_{(\alpha)}\dot{\gamma}_{(\alpha)} \tag{53}$$

Slip rates ($\dot{\gamma}$) are governed by the power law expression given below and are substituted in (53).

$$\dot{\gamma}_{(\alpha)} = \dot{\gamma}_0 sgn\ \tau_{(\alpha)} \left|\frac{\tau_{(\alpha)}}{g_{(\alpha)}}\right|^{1/m} \tag{54}$$

where $\dot{\gamma}_0$ is the reference shear rate taken to be the same from all slip systems, $\tau_{(\alpha)}$is the resolved shear stress on each slip system, $g_{(\alpha)}$is the hardness of each slip system and incorporates single crystal hardening and m is the strain-rate sensitivity index which is also taken to be the same for each slip system. $\tau_{(\alpha)}$ is defined as :

$$\tau_{(\alpha)} = P_{(\alpha)} : \sigma \tag{55}$$

The rate of slip system hardness is defined by:

$$\dot{g}_{(\alpha)} = \sum_{\beta} h_{(\alpha\beta)} \left|\dot{\gamma}_{(\beta)}\right| \tag{56}$$

where $g_{(\alpha)}(0)$ is the initial hardness of any slip system and is taken to be a constant (τ_0) and $h_{\alpha\beta}$ are the hardening moduli such as:

$$\mathrm{h}_{(\alpha\beta)} = \mathrm{q}_{(\alpha\beta)}\mathrm{h}_{(\beta)} \text{ (no sum on } \beta) \tag{57}$$

where h_β is the hardening rate of a single crystal and $q_{(\alpha\beta)}$ is the matrix that defines the latent hardening behavior of the crystal. For FCC crystals, $q_{(\alpha\beta)}$ is defined by [42] as:

$$q_{(\alpha\beta)} = \begin{bmatrix} A & qA & qA & qA \\ qA & qA & qA & qA \\ qA & qA & qA & qA \\ qA & qA & qA & A \end{bmatrix} \tag{58}$$

where q is the ratio of the latent hardening rate to self-hardening rate and A is a 3 x 3 unity matrix. This is because slip systems [1 -12] are coplanar. Thus the ratio of the latent hardening rates to the self-hardening rates are taken as unity.

Asaro and Needleman [42] and some others take each $g_{(\alpha)}$as a function of accumulated slips $\gamma_{(\alpha)}$;

$$g_{(\alpha)} = g_{(\alpha)}(\gamma_\alpha) \tag{59}$$

Where

$$\gamma_{(\alpha)} = \int_0^t \sum_{\alpha} \left|\dot{\gamma}_{(\alpha)}\right| dt \tag{60}$$

Pierce et al. [144] take the single slip hardening to be a function of $\gamma_{(\alpha)}$expressed as:

$$h_{(\beta)} = h_0 \left(\frac{h_0 \gamma_{(\alpha)}}{\tau_{(\alpha)} n} + 1\right)^{n-1} \tag{61}$$

where h_0 is the initial hardening rate, γ_α is the accumulated slip on a slip system and n is the hardening exponent.

In an explicit small time-step formulation, once N^e is known, the orientation of the crystal is updated using the orientation matrix. The orientation matrix (Q) rotates the crystal axis into the global system.

Orientation in an explicit formulation is then updated using the method of Raphanel et al. [145] given as:

$$Q_{n+1} = e^{N^e Dt} Q_n \tag{62}$$

where $e^{N^e Dt}$ is obtained using the Euler-Rodrigues formula;

$$e^{N^e Dt} = I + \frac{\sin n^e \Delta t}{n^e} N^e + \frac{1 - \cos n^e \Delta t}{(n^e)^2} N^e N^e \tag{63}$$

where $n^e = \sqrt{(N_{ij} N_{ij})/2}$.

Euler angles $(\emptyset_1, \emptyset, \emptyset_2)$ in Bunge's notation are calculated from the updated orientation matrix. Euler angles are stored and are used to track the evolution of texture in the material [78].

Finite element models mostly use an explicit time scheme which use small time steps to insure stability. However, semi-implicit Taylor type models use the rate tangent method developed by Pierce et al [144] where the slip increment ($\Delta\gamma_{(\alpha)}$) used in the slip-rate law (Equation 54) is written as:

$$\Delta\gamma_{(\alpha)} = \gamma_{(\alpha)}(t + \Delta t) - \gamma_{(\alpha)}(t) \tag{64}$$

A linear interpolation results in:

$$\Delta\gamma_{(\alpha)} = [(1 - \theta)\dot{\gamma}_{(\alpha)}(t) + \theta\dot{\gamma}_{(\alpha)}\,(t + \Delta t)]\Delta t \tag{65}$$

where Δt is the time increment and θ is a fitting parameter between 0 and 1.

In a typical Taylor type formulation, once N^e is known, orientation update is calculated using a T-Matrix. Where a Z-X-Z T-Matrix is defined from Euler angles as:

$$Tm_{ZXZ} = \begin{bmatrix} c_1c_3 - c_2s_1s_3 & -c_1s_3 - c_2c_3s_1 & s_1s_2 \\ c_3s_1 + c_1c_2s_3 & c_1c_2c_3 - s_1s_3 & -c_1s_2 \\ s_2s_3 & c_3s_2 & c_2 \end{bmatrix} \tag{66}$$

where Tm is the T-matrix and $c_{1,2,3}$and $s_{1,2,3}$represent the cosine and sine of $\emptyset_1, \emptyset, \emptyset_2$ respectively and is updated using:

$$Tm' = TmN^e \tag{67}$$

where Tm' is the updated T-matrix.

5.2 Probabilistic Integration Point Static Recrystallization (SRX) Model

Based on the material at hand, deformations at elevated temperatures can cause static and dynamic recrystallization. A probabilistic integration point based model is presented for simulating static recrystallization in FCC metals. This approach is closer to statistical JMAK models [109] and uses the outputs from crystal plasticity simulations. The proposed approach can be divided into two parts; (a) nucleation and (b) growth of nuclei. Proposed model uses the texture and resolved shear stress data from crystal plasticity simulations to predict nucleation and growth which is used to predict the final textures and grain size.

Nucleation and grain growth are directly affected by neighbors. Raabe et al. [135] have used a cellular automata concept where a cell is composed of one or several elements. The cell defines sites for possible nucleation and grain growth. Popova et al. [114] have used an extension of Raabe et al. [135] for 2D simulations where each element is considered a cell to simulate DRX in Mg alloys. They have considered Von Neumann and Moore neighboring schemes which result in 4 and 8 neighbors to each element respectively. This work, unlike the works mentioned previously, uses the Avrami type approach [109] where all points are neighbors with all the other points in the simulation.

5.2.1 Nucleation

Cahn et al. [146] introduced the concept of nuclei during recrystallization based on dislocation density. In their work [146], nuclei were identified as areas of high dislocation density and areas with high dislocation mismatch with surroundings (Figure 20).

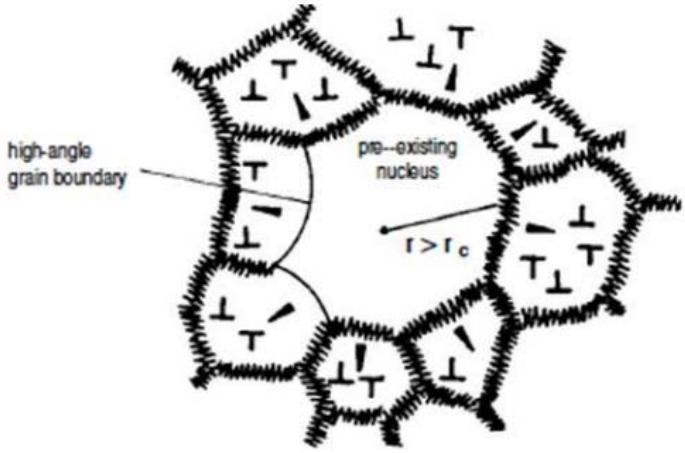

Figure 20: Schematic representation of the nucleus [147]

Experimental observations also show nuclei/subgrains growing and sweeping the dislocations to form clean grains as shown in Figure 20 [104]. Literature presents several critical conditions to predict nuclei; based on the critical value of dislocation content [148] or a critical subgrain size [149] which can also be attributed to high angle grain boundaries. These are in-line with experimental observations that show formation and growth of subgrains in materials [104]. Nucleation criterion presented in literature [150] based on dislocation "jump" between neighbors i and j is calculated as:

$$d||\alpha^N|| = ||\alpha_i^N|| - ||\alpha_j^N|| \quad \textbf{(68)}$$

where α^N is the Nye tensor [151] and is defined as:

$$\alpha^N = \frac{1}{b}\nabla \times F^P \quad \textbf{(69)}$$

where F^P is the plastic part of the deformation gradient and b is the magnitude of burgers vector.

Instead of using the Nye tensor, Arsenlis and Parks [152] accounted for the dislocation density by distributing it into screw and edge dislocations on each slip system (α) as:

$$\rho_{GN(e)}^{\alpha} b = -\nabla\gamma^{\alpha}.\mathrm{m}^{\alpha} = \gamma_{,k}^{\alpha}\mathrm{s}_k^{\alpha} \quad \textbf{(70)}$$

$$\rho_{GN(s)}^{\alpha} b = \nabla\gamma^{\alpha}.\mathrm{n}^{\alpha} = \gamma_{,k}^{\alpha}\mathrm{n}_k^{\alpha}$$

where e and s are for edge and screw dislocations respectively. This approach gives a simpler method to calculate the contribution of each slip plane and also the total dislocation density as:

$$\rho_{GN}^{\alpha} = \sqrt{\left(\rho_{GN(e)}^{\alpha}\right)^2 + \left(\rho_{GN(s)}^{\alpha}\right)^2} \quad \textbf{(71)}$$

Yet another way to calculate the dislocation density based on obstacle spacing is presented by Humphreys and Hatherly [104] and Murr and Kuhlmann-Wilsdorf [153] as:

$$\tau = a\mu b\sqrt{\rho} \quad \textbf{(72)}$$

where τ is the resolved shear stress, μ is the shear modulus and a is the obstacle strength. This methodology is used in this work to find the dislocation density as the resolved shear stress is available from simulation data.

In this work, the initiation of SRX (nuclei formation) is assumed to occur at high angle grain boundaries greater than a critical misorientation angle (θ_{cr}). These possible nucleation sites are given a probabilistic chance of being a nucleus if they have reached a critical dislocation density (ρ_{cr}) and are above a threshold dislocation density with their neighbors.

The critical dislocation density (ρ_{cr}) was first given by Roberts and Ahlblom [149] for subgrain building. It was then used as a nucleation criteria in many studies (e.g. [114, 130]) and is given as:

$$\rho_{cr} = \left(\frac{20S\dot{\varepsilon}}{3bLM\lambda^2}\right)^{1/3} \quad \textbf{(73)}$$

where S is the Read and Shockley [154] grain boundary energy per unit area, $\dot{\varepsilon}$ is the strain-rate, L is the dislocation mean free path and is given by:

$$L = K/c_2\sqrt{\rho} \quad \textbf{(74)}$$

M is the grain boundary mobility and is given by:

$$M = M_o\, exp\left(\frac{H_m}{kT}\right) \quad \textbf{(75)}$$

and λ is the dislocation line energy and is given by:

$$\lambda = c\mu b^2 \quad \textbf{(76)}$$

where K, c_2 and c are fitting parameters, H_m is the activation enthalpy, k is the Boltzman constant, T is the temperature and a Heaviside step function at 15^0 is used to represent the pre-factor M_o that follows experimental observations [104]. A generalized mobility curve was introduced by Humphreys and Hatherly [104] and is shown in Figure 21.

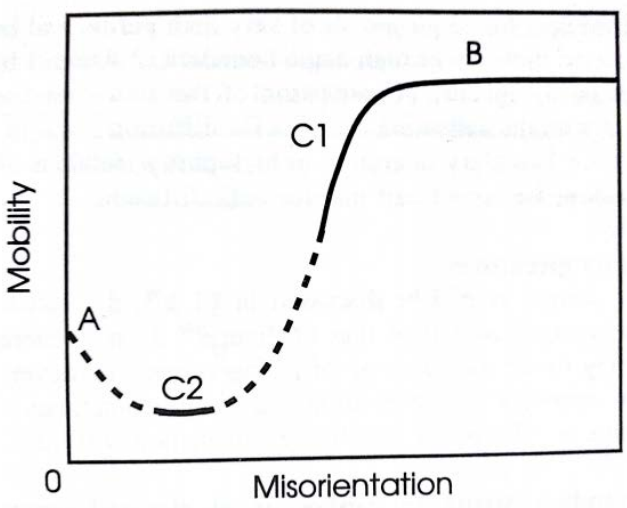

Figure 21: Schematic diagram of possible distribution of mobility function [104]

The dislocation "jump" concept introduced by Brahme et al. [150] for neighboring elements i and j is also used in this work. The dislocation jump between neighboring elements is calculated as:

$$d\rho_{ij} = \rho_i - \rho_j \tag{77}$$

where ρ_i and $\rho_j$are the dislocation densities of neighboring points i and j respectively. Nucleation requires this dislocation jump to be greater than a critical dislocation density mismatch $d\rho_{cr}$which is defined as:

$$d\rho_{cr} = C_0\rho_{max} \tag{78}$$

where $C_0$is a fitting parameter that ranges from 0.1 to 0.9. This critical mismatch controls the number of nuclei formed in the deformed sample and is kept constant for all simulations.

After the potential nuclei are identified using the conditions mentioned above, a probabilistic switching step is performed to identify viable nuclei with the highest probability of growing. The switching parameter (ω_{switch}) used to identify the viable nuclei is based on grain boundary velocity (v) and is defined as:

$$\omega_{switch} = \frac{v_i^j}{v_{max}} \tag{79}$$

where $\omega_{switch}$is the switching parameter, $v_i^j$is the grain boundary velocity of point i with respect to neighbor j and $v_{max}$is the maximum grain boundary velocity in the simulation.

Switching parameter is compared to a random number ξ between 0 and 1 and switching is performed if:

$$\omega_{switch} \geq \zeta \tag{80}$$

The switched nuclei are identified as viable nuclei and are used for grain growth as discussed in the next section.

5.2.2 Grain Growth

The next step (after identifying the viable nuclei) is grain growth. A nucleus eats any neighboring point that results in maximum reduction in energy. Assuming 100% recrystallization, each nucleus corresponds to a new grain after recrystallization. The driving force for recrystallization is the grain boundary velocity (v) which is based on the stored dislocations and is defined as:

$$v = MP \tag{81}$$

where v is the grain boundary velocity, $M$is the temperature dependent mobility as described in the previous section and $P$is the stored energy.

Based on the work by Gottstein and Shvindlerman [147], the stored energy is calculated as:

$$P = \frac{1}{2}\rho\mu b^2 \tag{82}$$

where μ is the shear modulus.

To identify the viable growth path for the nuclei, a probabilistic step is taken to define growth. Growth happens as nuclei consume their neighbors based on a switching parameter. The switching parameter (ω_{switch}) is calculated for all potential points of growth as:

$$\omega_{switch} = N_f \frac{v_i^j}{v_{max}} \tag{83}$$

where N_f is the neighbor factor used in recrystallization models based on the type of neighbor (von Newmann or Moore) [114]. N_f is taken as 1 for von Newmann whereas N_f is taken as 1 for nearest neighbors and 0.48 for second nearest neighbors in More neighborhood models [114].

Switching parameter is compared to a random number ξ between 0 and 1 and switching is performed if:

$$\omega_{switch} \geq \zeta \tag{84}$$

This probabilistic step ensures that only one neighbor will be recrystallized in one recrystallization step.

5.3 Summary

Various numerical approaches namely; Crystal Plasticity and Probabilistic Integration Point based Static Recrystallization are explained in this Chapter. Rate-dependent crystal plasticity formulation used in this thesis accounts for crystallographic slip in FCC metals. Plastic deformation on these slip systems is defined as a set of simple shears and is used to calculate the stress-strain as well as the crystallographic rotation of each grain. More details about the crystal plasticity framework and its application is presented in Section 6.1.

As many AA 6xxx alloys undergo SRX at high temperatures, crystal plasticity simulations by themselves are unable to capture the final texture. Therefore a SRX model was developed to model the final texture and grain size. SRX model used in this work is divided into two parts; (a) nucleation (b) growth of nuclei. The model uses texture and resolved shear stress as inputs from crystal plasticity to identify the possible nuclei based on a few criteria. Next, the model uses the stored energy in the model for growth of these nuclei to find the final texture and grain size. More details about the SRX model and its implementation are presented in Section 6.3.

Chapter 6

Application to Large Strain Deformation Processes

6.1 Rolling

Rolling is defined as a processes of plastically deforming any material between two rolls (Figure 22). It is used extensively in manufacturing processes to produce sheets of metals [155]. These sheets are further processed and made into different parts by forming operations such as stamping. The metal is subjected to high compressive and shear stresses due to friction from the rolls. Rolling is further classified into cold and hot rolling based on the operating temperature [156].

Hot rolling is done to breakdown the ingots into billets and further into sheets, bars, etc. Hot rolling in aluminum alloys is done around 500^{o}C which is above the recrystallization temperature [24] and hence makes it easier to deform the material. However hot rolling does not produce good surface finish due to surface oxidation in some metals. Cold rolling is done below recrystallization temperature of the metal and is used to further roll hot rolled sheets. This improves the surface finish and increases the strength of the sheet metal [35]. Many combinations of rolling variables are used to fabricate sheets that can have deep drawability and stretchability by varying the grain size, texture, etc. [157].

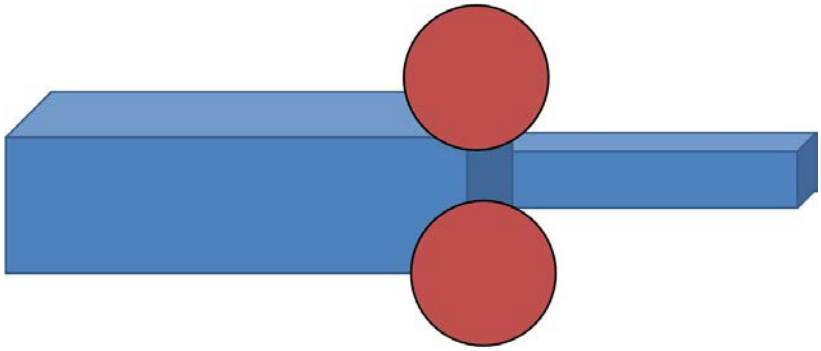

Figure 22: Simple rolling setup

Fundamental concept in a rolling process assumes constant velocity of rolls. This is also called symmetric rolling. On the other hand asymmetric rolling assumes different roll velocities or roll diameters. It is also assumed that the material extends only in the rolling direction with no increase in width of the sheet and that the cross-sectional area is not distorted. This leads to:

$$h_0 v_0 = h_f v_f \tag{85}$$

where h and v are the sheet thickness and sheet velocity at before and after rolling respectively.

6.1.1 Simulating and Analyzing Cold Rolling

Roller velocities and friction lead to variable velocity profile across the sheet thickness. Therefore it is important to consider the through thickness variation in strain and texture distribution in the rolled sheet [21, 158–160]. Jung et al. [161] attributed this variation to the different shear and compressions experienced by different material layers during deformation. Finite element based phenomenological models have tried to account for the through thickness effects in the sheet [160, 162]. Roumina et al. [160] have showed the through thickness shear strain distribution during symmetric and asymmetric rolling. Phenomenological models can capture the stress-strain behavior but are unable to capture the microstructural effects (grain size, shape, breakage, texture evolution, etc.) in the sheet. Microstructure effects are important to capture as they contribute to the material behavior during subsequent forming.

As phenomenological models are unable to capture microstructural evolution, crystal plasticity models, such as the Taylor model, self-consistent (VPSC) and CPFEM, are typically used to account for microstructure evolution. Hirsch et al. [19] and others [7, 163, 164] have correctly predicted rolling textures for AA 1100 and AA 1050 using Taylor type models. Bozzolo et al. [165] have predicted rolled textures for pure titanium using VPSC. Mathur and Dawson [7] have used a finite element approach to simulate rolling under the Taylor assumption [38] and can capture the textures accurately. However, they are unable to account for microstructure information (e.g. grain breakage). All these approaches can accurately capture the texture and stress-strain distribution but are unable to capture the microstructure evolution such as grain size, grain breakage/refinement, grain shape, etc. without applying additional constraints.

Full field crystal plasticity finite element models offer a viable solution and can capture the complete microstructural information. Rossiter et al [62] and Delannay et al. [166] have accurately predicted the microstructure evolution for AA 5754 and ULC steel respectively. However, finite element models have their limitations at large strains due to element distortion [23, 70]. Element Free Galerkin (EFG) methods provide effective solution with higher accuracy. In addition, EFG methods do not have element connectivity like conventional finite elements and can easily accommodate large strains (Section 2.2.3).

A rate-dependent full-field Crystal Plasticity Element Free Galerkin model (CPEFG - Section 4.1) [62, 167] was used to simulate cold rolling in LS-DYNA for AA 5754. CPEFG model was validated with literature data [168, 142] and captured the complete through thickness information (stress-strain,

grain size, shape distribution and texture). Simulated results highlight the importance of capturing the complete through thickness model to simulate cold rolling.

6.1.2 EFG Implementation

CPFEM has been used extensively to model various deformations. However, CPFEM models cannot handle large strains due to element distortion. Re-meshing techniques can be used with CPFEM to increase the model accuracy, however, re-meshing is a computationally expensive process and cannot be used in the crystal plasticity framework as each new element has to be assigned a grain number and texture. As discussed in Section 2.2.3, EFG methods allow for higher strains with high accuracy without any re-meshing. Even though LS-DYNA offers EFG solvers, crystal plasticity framework has not been implemented with EFG in LS-DYNA. Therefore crystal plasticity framework presented in Section 5.1 was implemented in LS-DYNA with Element Free Galerkin model (CPEFG).

CPEFG model was validated with CPFEM simulations before performing large scale simulations. Figure 23a shows a single element in FE whereas Figure 23b shows the mesh for a single element in EFG. Mesh in EFG is only represented by nodes. Therefore eight nodes are used to represent a cube element to compare the results between FEA and EFG simulations. Please note that further representation of EFG or FEA results in this work will be shown as a classical FE mesh (Figure 23).

Figure 23: (a) Single FE Element (b) Single EFG element showing 8 nodes

Single element results under tensile loads with crystal orientation (90, 45, 45) and (0, 0, 0) under CPEFG and CPFEM are shown in Figure 24a. Results in Figure 24a show that CPEFG predictions match the CPFEM predictions for both orientations. In addition, Figure 24a shows different stress-strain predictions under different orientations thus validating the anisotropy of the model.

It is important to validate the model on not only single element but multiple elements with other modes of deformation. Therefore multi-element CPFEM and CPEFG models were simulated under

shear as shown in Figure 24b, c. Shear stress results under CPFEM and CPEFG show no major difference thus validating the CPEFG model under different loading conditions.

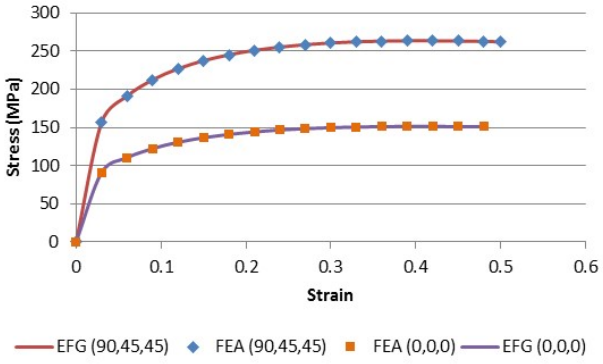

(a)

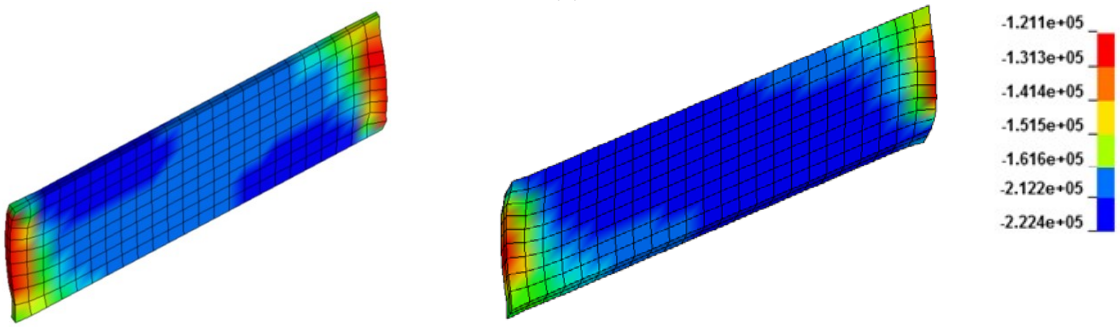

(b) (c)

Figure 24: (a) Comparison between EFG and FEA for single element under tensile loads (b) Crystal plasticity EFG simulation under shear (c) Crystal plasticity FE simulation under shear

6.1.3 Problem Formulation and Model Validation

6.1.3.1 Problem Formulation

A sample microstructure was created to accurately represent cast aluminum alloy 5754 for rolling. AA 5754 has a composition of Al-3Mg-0.3Mn-0.2Fe (by weight percent). 2D Electron Backscatter Diffraction (EBSD) data was used to create a statistically equivalent 3D voxelized microstructure and is explained in Section 2.4.2.

AA 5754 sheet being modeled was 2.5 mm in thickness. The model was created to represent half symmetry (Figure 27a) to save computational time (Figure 27a). It should be noted that the bottom of the model refers to the center of the rolled sheet. The resulting specimen was 175 x 175 x 1250 µm (Figure 27a) and had ~800 grains with an average grain size of 22 µm. CPEFG model was assumed to be from the middle of the sheet as shown in Figure 25.

Representative volume elements (RVE) are used extensively in crystal plasticity simulations [61, 169] and simulate the global material response [170, 171] by simulating the material response on a small volume. RVE's assume that the simulated material volume represents a repeating cell in the material. The generated microstructure uses (RVE) in the Z (RD) and X (TD) direction (RD-TD Plane in Figure 28) and represents the true thickness of the material in Y-direction (ND).

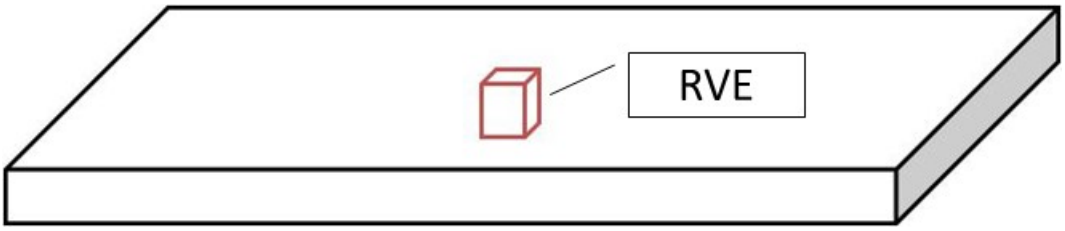

Figure 25: Location of the CPEFG model (RVE) in the real sample. RD along sheet length

Figure 26 show the initial <0 0 1> and <1 1 1> pole figures of the generated microstructure. The microstructure used in this work had similar texture to works of Jin and Lloyd [168, 142]. Table 2 shows the volume fraction of several texture components in the sheet. The generated microstructure has high volume fraction of Cube (10%) followed by S (3.9%), Brass (3.7%) and Copper (2.9%).

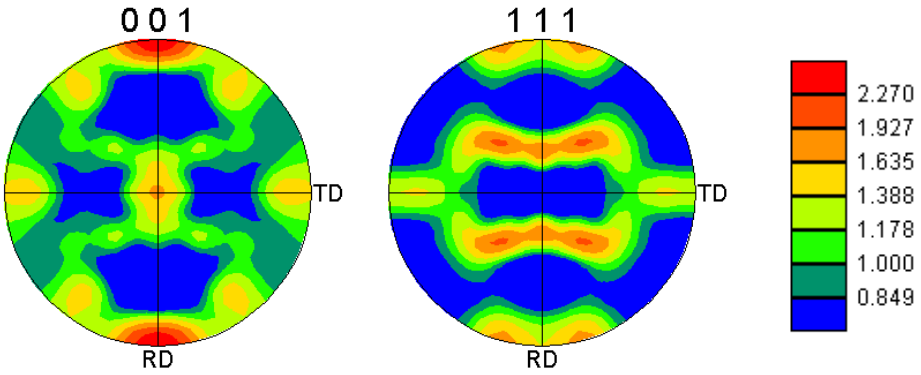

Figure 26: Initial <0 0 1> and <1 1 1> sheet texture used in the CPEFG model

Table 2: Texture components by volume fraction in the initial sample

Component	Volume Fraction (%)
Cube	10.1
Goss	0.8
Brass	3.7
Copper	2.9
S	3.9

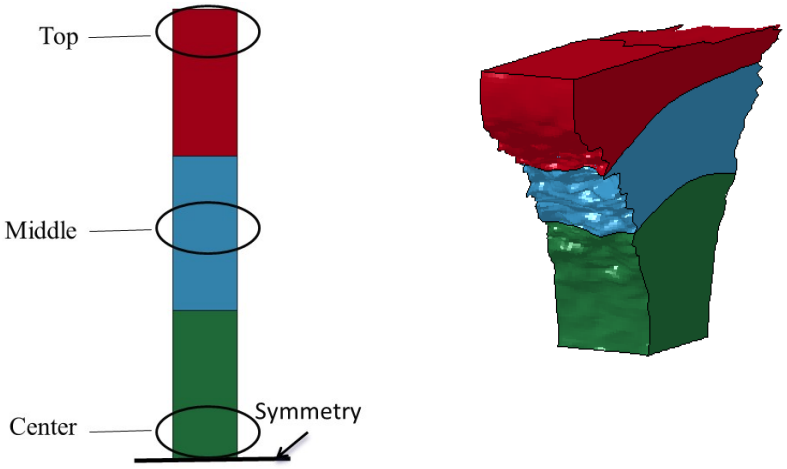

Figure 27: Simulated CPEFG models (a) Initial model and (b) Deformed model [63]

Simulations were performed to match the experimental results by Jin and Lloyd [142]. Simulated boundary conditions were based on symmetric rolling with two rollers of 161.5 mm diameter each at a constant rate of 25 rev/min for both rollers [142]. The sheet was rolled by 60% to 1 mm. The deformed model is shown in Figure 27b.

In cold rolling simulations, surface B and shaded surfaces (Figure 28) were constrained in the Y and X Direction respectively as there is very little thinning in TD during rolling. Vertical (Y-direction) and horizontal (Z-direction) velocities were applied on surface A (Figure 28) to simulate rolling. In cold rolling simulations, the horizontal velocities were varied (Equation 86) based on the number of passes, where V_S is the applied horizontal velocity, n is the number of passes and V_E is the horizontal velocity.

$$V_s = nV_E \quad \textbf{(86)}$$

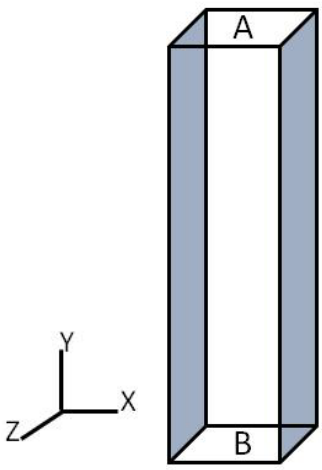

Figure 28: Boundary conditions used for simulating cold rolling

6.1.3.2 Model Validation

Top, Middle and Center sections (1875 elements - Figure 27a) in the simulated model were compared with experimental data [168, 142]. Model predictions were compared with pole figure and volume fraction data of various texture components [142]. Figure 29 shows the <0 0 1> and <1 1 1> pole figures for the top, middle and center sections after 60% deformation. The predicted texture trends in Figure 29a-c are similar to the ones reported by Jin and Lloyd [142] for all sections. Predicted textures show high S component in the top section and high Brass component in the middle and center sections. Aforementioned volume trends are also in-line with experimental results presented by Jin and Lloyd [142] which show high S and Brass in the top section and middle sections respectively.

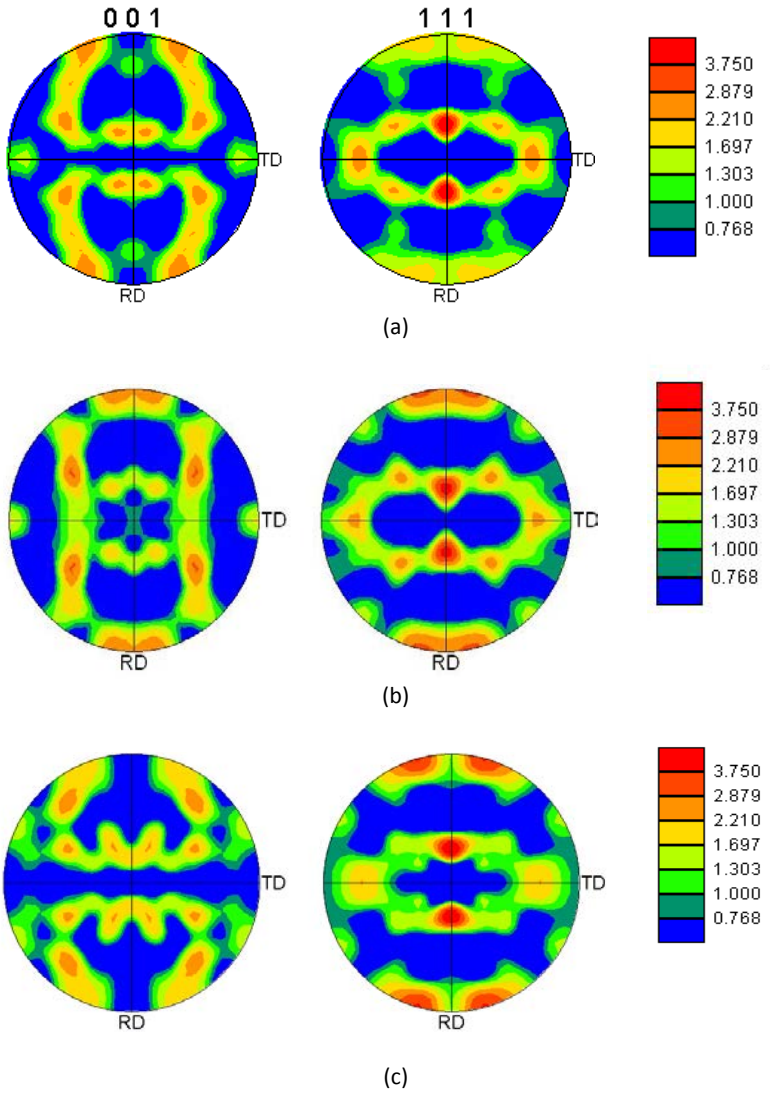

Figure 29: Predicted <0 0 1> and <1 1 1> pole figures for the (a) Top, (b) Middle and (c) Center sections at 60% thickness reduction

Volume fractions were calculated (Section 2.3.2) at the top, middle and center sections at 0 and 60% thickness reduction and are shown in Table 3. Volume fraction trends show that Cube remained relatively constant in the center section. However, the top section saw huge reduction in Cube. On the other hand, Brass and Copper saw considerable changes in the middle and center sections as seen in the experimental results [142].

Table 3: Texture components by volume fraction in the deformed sample at 0 and 60% thickness reduction in the Top, Middle (Mid) and Center (Cen) sections

Component	Top - 0%	Mid - 0%	Cen - 0%	Top - 60%	Mid - 60%	Cen - 60%
Cube	5.5	2.9	0.9	1.4	7.0	0.7
Goss	4.2	4.3	0.9	1.3	3.4	1.2
Brass	4.8	0.8	1.5	0.6	5.5	4.9
Copper	0.2	7.2	0.1	5.4	12.6	2.8
S	10.7	5.2	11.5	10.1	6.1	5.3

6.1.4 Simulation Results

6.1.4.1 Normal and Shear Strain Distribution

As discussed previously, the model was broken down into Top, Mid and Cen sections to help analyze the through thickness evolution. Normal and shear strain results shown in this section were averaged for all elements at each section and at each reduction in thickness.

Figure 30a & b show the normal and shear strains at different thickness reductions. It is observed that the top section undergoes the most normal and shear strain until 50% reduction due to its proximity to the applied velocities. However, at 60% thickness reduction, the middle section shows higher shear and normal strain than the top and center sections.

Simulated shear strain results were validated from experimental results by Roumina et al. [160]. Shear strains of 0.05%, 6% and 12% are observed at the top, middle and center sections in the simulations which are similar to the shear strain results presented by Roumina et al. [160].

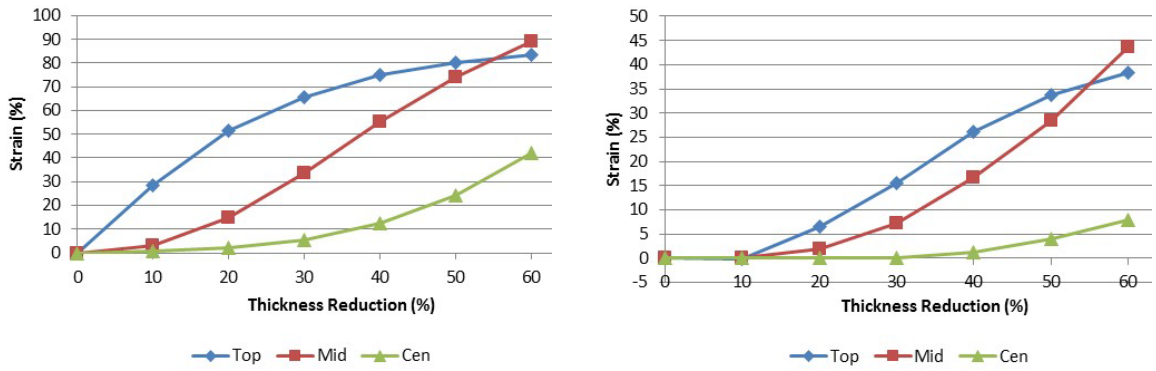

Figure 30: (a) Normal and (b) Shear strains in the rolling sample at different sections

Figure 31 shows the effective strain on different sections of the sample at 60% compression during rolling. Figure 31 shows that even though the top surface has the closest proximity to the applied velocities, the maximum strain is not experienced at that surface. Maximum strain is experienced near the top section while the least strain is experienced by the center section (0.5%). Deformed surfaces show that the center section undergoes the least curvature which is one of the reasons of negligible shear strain observed in this section.

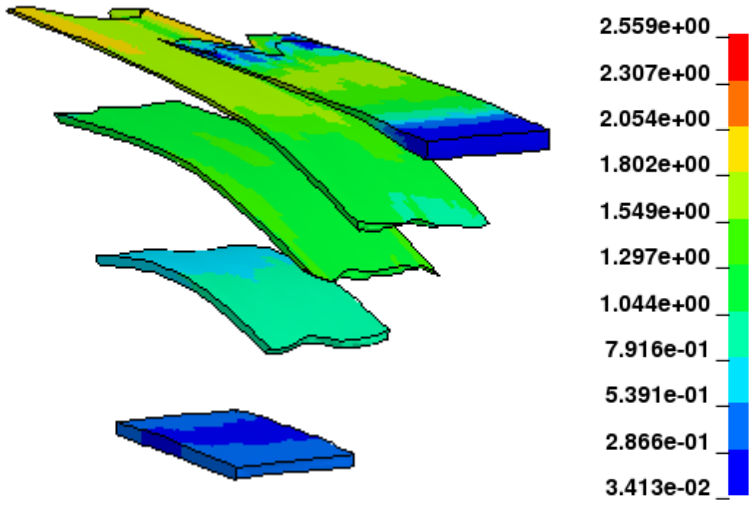

Figure 31: Effective strain on rolled sample at different sections

6.1.4.2 Through Thickness Texture Gradients

Pole figures (<0 0 1> and <1 1 1>) for the Top, Middle and Center sections are shown in Figure 29a-c and show the through thickness texture gradients at 60% thickness reduction. As top section undergoes the highest deformation, pole figures (<0 0 1> and <1 1 1>) for the top section at 0%, 30% and 60% thickness reduction are presented in Figure 32a-c. Pole figures show that the textures are similar between 30% and 60% thickness reduction with minor changes in strength in certain locations.

Initial pole figures (Figure 32a) show a higher percentage of Cube, Goss and Brass than pole figures at 30% (Figure 32b) and 60% (Figure 32c). However, pole figures at 30% and 60% thickness reduction show an increase in Copper. A better way to study the microstructure evolution was to look at the volume fraction evolution and is presented in Section 6.2.3.

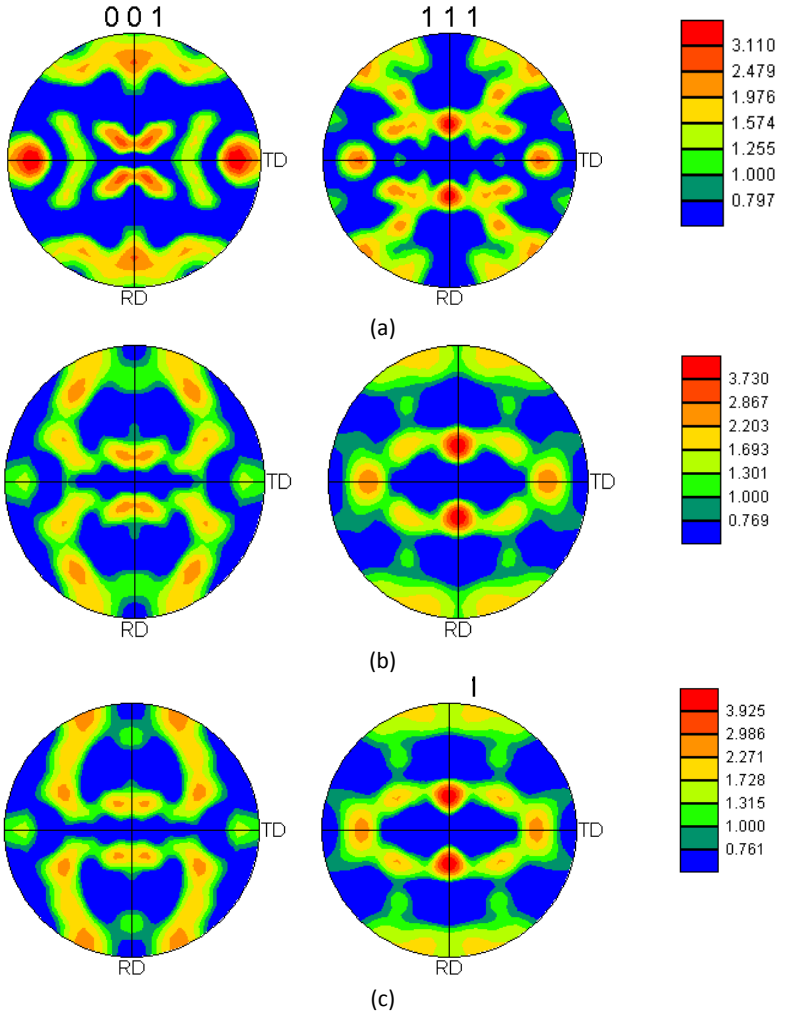

Figure 32: Top section pole figures at 0%, 30% and 60% thickness reduction

6.1.5 Grain Analysis

Experimental and simulated through thickness data shown in Section 5.1.4 highlights the need to study the through thickness microstructural behavior to understand various factors such as, grain distribution and their evolution. This information is important for engineers and researchers to study the effect of grain breakage as grain morphology affects the texture, strength and surface finish of the rolled sheet [9]. Many mechanical properties are also directly related to grain size. It is commonly known that a decrease in grain size improves the strength (Hall-Petch effect) [26] and toughness of the material [172, 173].

Large strain and severe plastic deformation (SPD) processes such as rolling [20, 168], ECAP [174, 175], etc. are used extensively for grain refinement. Several researchers have tried to predict the evolution of grain size and texture during these processes [82, 172, 174, 176]. However, their methodologies are based mainly on 2D [177] analysis and lack the ability to track evolution of microstructural changes. Third party software's are also available but are mostly used for micro-scale analysis and do not provide detailed grain analysis tools.

A new 3D path finding in-house grain analysis code (gCode) was developed to analyze the grain evolution in the rolled sheet and applied to crystal plasticity cold rolling simulations shown in Section 5.1.4. This is one of the first approaches to track the evolution of 3D microstructural changes in rolled sheets It is important to be able to track the grain size and morphology evolution during evolution as they directly affect the mechanical properties of the rolled sheet. The gCode uses the point texture data from crystal plasticity Element Free Galerkin simulations to analyze the formation of new grains, grain size and rate of subgrain formation. In addition, the gCode can be used to calculate the distribution of grain sizes, grain volume and grain misorientation in the sheet. It is noted that gCode can be used for any other application besides rolling.

6.1.5.1 gCode Algorithm

In-house gCode uses a misorientation based path finding algorithm [28] between neighboring elements to define new grains formed during deformation. As mentioned previously, synthetic microstructures generate a 3D representation of 2D experimental EBSD data. However, each element corresponding to the same grain is assigned the same orientation and hence each neighbor with exact same orientation is part of the same grain. However, as deformation is applied to the synthetic microstructure, each element experiences a different strain-path and hence undergoes different texture rotation. Therefore, after deformation, each element in a grain does not have the same

orientation and hence the misorientation between each element and its neighbors is used as a criteria to define the elements present in a grain.

Element Free Galerkin model superimposed on a finite element mesh as well as the initial and final texture are used as inputs to the gCode. Superposition on a finite element mesh was done to obtain spatial coordinates for each Element Free Galerkin point. Initial and final orientations were in Bunge Euler angles $(\varphi_1, \emptyset, \varphi_2)$. In-house gCode uses quaternions (q_0, q_1, q_2, q_3) to define the crystal orientation of each grain as defined in Section 2.3.

In-house gCode starts by finding the element neighbors and their misorientation. In 3D, one element has 6 (Figure 33a) or 26 neighbors. A simple illustration of the element neighbor criterion (in 2D) is shown in Figure 33b. Each element centroid (blue) that falls inside the circle of radius (r) is assigned as a neighbor to the element red. This is repeated until all elements have been assigned neighbors.

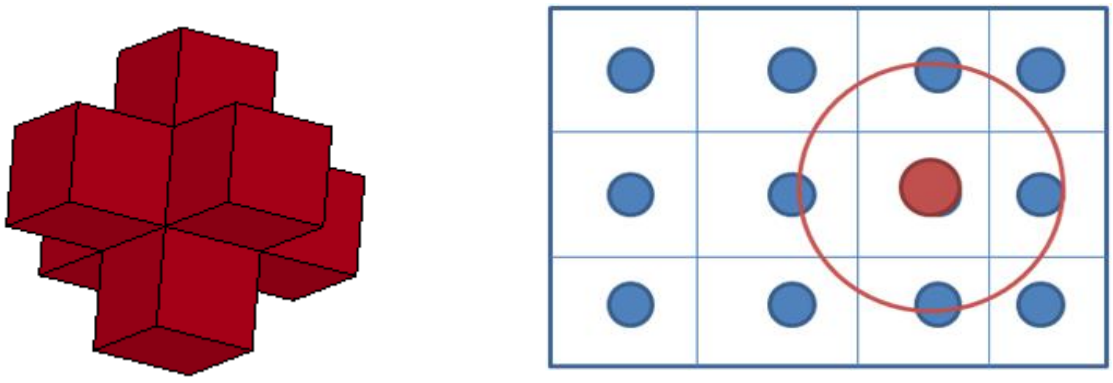

(a) (b)

Figure 33: (a) Neighbors of a single 3D element (b) Neighbor finding criterion

Element neighbor data is then used as an input to a recursive algorithm to find the grains based on misorientation angle. Figure 34a shows a simple example to explain the algorithm. Algorithm looks at the first element (red – Euler angle 1) and compares its misorientation with all the neighboring elements (green – Euler angles 1 and 2). If the misorientation angle is less than the threshold (5°, 15°) then the elements belong to the same grain [81]. If not, they are assigned a new grain till all the elements are assigned a grain number.

In the example shown in Figure 34a, all misorientations are assumed to be more than the threshold misorientation and the resulting grain assignments are shown in Figure 34b. The first grain has all the elements with angle 1 (Grain 1), the second grain has two elements with angle 2 (Grain 2), the third

grain has one element with angle 3 (Grain 3) and the fourth grain has 1 element with angle 2 (Grain 4) because it does not share any neighbors with the same angle.

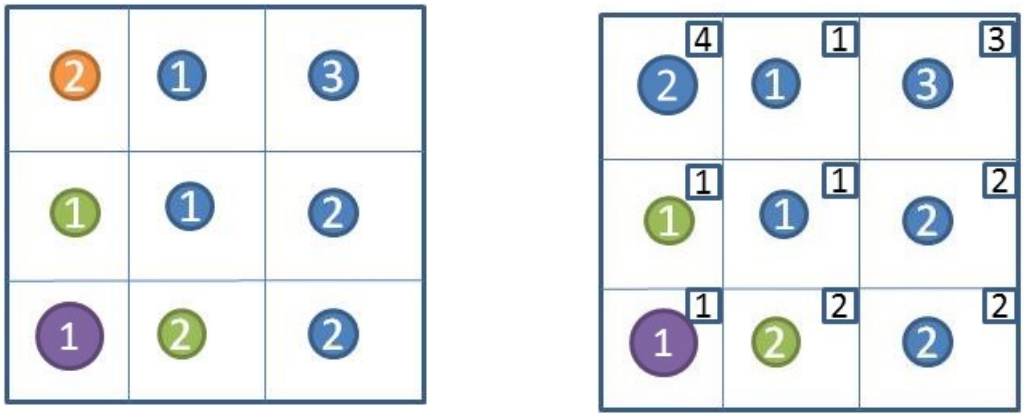

(a) (b)

Figure 34: Grain algorithm (a) Initial (b) Final. Numbers inside the circles represent the Euler angles

6.1.5.2 Validation and Evolution of New Grains in Sheet Thickness

Cold rolling results (Section 5.1.4) have successfully shown the through thickness texture variation in AA 5754 as reported by Jin and Lloyd [168]. However, it is important to validate the gCode before using it to study other grain metrics. Therefore, gCode was used to find the initial and final grain size from cold rolling simulations. Next, the simulated results were compared to experimental data [168]. Initial grain size in the simulated (Section 5.1.1) and experimental [168] microstructure was 22 µm. The final grain size was not reported by Jin and Lloyd [168] but was calculated using the optical microscopy images [168] and was found to be 15.8 µm. Similarly, final grain size from cold simulations was found to be 14.4 µm at 60% thickness reduction (using a 15° misorientation). This successful validation of the gCode allows the analysis of other grain metrics as discussed below.

Pictorial representation of the number of grains in the initial and deformed sample are shown in Figure 35. Grains in the deformed sample are shown with a 15° misorientation angle [81], and are mapped on the undeformed model for ease of comparison. Figure 35b shows that more grains are formed near the top surface (as shown by the marked regions) than the center of the sheet.

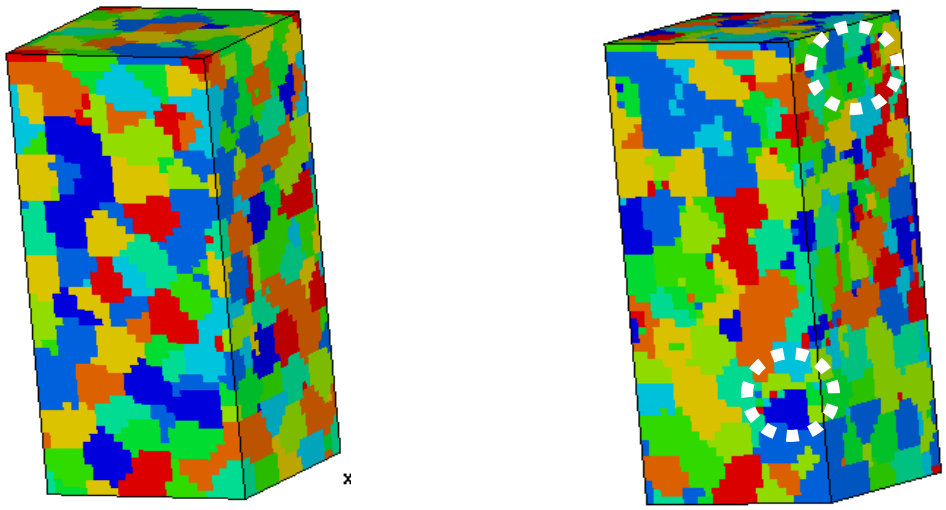

(a) (b)

Figure 35: Grains at (a) 0% thickness reduction and (b) 60% thickness reduction with random colors

Definition of a new grains (subgrains) formed due to grain breakage is based on a 10°-15° misorientation angle [81, 178]. However, as deformation proceeds, some grains with lower misorientation (~5°) are also formed. These are known as intra-granular grains and provide the driving force for grain breakage. In addition, these grains also provide the possible nuclei sites during subsequent annealing processes. Figure 36 shows the number of grains and corresponding grain size evolution. Results show similar trends for number of grains and grain size. It is observed that the subgrain formation is directly proportional to the thickness reduction while the grain size is inversely proportional. In Figure 36, the starting undeformed microstructure, had around 800 grains with an average grain size of 22 µm. Using a 5° and 15° misorientation, the final microstructure resulted in 8326 grains (radius - 10.0 µm) and 3227 grains (14.4 µm) respectively. It is noted that results presented in Figure 36 show an increasing rate for subgrain formation and require more investigation.

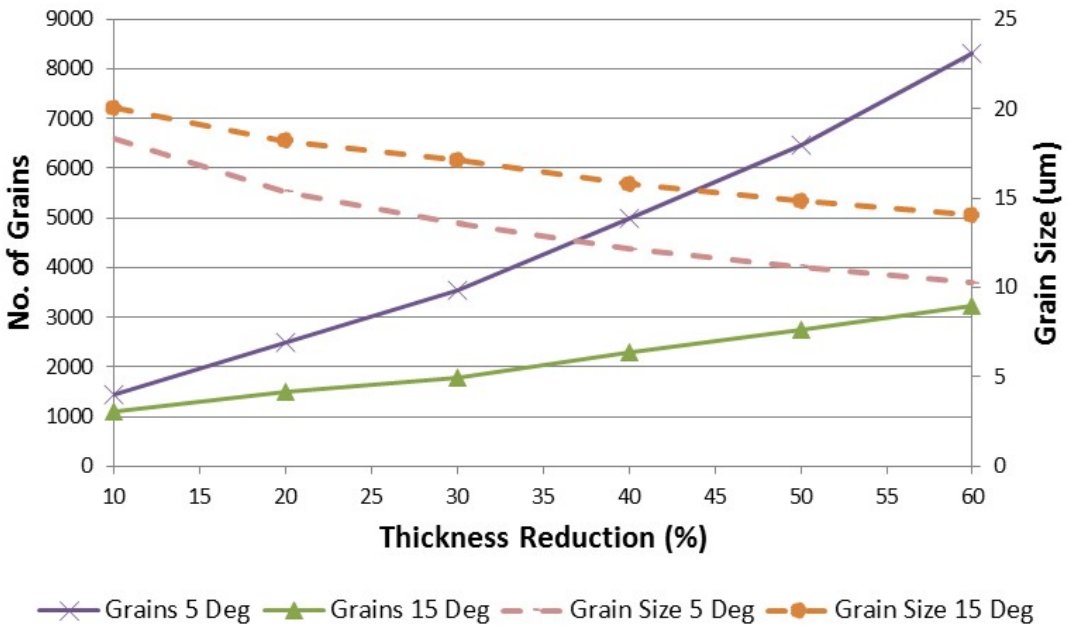

Figure 36: Number of grains and grain size in the rolled sample using different misorientation angles

Formation of subgrains gives insight into the microscopic deformation during the rolling process. It is important to study if the formation of subgrains is a continuous or abnormal process. Like abnormal grain growth [97], an abnormal subgrain formation would infer an energy threshold required to start the process. On the other hand, a continuous process would infer a continuous flow of energy to continue subgrain formation throughout the deformation.

Figure 37 shows the rate of change of grains with respect to thickness reduction$\left(\frac{dN_g}{d\varepsilon}\right)$. Results show a relatively constant rate of grain breakage for 15° misorientation which suggests a continuous formation of subgrains. However, the rate of intra-granular subgrain formation increases (5° misorientation) with deformation. This implies a higher rate of intra-granular subgrain formation and is important since these subgrains result in new grains and can be a source of nuclei during subsequent annealing.

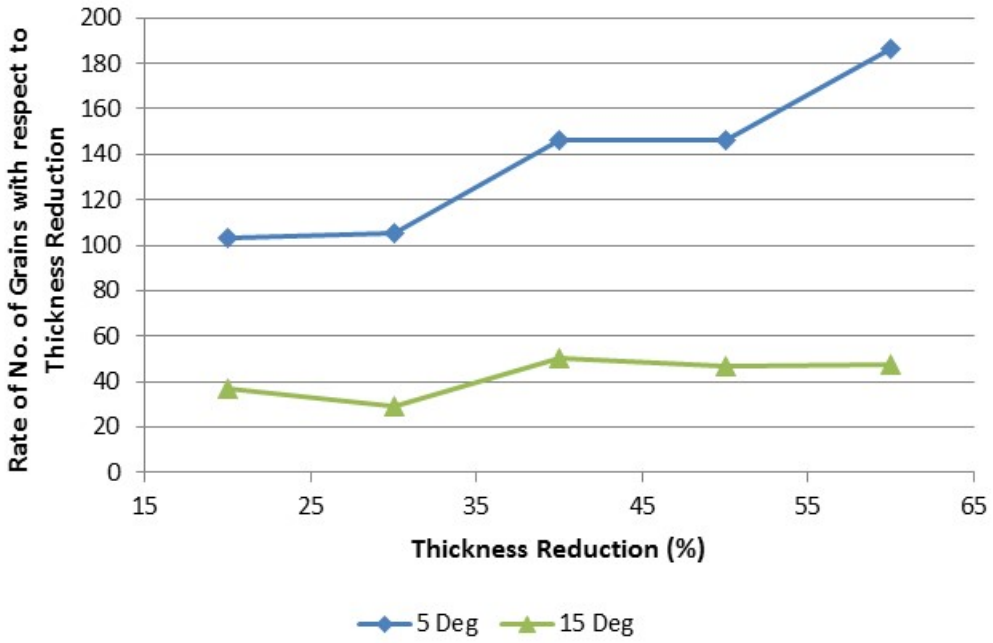

Figure 37: Rate of change of grains with respect to thickness reduction at different misorientations

As through thickness texture varies in the sheet, it is important to study the distribution of grains in the rolled sheet. To do this, grain distribution across the thickness of the sheet was calculated. Grain centroids were found by averaging the elemental centroids corresponding to that grain and the corresponding distribution was plotted across the sheet thickness. The results were normalized to compare the distribution of grains in the initial and final sample. Figure 38 shows the distribution of grain centroids in the initial (793 grains) and final (3225 grains) sample.

Initial sample (Figure 38) shows a relatively constant distribution of grains across the sheet thickness. A near horizontal trend line drawn across the results shows very little variability across the sheet. This was expected as the generated microstructure did not have a gradient in the grain size. However, at 60% thickness reduction, more grains are observed at each corresponding sheet thickness. A trend line drawn across the results shows that the number of grains decreases down the sheet thickness (from top to center of the sheet). Conversely, the grain size increases down the sheet from 11 µm to 18 µm. This difference between the top and center of the sheet is due to the strain distribution across the sheet thickness. It is important to note that the average change in grain size from the initial to 60% thickness reduction was 8 µm. However, the change in the grain size from the top to the center of the sheet was found to be 7 µm. This highlights the importance of modelling through thickness differences across the sheet.

Sheet thickness was broken down into top, top-middle and center sections and the number of grains as a percentage of the total grains were calculated, for each section, in the initial and final sample. For example change in top section = (# of grains in section)$_t$/(# of grain in entire sample)$_t$. Analysis shows that the number of grains in the center of the sheet decrease from 35% to 25% and the number of grains in the top section increase from 28% to 40%. However, results for the top-middle section show no change.

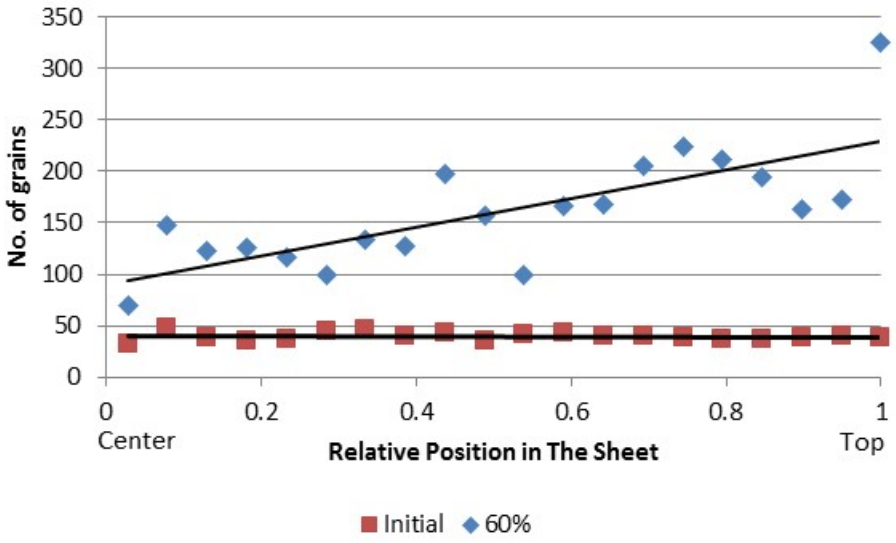

Figure 38: Grain distribution across the sheet thickness in the pre-rolled (red) and rolled (blue) sample. Trend lines are added for ease of comparison

6.1.5.3 Microstructure Analysis of Different Grain Sizes at In the Sheet

Analysis presented in the previous section shows that all grains seem to breakup into sub grains. However, it is important to find if there are any preferred orientations for subgrain formation under rolling. This would reveal if certain orientations result in stable grains i.e. they don't breakup into smaller grains or vice versa.

Deformed model was broken down into small and large grains where small and large grains account for all the grains that fall into the bottom and top 25% of the maximum grain size. Figure 39a shows that small grains have no preferred orientation, and consist of a mixture of Cube, rotated Cube, Copper and S. However, large grains (Figure 39b) show preferred orientations of S1 (56.79, 29.21, 63.43), S3 (58.98, 36.70, 63.43) and Copper (90, 27.37, 45).

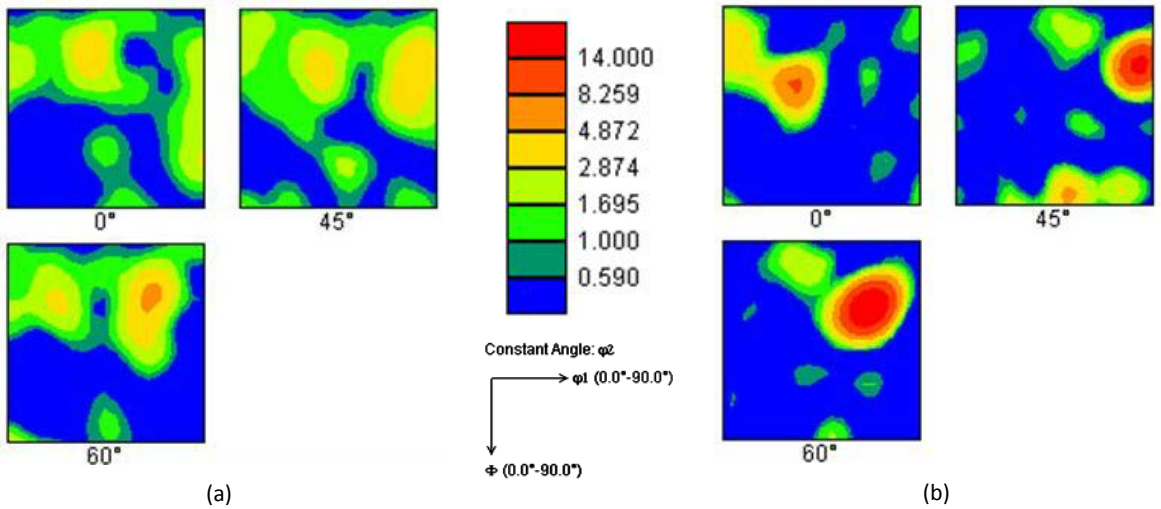

Figure 39: ODF plots for (a) small and (b) large grains at 60% thickness reduction

Next, the initial (undeformed) ODF for small and large grains is studied (Figure 40). It should be noted that only the ODF for the top and bottom 25% of the grains was used in this analysis. As the initial model is statistically equivalent, small and large grains have similar initial textures. Comparing with the initial texture, percentage of Cube is lower in the deformed sample (Figure 39) as it has rotated to other components. This is reflected in the decrease in intensity from ~14 in Figure 40 (Marked by C) to ~2 and ~4 for small and large grains respectively in Figure 39. It is possible that large grains have rotated from the initial texture to S and Copper as their intensities increase in the deformed sample in Figure 39. It is important to note that large grains could signify stable textures as they do not rotate to form subgrains.

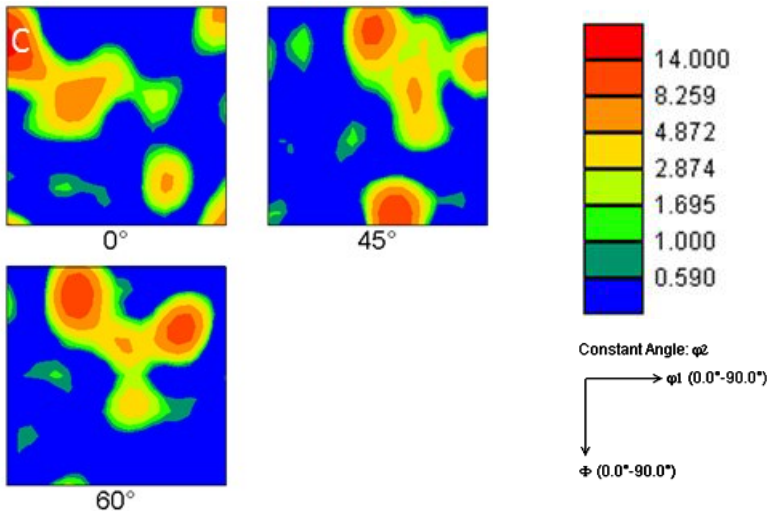

Figure 40: Combined undeformed ODF plot for small and large grains

Previous analysis has looked into small and large grains in the rolled sample as a whole. However, it is known that rolled sheet exhibit different textures across the sheet thickness [21, 164] due to the different strain paths experience across the sheet thickness. Therefore it is important to look at the small and large grains at various locations in the sheet to analyze the effect of strain distribution across the sheet.

Figure 41 shows the undeformed ODF for the top and center sections of the sheet. The top and center section refers to all the elements in the top and bottom 1/3rd of the simulated sheet. Comparing the undeformed ODFs for large and small grains (Figure 40) to Figure 41, it can be seen that the small and large grains prefer certain orientations. Whereas, the top and center section ODFs (Figure 41) don't seem to prefer any specific texture component. This is due to the presence of other texture components in the top and center ODF's that represent grains of all sizes. The best way to establish this is to explicitly draw deformed ODF's for large and small grains in the top and center sections.

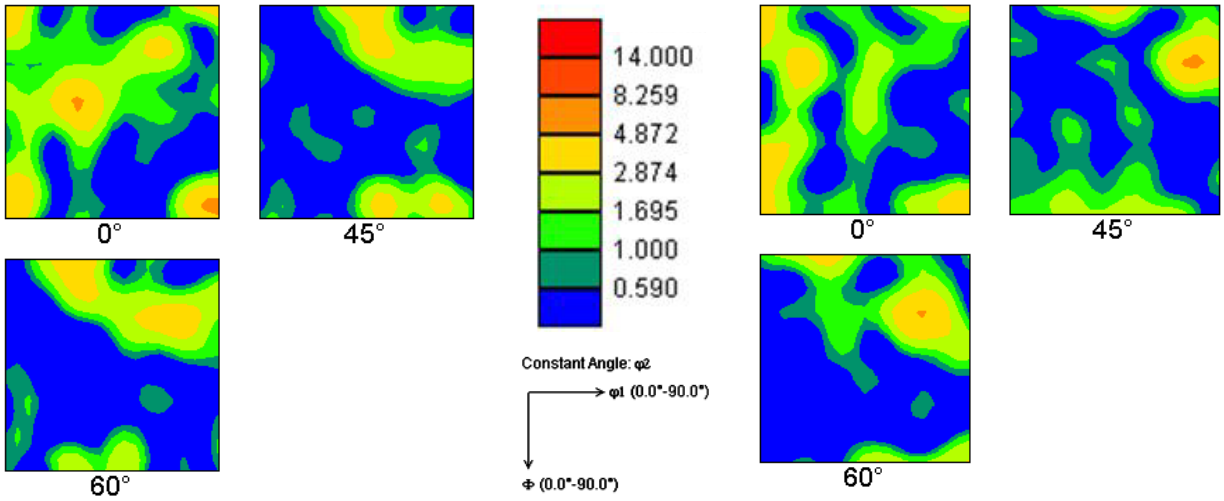

Figure 41:ODF plots for (a) top section (b) center section at 0% thickness reduction

Figure 42 shows the ODFs for small and large grains in the top and center section at 60% thickness reduction. It is observed (Figure 42a, b) that the grains in the top section do not show any clear preference. However, small and large grains show clear preference in the center of the sheet. Small grains in the center section show higher intensities of Brass, S and Copper (Figure 42c). While large grains (Figure 42d) show higher intensities for Cube, S and Copper.

In general, large grains in the top section show wider spread of texture components and hence don't show preference to any specific texture component. It has been established (Section 5.1.4.1) that the center section experiences mainly plane strain compression whereas the top section experiences a combination of shear and compression. This difference in strain paths is thought to be the main reason for these differences.

Stable/preferred orientations are assumed to not be affected by deformation [27]. However, as mentioned before, large grains represent stable orientations but don't show any preferred texture in the top section. On the other hand, small grains represented unstable orientations but show preference to specific texture components in the center section.

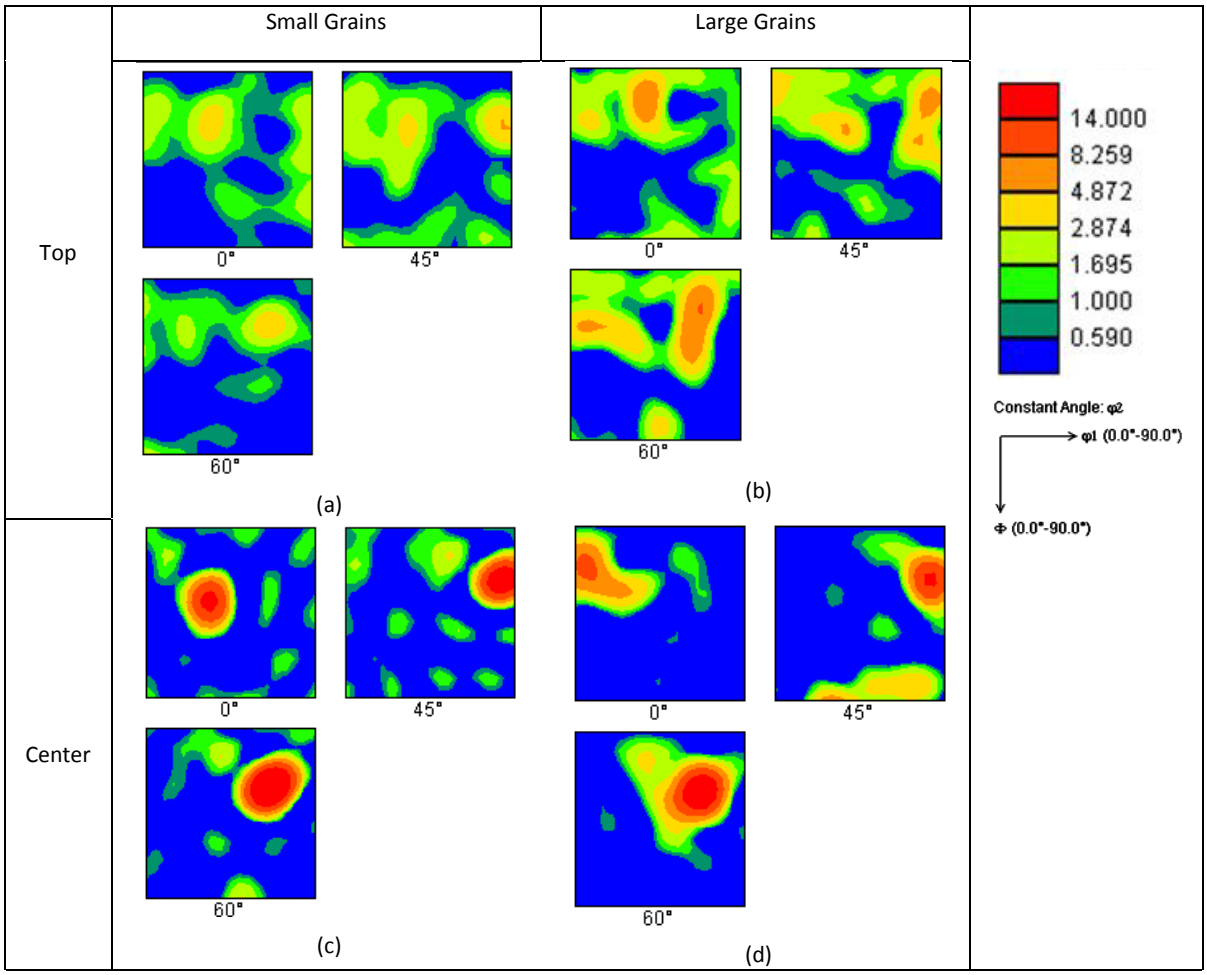

Figure 42:ODF plots at 60% thickness reduction for (a) small grains in the top section (b) small grains in the center section (c) large grains in the top section (d) large grains in the center section

6.1.5.4 Volume Fraction of Several Texture Components

Evolution of volume fraction for several texture components is shown in Figure 43. At 0%, Cube starts at 10% but reduces to 5% at 60% thickness reduction. On the other hand, Copper increases from 3% to 10%. Brass, S and Goss (5%, 5% and 1%) remain relatively consistent throughout the rolling process.

The change in Cube and Copper is due to rotation of these texture components into other components as seen in the ODF plots for small and large grains (Figure 39). In addition, Copper was found to be a stable orientation for large grains which suggests that while large grains retain their texture, small grains rotate into Copper thus increasing its volume fraction throughout the process. Brass, S and Goss are observed to be relatively consistent throughout the deformation in the whole sample. However, previous results show Brass and S to be the preferred orientations for large grains which suggests that smaller grains rotate away from S to other orientations which results in the consistent trend for these components.

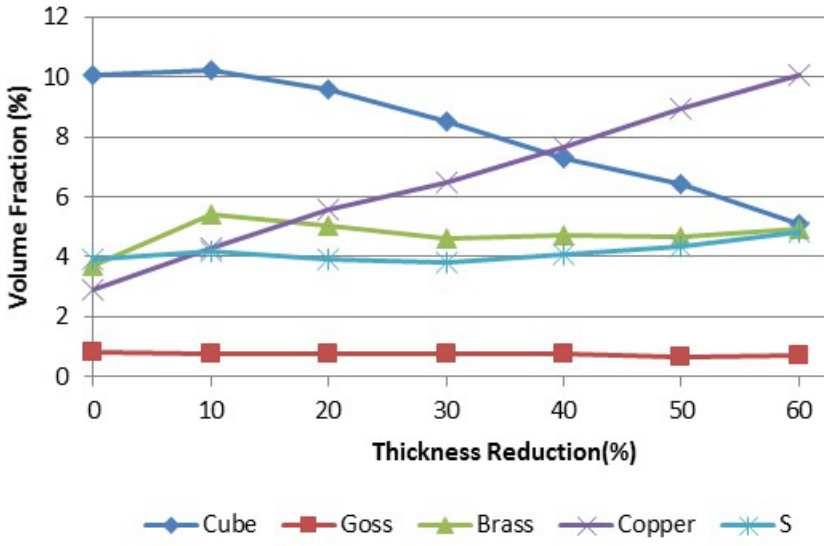

Figure 43: Volume fraction data in the rolling sample at different thickness reductions

6.1.5.5 Evolution of Grain Volume and Misorientation

Figure 44 shows the normalized grain volume evolution at initial, 20%, 40% and 60% thickness reduction. As deformation increases, more grains break into subgrains thus increasing the amount of small grains seen in Figure 44 between 0 and 0.25 grain volume. The trend switches after 0.25 grain volume as these grains breakup to form smaller grains and hence decrease with deformation.

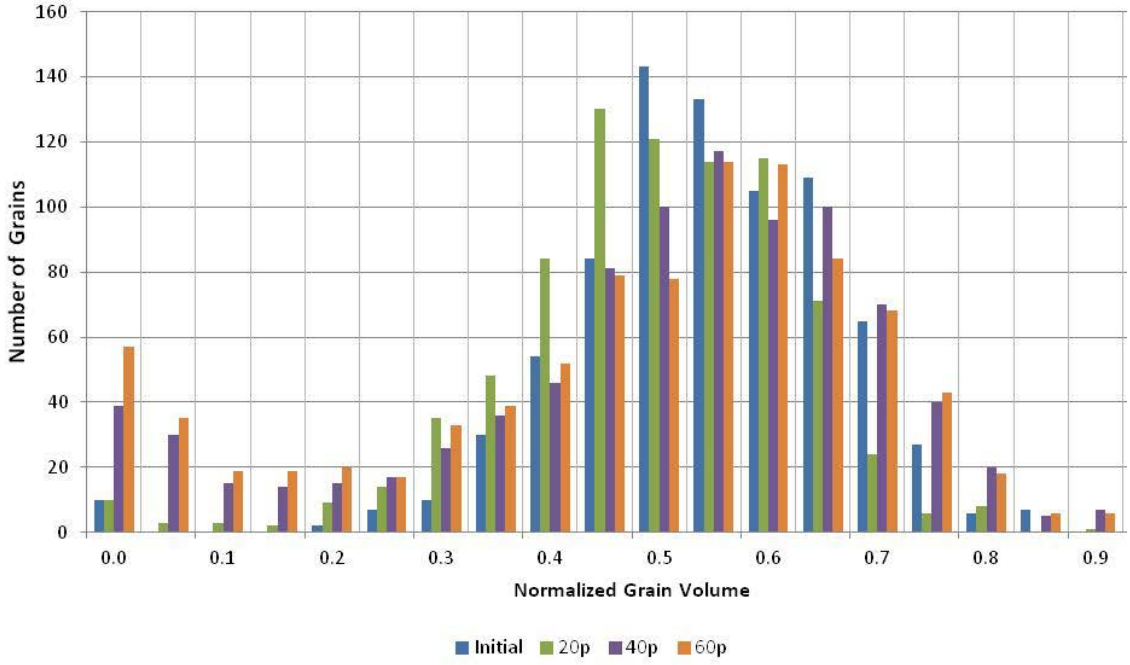

Figure 44: Normalized grain volume evolution in the rolling sample

Figure 45 shows the element neighbor misorientation distribution evolution. Misorientations less than 15° are ignored as they are considered part of the same grain. Trends from 15° to 25°, show an increase in elements with increase in deformation which suggests an increase in subgrain formation. Similar trends are observed between 52° and 59° which could be due to larger grains breaking down further to form smaller grains.

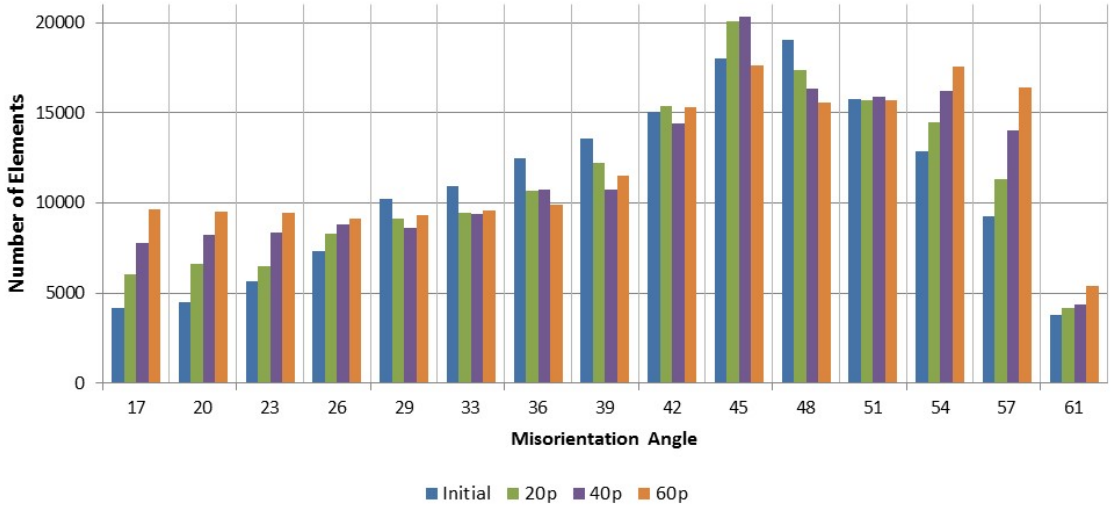

Figure 45: Misorientation distribution of element neighbors in the rolled sample at 0%, 20%, 40% and 60% thickness reductions

6.1.6 Summary and Conclusions

In this section, a rate-dependent crystal plasticity EFG model was used to simulate cold rolling across the through thickness of the sheet using a complete microstructure. Simulation results at different through thickness sections were verified using experimental results found in literature. It is found that, as expected, the normal and shear strains and texture vary in the material across the thickness of the sheet with the top surface seeing the most deformation.

A new grain analysis (gCode) framework was developed and applied on cold rolling of AA 5754 sheet. In-house gCode analyzes the formation of subgrains and other grain metrics. Final grain size from the new framework was validated against experimental work by Jin and Lloyd [168] and then used to study several grain metrics.

Analysis shows that the amount of subgrains are proportional to the thickness reduction and inversely proportional to grain size. Study of rate of subgrain formation shows that subgrains are formed at a constant rate and are directly proportional to the applied deformation. This is also evident from the normalized grain volume distribution and evolution of misorientation with nearest neighbors. Intra-

granular misorientations also increase with deformation. These could contribute to the formation of new grains during subsequent annealing. Grain sizes were calculated across the sheet thickness to analyze the effect of strain distribution across the sheet thickness. It was concluded that the formation of subgrains decreases towards the center of the sheet. Comparing the grain sizes, it was concluded that the grain size changes by around 7 μm from the top to the center of the deformed sheet and by around 8 μm, between the average initial and final grain size. The similarity in the predicted grain sizes before and after rolling and between the top and center rolled sections highlights the importance of capturing the microstructure differences across the through thickness of the sheet.

Grain breakup for the small and large grains were also studied. It is concluded that orientations that correspond to small grains are unstable while, orientations that correspond to large grains are stable. Results indicate that large grains have a preferred orientation close to S and Copper. This preferred orientation is also dependent on the strain path experienced by the grain. Results for small and large grains for the top and center sections show that small grains in the center sections prefer Brass, S and Copper. Whereas, large grains in the center of the sheet experience mostly compressive stress and the corresponding grains preferred Cube, S and Copper.

6.2 Comparing the Through-thickness Response under Rolling and Plane Strain Compression

Most approaches in literature assume a plane strain compression condition to simulate rolling [163, 179, 180, 18, 181]. However, this assumption only holds true under symmetric rolling as layers close to the center line of the sheet experience plane strain compression [180, 182]. Knezevic et al. [18] have simulated cold rolling under this assumption but as a consequence, have neglected the different strain paths experienced across the sheet thickness while Engler et al. [183] have modelled different layers of sheet thickness as separate simulations but are unable to capture the microstructure changes. Therefore it is important to capture the microstructural changes in the sheet thickness with the correct boundary conditions to simulate rolling.

To identify the differences between plane strain compression and rolling, simulations for plane strain compression were performed and compared with cold rolling simulations (Section 5.1.1) using the same initial microstructure and thickness reduction. Several key factors namely; equivalent strains, textures, volume fraction evolution and β and γ fibers were compared and are discussed below.

6.2.1 Normal and Shear Strains

Figure 46a & b show the normal and shear strain in the top section during rolling and plane strain compression respectively. Normal strains on the top section during rolling and plane strain compression (Figure 46a) follow the same trends. However, the maximum strain at 60% thickness reduction for rolling is about 50% that of plane strain compression. Figure 46b shows that the maximum shear strain experienced during plane strain compression is negligible (9%) compared to rolling (38%). The differences in normal and shear strains during plane strain compression and rolling are due to the shear effect under rolling.

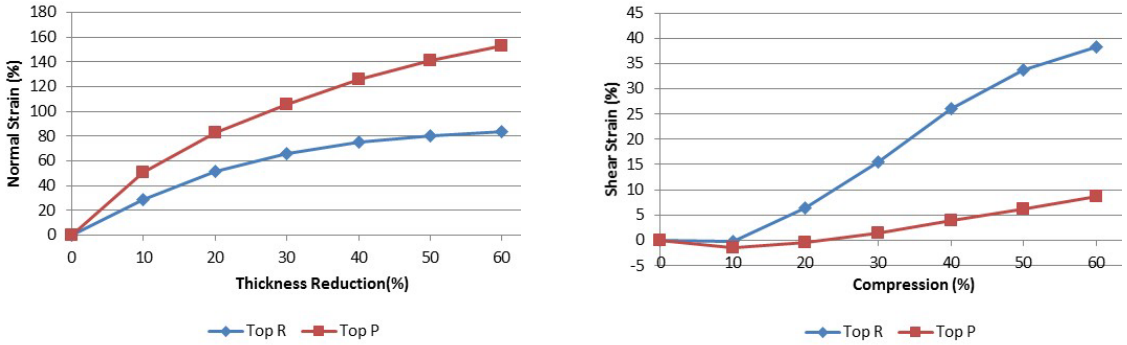

(a) (b)

Figure 46: (a) Normal strain and (b) Shear strain on top section (R stands for rolling and P stands for plane strain compression)

6.2.2 Texture

It is well known that texture plays an important part in the final material properties [97]. Therefore rolling and plane strain compression textures were compared at 60% thickness reduction. Pole figures for <1 1 1> were plotted for the top sections during rolling (Figure 47a, d & g) and plane strain compression (Figure 47b, e& h). To highlight the difference between the pole figures, difference pole figures were also calculated (Figure 47c, f & i). Each point on the difference pole figure ($Diff$) was calculated using Equation 87, where W_R and W_C are the weights of specific points in the pole figures for rolling and plane strain compression respectively.

$$Diff = abs(W_R - W_C) \quad \textbf{(87)}$$

Pole figure intensities in Figure 47 are kept same for each thickness reduction for ease of comparison. Initial difference pole figure serves as a sanity check and shows 0 intensity (Figure 47c) which confirms that the starting textures for both cases were exactly the same. Difference pole figures at 30% and 60% thickness reduction (Figure 47f & i) show high Brass (5% and 7%) and Copper (8% and 11%) but

low Cube (4% and 2%). While percentage of Brass and Copper increases with deformation, percentage of Cube goes down. These trends are summarized in Table 4.

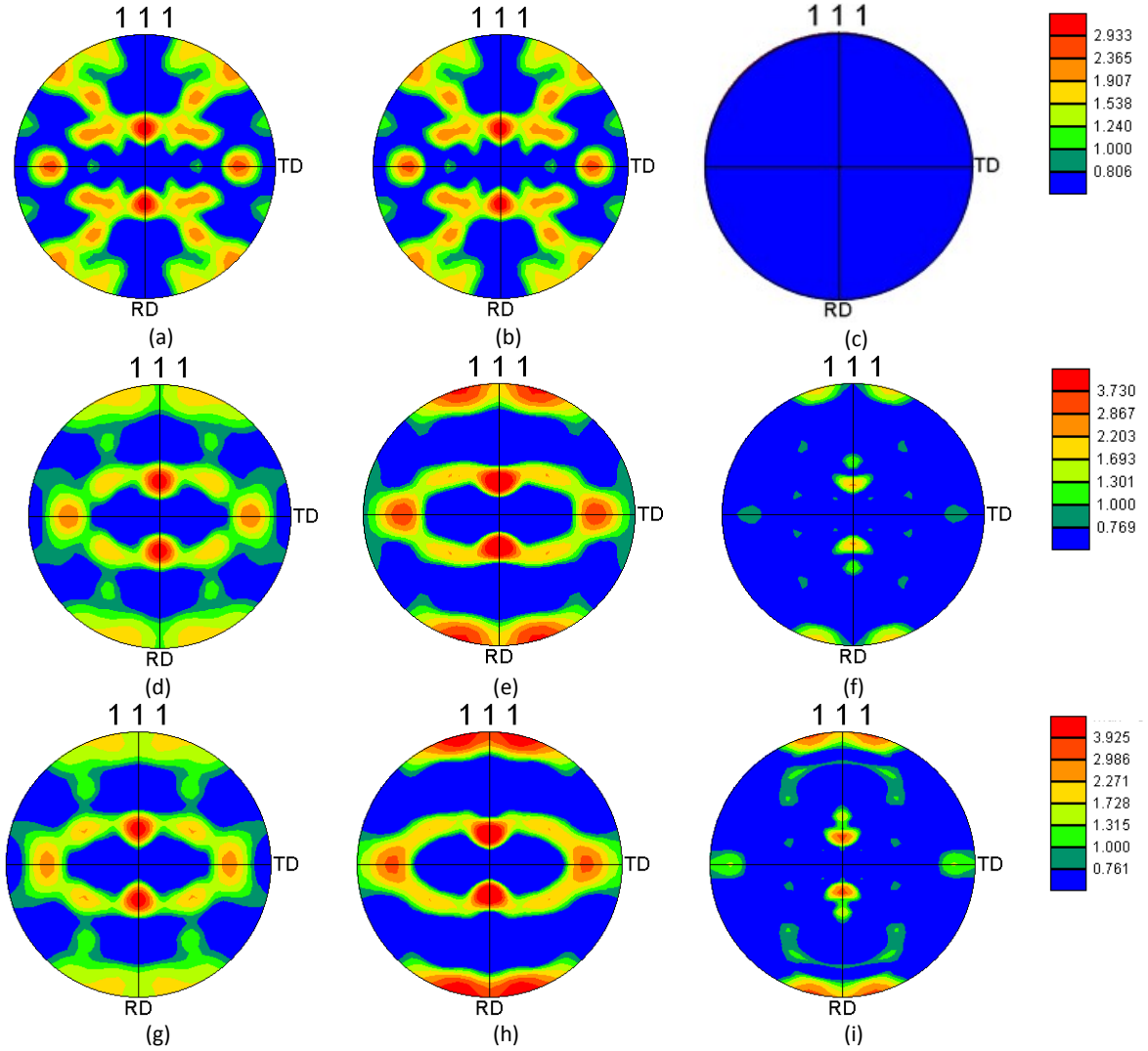

Figure 47: Rolling <1 1 1> pole figures, plane strain compression <1 1 1> pole figures and difference pole figures at the top section at (a-c) 0%, (d-f) 30% and (g-i) 60% thickness reduction respectively

Table 4: Top section volume fraction difference at 30% and 60% thickness reduction for rolling and plane strain compression

Component	Volume Fraction Difference (%) at 30%	Volume Fraction Difference (%) at 60%
Cube	3.8	2.3
Goss	0.9	1.1
Brass	4.5	7.3
Copper	7.7	10.6
S	0.6	0.7

Pole figures and difference pole figures highlight the differences between rolling and plane strain compression. These differences are due to the effect of shear found during rolling [160, 161]. However, to understand these differences further, volume fraction of various texture components need to be analyzed and are presented in the next section.

6.2.3 Volume Fraction Evolution

Volume fractions for different texture components were studied to understand the changes during deformation. To this effect, volume fractions for the top section during rolling and plane strain compression were compared. Figure 48a & b show the volume fractions for different components for the top surface under rolling and plane strain compression. Percentage of S remains relatively unchanged during both deformations with a slight dip during plane strain compression at 10% thickness reduction. Copper increases to 6% and 16% between 0% and 60% thickness reduction in rolling and plane strain compression simulations respectively. The remaining components (Cube, and Goss) decrease during rolling and plane strain compression while Brass decreases during rolling but increases during plane strain compression.

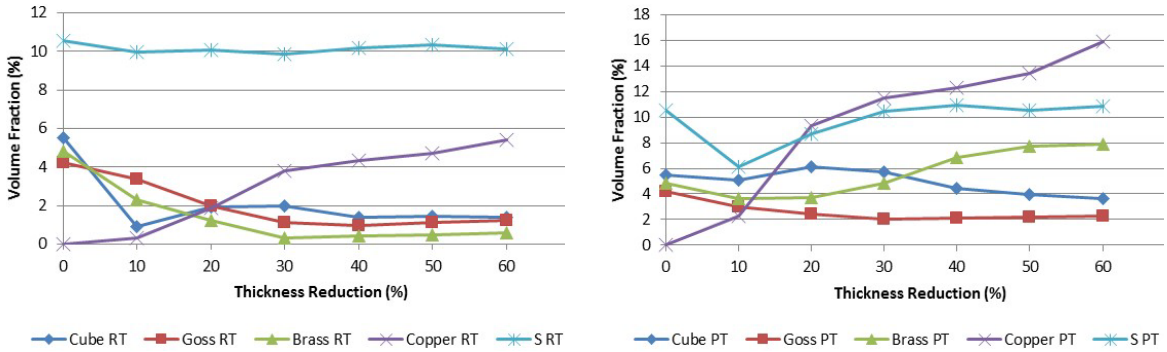

(a) (b)

Figure 48: Volume fractions of various texture components under Rolling
(R stands for rolling, P stands for plane strain compression and T stands for Top section)

To identify the differences between the top and center section, volume fraction trends for several texture components on the top and center section were calculated (Figure 49). Cube, Copper and Brass show higher volume fraction on the top section in plane strain compression than rolling while S and Goss start low but at 60% thickness reduction result in similar trends to Cube, Copper and Brass. Cube, Copper, S and Goss show higher volume fractions on the top section than the center section under both deformation modes. However, Brass shows lower volume fraction under rolling than center section.

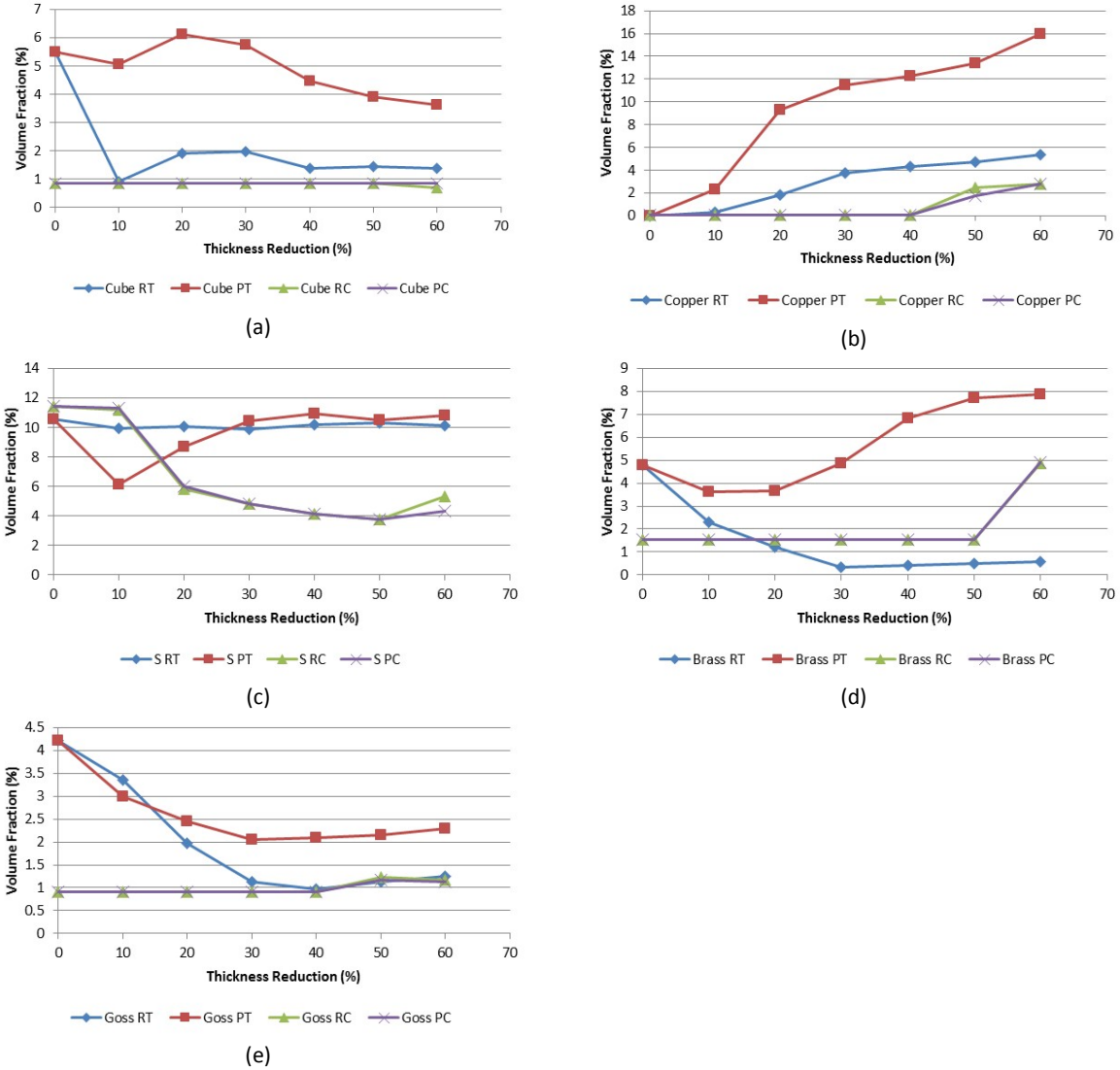

Figure 49: Volume fraction comparisons of (a) Cube, (b) Copper, (c) S, (d) Brass and (e) Goss at top and center section (R stands for rolling, P stands for plane strain compression, T and C represent the top and center sections of the sample)

Results in Figure 49 show that the volume fractions for rolling and plane strain compression at the center section are similar for all texture components. These results are in-line with the assumption that plane strain compression is similar to symmetric rolling near the sheet center [18, 184] and clearly show that the differences between rolling and plane strain compression are due to the shear effect found in rolled specimens.

6.2.4 Rolling Fibers

ODF sections of rolled FCC sheets provide a continuous tube of orientations that run from {1 1 0} <1 1 2> through {1 2 3} <6 3 4> to {1 1 2} <1 1 1>. This is further broken down into subsections and are known as the, α and β fibers [19, 185, 186] as shown in Figure 50. β-fiber is found between Copper and Brass through S. γ-fiber also shows up in FCC metals with high stacking fault energy and runs in elements parallel to the {1 1 1} planes from {1 1 1} <1 1 2> to {1 1 1} <1 10> [19, 185, 186].

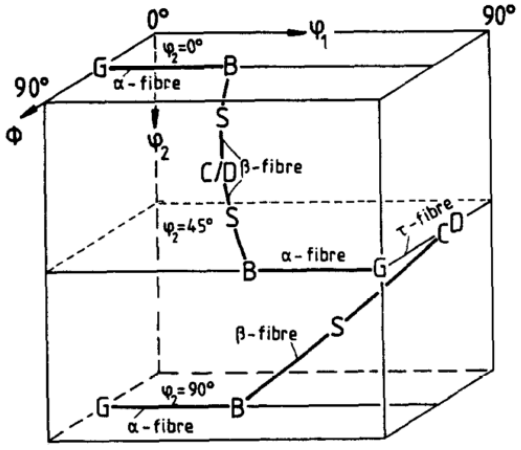

Figure 50: Plots of α and β fibers in Euler space [19]

Formation of γ-fiber is considered very important in enhancing the formability of aluminum sheets [142]. γ-fiber is caused by the shear strain due to the friction between the rollers and the sheets [187, 188]. Figure 51a & b shows the ODF intensity distribution of γ-fiber and β-fiber on the top section at 30% and 60% thickness reduction under rolling and plane strain compression. Distribution shows that rolling produces higher intensities of γ-fiber across the range of φ_1 and the fiber strengthens as thickness reduction increases. Conversely, β-fiber (Figure 51b) shows higher intensities in plane strain compression simulations. As expected, rolling simulations indicate higher formability as average intensities at 60% thickness reduction for rolling (0.73) are higher (0.45) than plane strain compression.

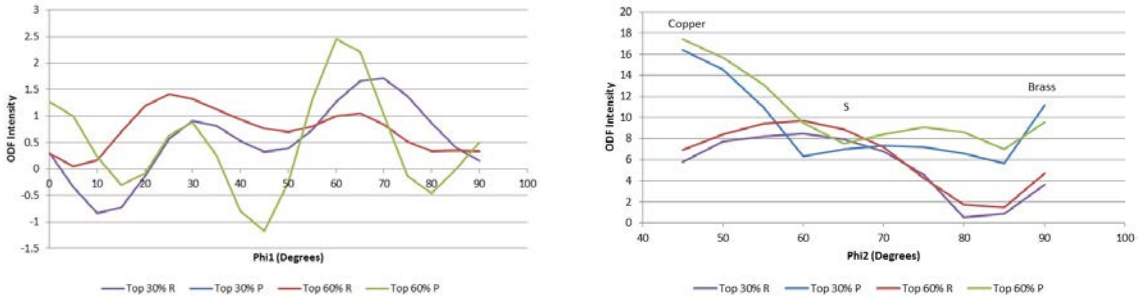

(a) (b)

Figure 51: ODF intensity comparisons of (a) γ-fiber and (b) at β-fiber top section between rolling and plane strain compression (R stands for rolling and P stands for plane strain compression)

6.2.5 Summary and Conclusions

The rolling process is often approximated by plane strain compression. To highlight the differences, between rolling and plane strain compression, results from rolling simulations presented in Section 5.1 were compared with plane strain compression simulations. Normal strains, shear strains, texture, volume fraction and β and γ fibers show clear differences between the two processes. Therefore, it is concluded that there are major differences between the two processes. However, volume fraction data from the top and center section show that the two processes result in similar texture evolution near the sheet center. As expected, rolling results in stronger γ-fiber which is necessary to increase formability.

The work presented in this section shows that rolling and plane strain compression lead to different microstructures and will not have similar behavior under subsequent forming operations. Therefore, it is necessary to model the complete microstructure and boundary conditions for successful rolling simulations.

6.3 Hot Compression

Similar to other large strain processes, hot compression also involves inducing huge plastic strains in the material resulting in huge changes in texture and stress-strain response of the material. Tensile and shear results presented in literature show little effect on the material stress-strain response at lower temperatures for AA 5xxx alloys [189, 190]. However at higher temperatures, AA 5xxx alloys have been shown to be temperature and strain-rate sensitive [191]. Hashemi et al. [192] have also shown the temperature and strain-rate dependence of AA 6xxx alloys from 323 K to 573 K and from 0.001 s^{-1} to 1 s^{-1} under uniaxial tension. Unlike some AA 5xxx alloys, AA 6xxx are positive strain-rate sensitive i.e. they get softer at higher temperatures and lower strain-rates [193]. Therefore, for modelling high temperature applications (e.g. extrusion, ECAE, etc.) it is important to correctly predict the stress-strain and texture response.

Phenomenological models have been shown to predict material response under various temperatures and strain-rates [194] however they are unable to capture the texture evolution. Crystal plasticity works by Staroselsky et al. [195] and Cyr et al. [196] have studied the effects of temperature under low strain-rates (creep) and shear for Ni super alloys and AA 5754 respectively. Dislocation based crystal plasticity simulations [197] have also shown to predict the temperature effects in materials. Effects of strain-rate and temperature have been studied in literature. Hansen et al. [198] have implemented a temperature dependent high strain-rate single crystal model for Copper.

In this work, a Taylor-type polycrystal in-house model (Section 4.1) was used to simulate hot compression for AA 6063 at various strain-rates (0.01 s^{-1}, 0.1 s^{-1}, 1 s^{-1} and 10 s^{-1}) and temperatures (400^{0}C, 450^{0}C, 500^{0}C, 550^{0}C and 600^{0}C). As extrusion processes are carried out in this temperature range, hot compression experiments were also carried out at these temperatures. Hot compression simulations were used to predict the texture and stress-strain response of the material during deformation. Experimental observations in literature suggest that AA 6063 undergoes static recrystallization after hot deformation [24]. Therefore, a probabilistic integration point based static recrystallization model (Section 4.2) was used to predict the final texture and grain size observed under experimental conditions.

6.3.1 Modified Hardening Model

Single crystal slip hardening model (Equation 61) presented in Section 4.1 cannot account for different temperatures and strain-rates. Therefore the current hardening model was modified [199, 200] with:

$$h_\beta = h_s + (h_0 - h_s)sech^2\left[\left(\frac{h_0 - h_s}{\tau_s - \tau_0}\right)\gamma_\alpha\right] \quad \textbf{(88)}$$

where h_0 and h_s are the initial and asymptotic hardening rates and τ_s is the saturation shear stress. To incorporate the effects of strain-rate, polynomial functions (Equation 89, 90 and 91) were used for the evolution of all hardening parameters (h_0, h_s and τ_s). A similar approach has been used by Kocks and Mecking as a Voce law based scaling function to predict material response [201].

$$h_s = a_1[log10(\dot{\varepsilon})]^2 + b_1 log10(\dot{\varepsilon}) + c_1 \quad \textbf{(89)}$$

$$h_0 = a_2[log10(\dot{\varepsilon})]^2 + b_2\ log10(\dot{\varepsilon}) + c_2 \quad \textbf{(90)}$$

$$\tau_s = a_3[log10(\dot{\varepsilon})]^2 + b_2\ log10(\dot{\varepsilon}) + c_3 \quad \textbf{(91)}$$

where a, b, c are fitting parameters and $\dot{\varepsilon}$ is the strain-rate.

To incorporate the effects of temperature, hardening parameters were also evolved based on different temperatures. Equation 92 is used for the temperature and strain-rate evolution of τ_0 and is able to account for the stress-strain response under various temperatures and strain-rates.

Works by Varshni and others [195, 202, 203] and Slagle and Lowrie [204, 205] scale the elastic constants based on different temperatures and use polynomial functions to represent the dependence of elastic constants on temperature. Therefore, elastic parameters have been scaled by τ_0 as:

$$\tau_0 = \sum_{i=0}^{3}\sum_{j=0}^{2} d_{ij}[log10(\dot{\varepsilon})]^i\,[log10(\theta)]^j \quad \textbf{(92)}$$

where d_{ij} are calibration coefficients.

6.3.2 Problem Formulation

A sample microstructure with 1000 crystals was created to accurately represent cast aluminum alloy 6063 (chemical composition for AA 6063 is shown in Table 5). 2D Electron Backscatter Diffraction (EBSD) data was used to create the sample as is explained in Section 2.4.1.4.

Table 5: AA 6063 chemical composition (wt%)

Mg	Fe	Si	Cu	Ti
0.49	0.029	0.16	0.40	0.01

Experimental pole figure from EBSD scans (Figure 52) is shown in Figure 53a while the pole figure from generated texture is shown in Figure 53b. Figure 53a & b are on the same scale and show that there is almost no difference in the generated and experimental pole figures. As ODF provide more information across different sections, ODF for the experimental and generated texture is shown in Figure 54a & b respectively. Texture shows Copper, Cube (45^0 ODF) and S (65^0 ODF).

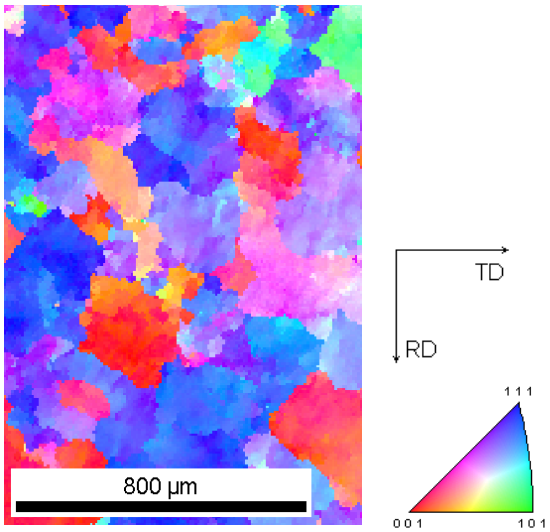

Figure 52: Experimental IPF map for AA 6063

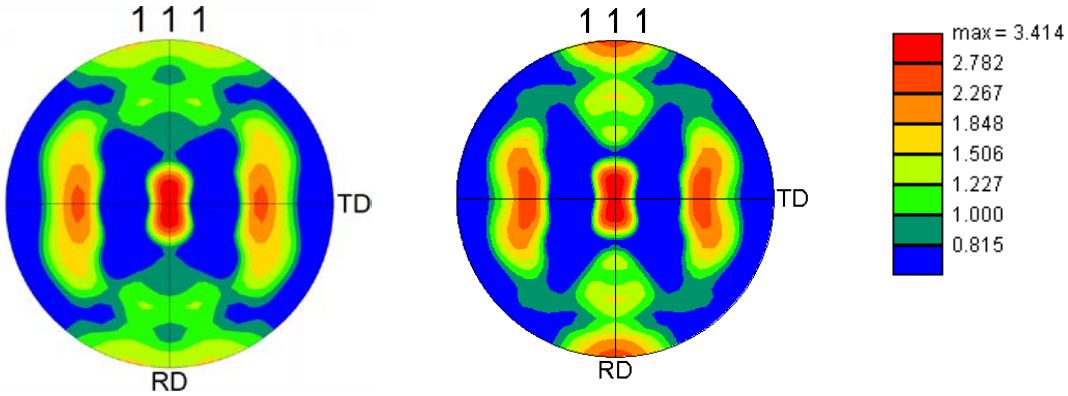

(a) (b)

Figure 53: (a) Experimental and (b) Generated <111> pole figure for AA 6063

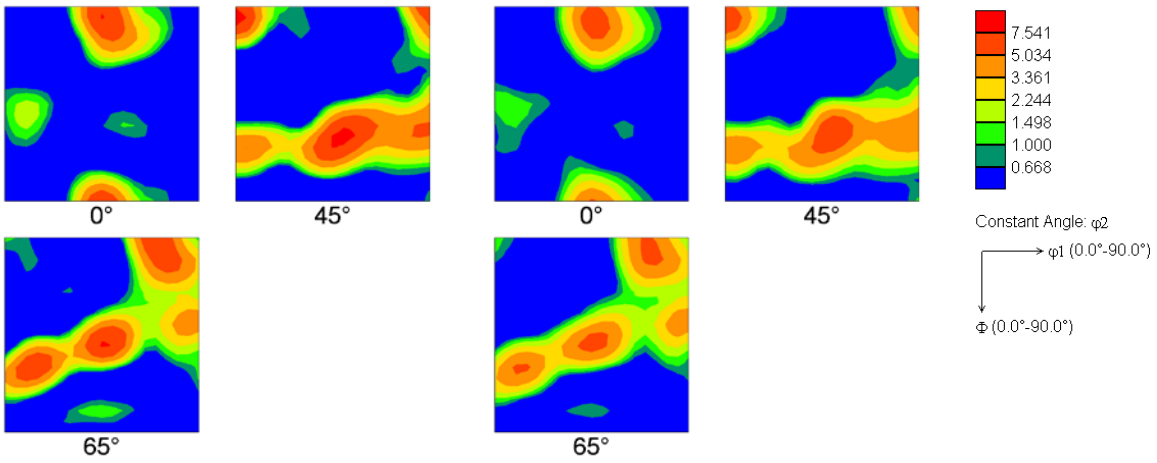

(a) (b)

Figure 54: Initial (a) Experimental and (b) Simulated AA 6063 texture shown as ODF plot (φ_2-sections)

To simulate compression, the sample microstructure was applied negative (strain-rate) $\dot{\varepsilon}$ as shown in Figure 55. There were no other boundary conditions applied in the other directions.

Figure 55: Geometry and loading conditions applied

6.3.3 Model Calibration

Experimental AA 6063 compression data was used to calibrate the hardening parameters for the crystal plasticity model. Data for all strain-rates and temperatures (except for 500 ^{0}C) was used for calibration. Figure 56 shows the data points used to fit the hardening parameters h_0, h_s and τ_s at 0.01 s^{-1}, 0.1 s^{-1}, 1 s^{-1} and 10 s^{-1} and the corresponding polynomial fits to those points. Polynomial fits were based on least squares method to find the least error. Initial elastic values were also calibrated in a similar manner. Resulting elastic values and hardening parameters are given in Table 6 and 7.

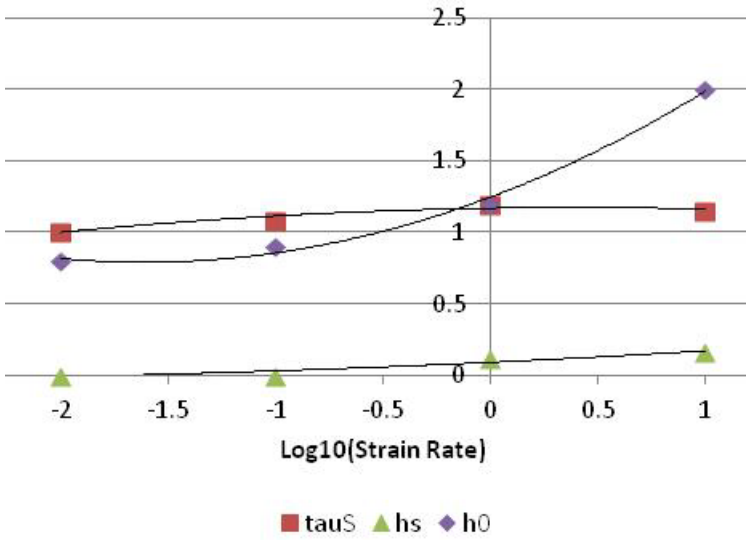

Figure 56: Calibrated AA 6063 data for h_0, h_s and τ_s

The same procedure was repeated for τ_0 but as it is dependent on both strain-rate ($\dot{\varepsilon}$) and temperature (θ), it would correspond to a surface rather than a line. The resulting best fit surface with an R-squared value of 0.9958 is shown in Figure 57 and the resulting parameters are given in Table 8. Black dots in Figure 57 correspond to experimental points.

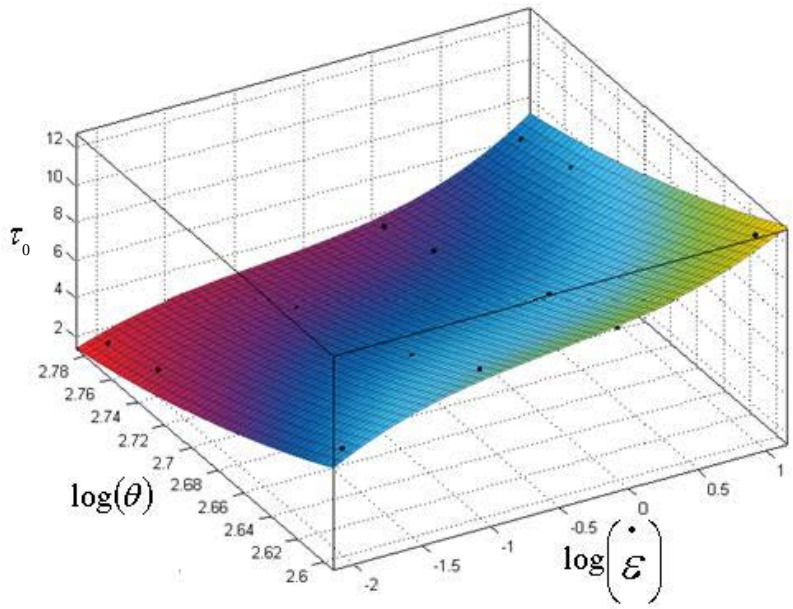

Figure 57: Calibrated surface for τ_0

Table 6: Calibrated elastic values for AA 6063

	C_{11}/τ_0	C_{12}/τ_0	C_{44}/τ_0
Value	4893.6	2808.5	1276.6

Table 7: Calibrated values for h_0, h_s and τ_s (AA 6063)

	a	b	c
1	-0.040	0.080	0.120
2	0.175	0.565	1.245
3	-0.030	0.024	1.187

Table 8: Calibrated values for τ_0 (AA 6063)

d_{ij}	**0**	**1**	**2**
0	563.2	-379.8	64.380
1	-1.662	1.013	0.042
2	-3.838	1.713	0.000
3	0.383	0.000	0.000

6.3.4 Model Verification

Calibrated model parameters were used to verify if the hardening parameters are able to predict the correct stress-strain curves at 0.01 s^{-1}, 0.1 s^{-1}, 1 s^{-1} and 10 s^{-1} strain-rates and temperatures of 400^{0}C, 450^{0}C, 550^{0}C and 600^{0}C. Simulated stress-strain results were compared to experimental stress-strain results and are shown in Figure 58-61. Simulated results show excellent agreement with experimental results at all temperatures and strain-rates. It should be noted that some of the experimental results are not shown till 60% compression due to material failure and softening seen in experimental results.

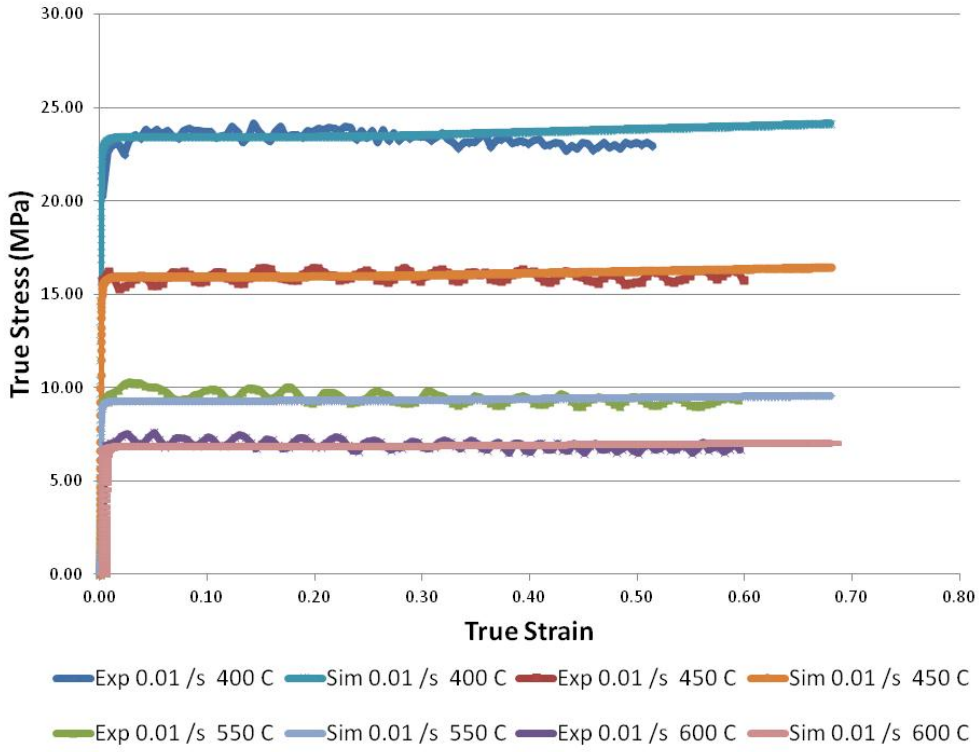

Figure 58: Experimental and simulated AA 6063 uniaxial compression stress-strain curves at 0.01 s^{-1}

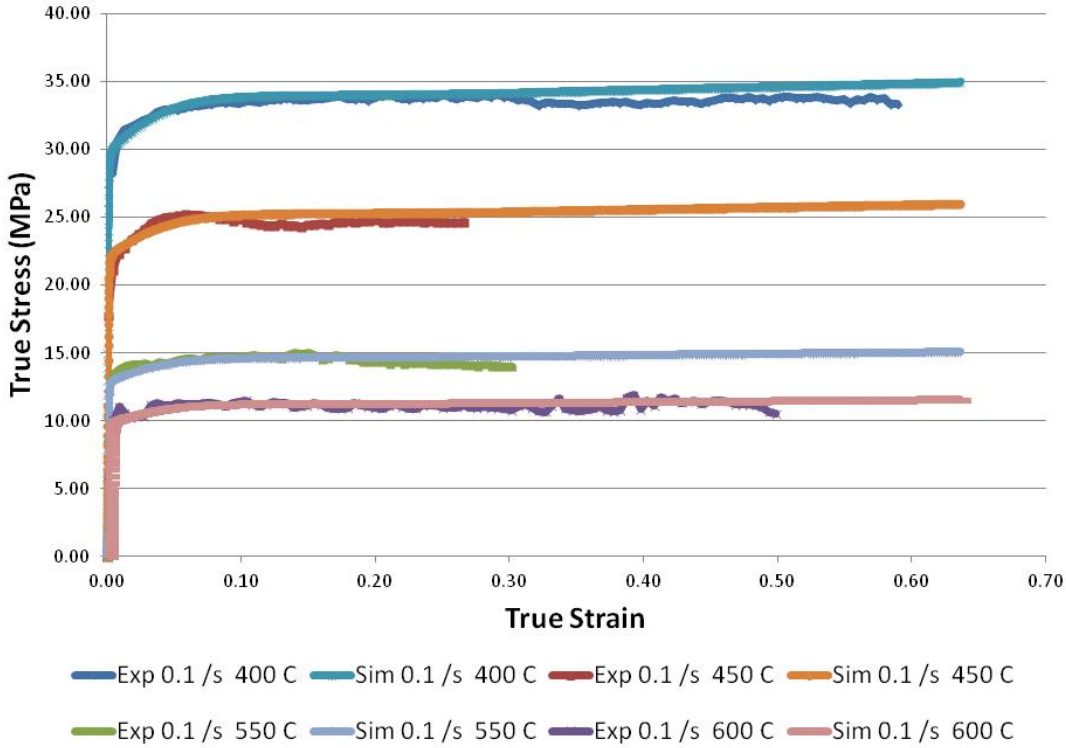

Figure 59: Experimental and simulated AA 6063 uniaxial compression stress-strain curves at 0.1 s^{-1}

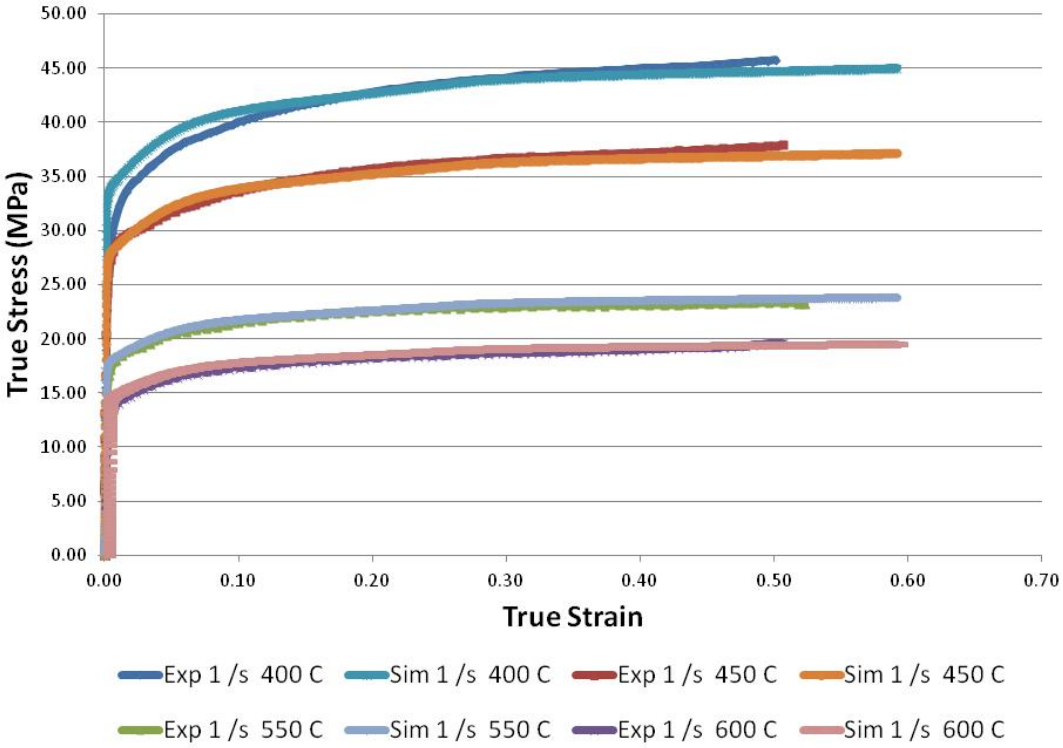

Figure 60: Experimental and simulated AA 6063 uniaxial compression stress-strain curves at 1 s^{-1}

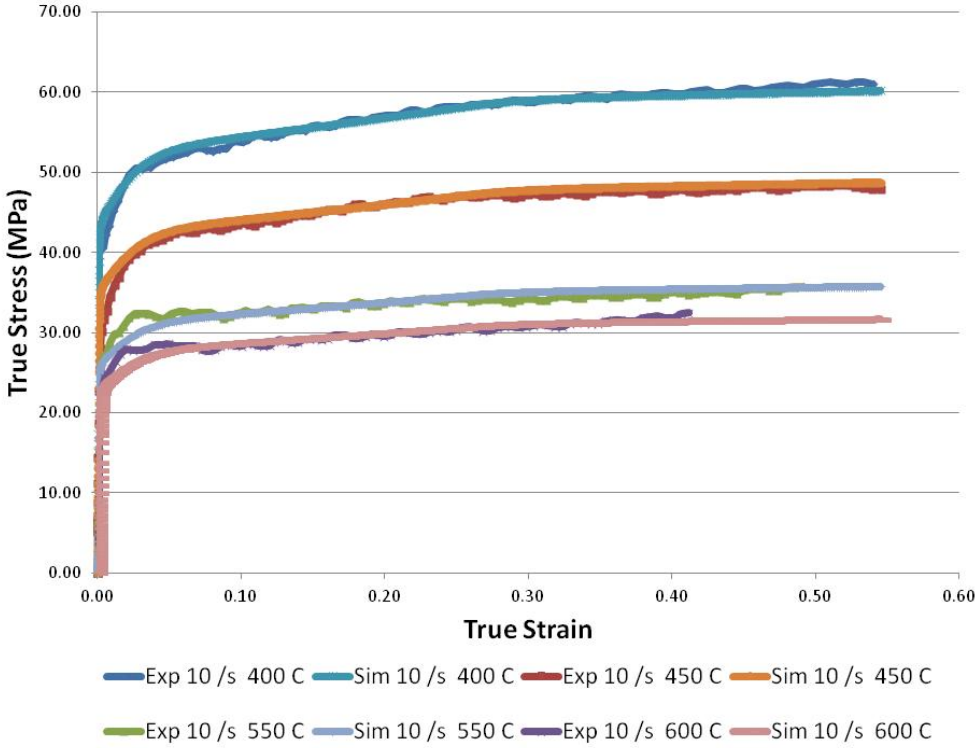

Figure 61: Experimental and simulated AA 6063 uniaxial compression stress-strain curves at 10 s^{-1}

6.3.5 Model Validation

It is important to validate the model with non-calibrated data to assess the predicting capabilities. Therefore, the model was validated with uniaxial compression results from 500^0C (Figure 62). Simulated results for all strain-rates show excellent predictions for most cases. The model over predicts results for 10 s^{-1} after 20% strain by a maximum of 5 MPa due to extra hardening in the material during simulations. Even though the modified hardening model indirectly incorporates high temperature mechanisms such as climb, cross-slip, glide, etc. the over-prediction of the model at 10 s^{-1}could be due to these high temperature mechanisms. However, most of these high temperature mechanisms are only active at low strain-rates.

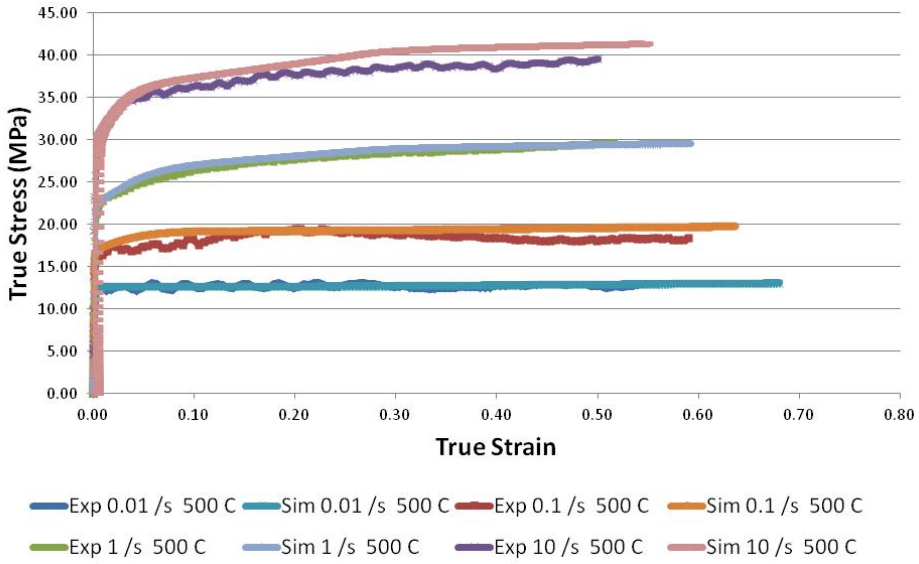

Figure 62: Experimental and simulated uniaxial compression stress-strain results for AA 6063 at 500^0C

Results in Section 5.3.3-5.3.5 show calibration, verification and validation of the stress-strain response of AA 6063 under uniaxial compression at various temperatures and strain-rates. However, crystal plasticity models are also expected to predict the texture evolution in the material during deformation which is discussed in the next section.

6.3.6 Modelling Texture Evolution

In-house Taylor based crystal plasticity model was also used to compare the texture evolution after deformation with experimental results. Deformed AA 6063 texture was measured using 2D XRD Brucker D8 Discover at various temperatures and strain-rates. Pandey et al. [191] have shown that texture data at different temperatures represented using pole figures does not show adequate differences in texture. Therefore, only ODF data was plotted and compared to simulated results.

6.3.6.1 AA 6063 Experimental Results

ODF textures were measured at different temperatures and strain-rates after deformation with a Brucker D8 Discover 2D X-Ray Detector and are presented in Figure 63. Figure 63a & c show the texture evolution at constant strain-rate (with varying temperatures) while Figure 63b & c show texture evolution at constant temperature (with varying strain-rates). ODF results for initial texture are given in Figure 54. Figure 63a-c show almost no Cube, Copper, S, Goss and Brass in the ODF's. Initial texture also lacked Cube, Brass and Goss but had Copper and S component. Therefore, it is concluded that most of the well-known texture components were not present in the deformed model.

Initial and final ODF, show peaks near (45, 0, 0) and (45, 90, 0) in all cases. However, the peak intensity increases with temperature and decreases with strain-rate. Initial 45^0 ODF section shows peaks near (0, 45, 45) and (0, 0, 45). These peaks form a fiber from (0, 0, 45) to (0, 90, 45) as shown in Figure 63. The intensity of this fiber does not change with temperature but increases with strain rate (Figure 63b &c). Initial and final ODF also show peak near (55, 55, 45) and (50, 65, 65). The intensity increases with decrease in temperature and increase in strain-rate.

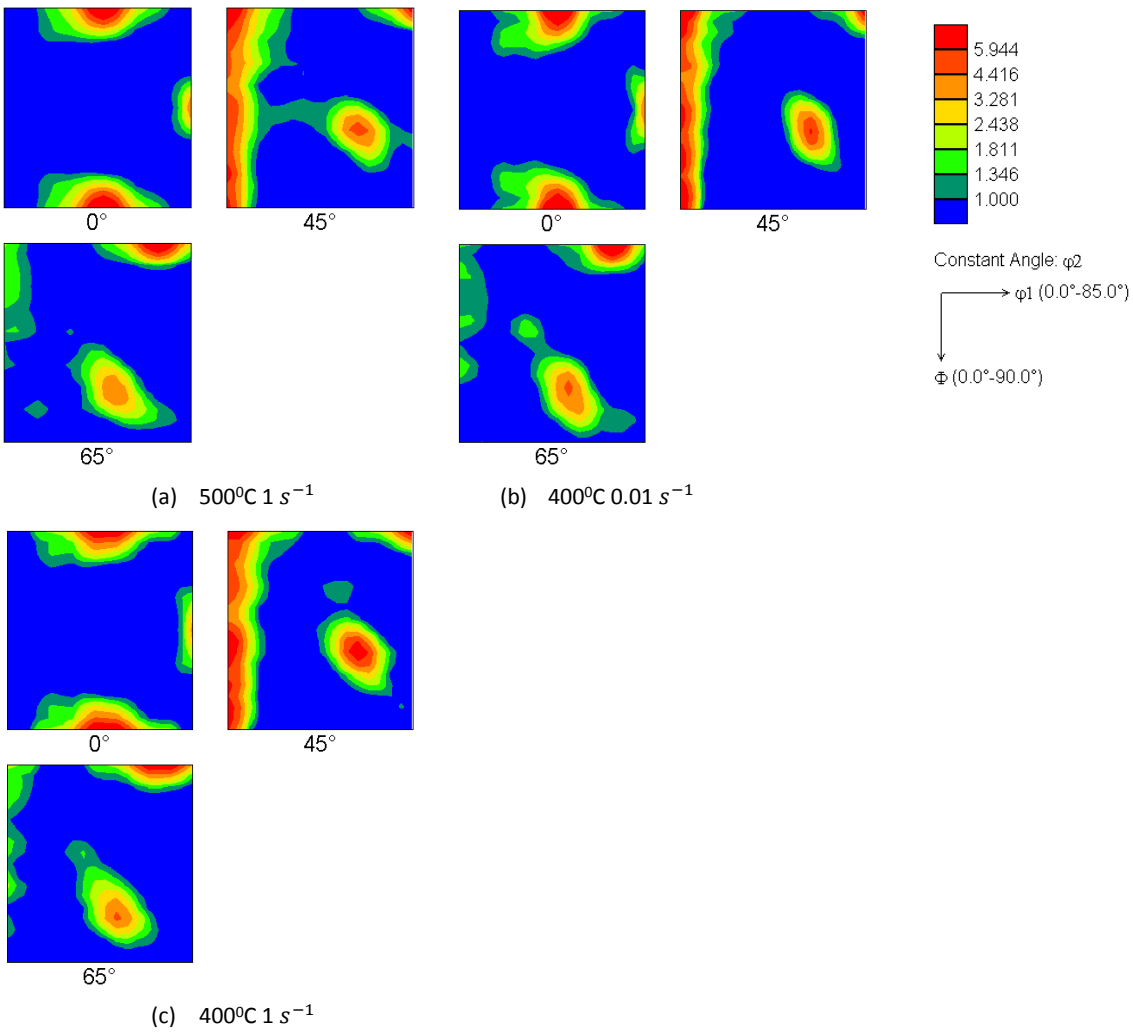

Figure 63: Experimental deformed AA 6063 ODF plots (φ_2-sections) at (a) 500⁰C 1 s^{-1} (b) 400⁰C 0.01 s^{-1} and (c) 400⁰C 1 s^{-1}

6.3.6.2 AA 6063 Experimental and Crystal Plasticity Comparison

Experimental and crystal plasticity results are shown in Figure 64a & b for 400⁰C at 0.01 s^{-1}. Results show large discrepancies between experimental and simulated data in all ODF sections as effect of static recrystallization is not incorporated. The results show the importance of recrystallization for prediction of accurate texture at high temperatures.

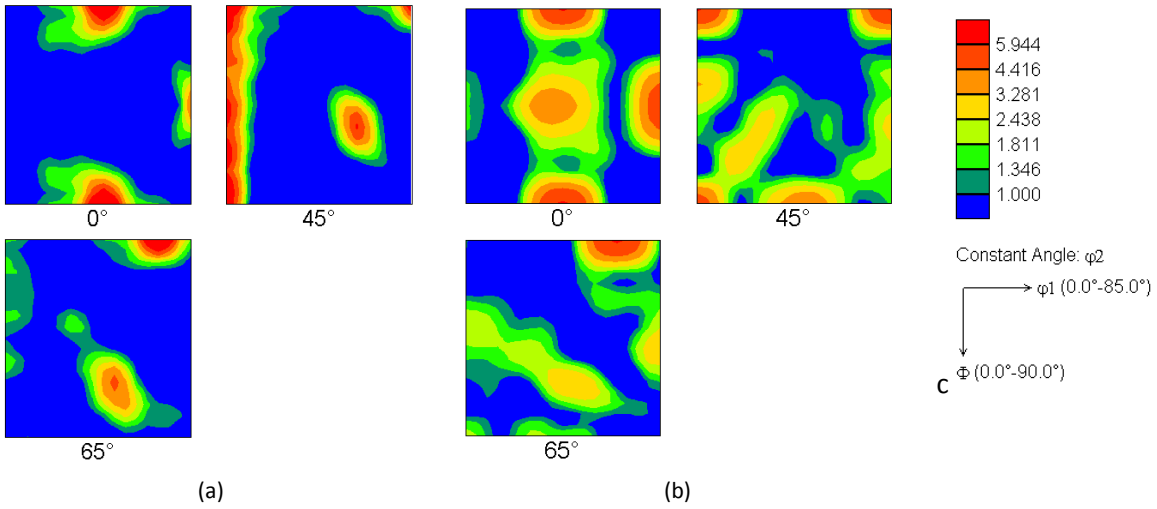

Figure 64: (a) Experimental and (b) Simulated AA 6063 ODF plots (φ_2-sections) at 400^{0}C 0.01 s^{-1}

6.3.6.3 AA 6063 Static Recrystallization Calibration and Validation

Section 5.3.6.2 shows the importance of considering the effects of recrystallization at high temperatures. Static recrystallization framework discussed in Section 4.2 was used to predict accurate textures subsequent to the crystal plasticity simulations. Texture and shear stress data from crystal plasticity simulations were the main inputs into the SRX model.

SRX model parameters discussed in Section 6.3 were calibrated at 400^{0}C 0.01 s^{-1} to get the optimum texture after recrystallization as shown in Figure 65b. Simulated SRX results for the 0^0, 45^0 and 65^0 ODF showed similar trends and intensities to experimental data (Figure 63b) for all ODF sections. However, simulations predicted higher intensities near (90, 45, 0) and lower intensities near (55, 55, 45) and (50, 65, 65). In addition, simulations did not capture the complete fiber seen in 45^0 ODF.

To validate the SRX model, simulated results at 500^{0}C 1 s^{-1} and 400^{0}C 1 s^{-1} were compared to experimental results shown in Figure 63. Simulated results at 500^{0}C 1 s^{-1} and 400^{0}C 1 $s^{-1}$are shown in Figure 65a & c. Simulated results at 500^{0}C 1 s^{-1} captured most of the experimental ODF peaks with minor deviations in 45^0 ODF. Simulated results for 400^{0}C 1 s^{-1} also captured most of the experimental ODF peaks with minor deviations as seen in Figure 65c.

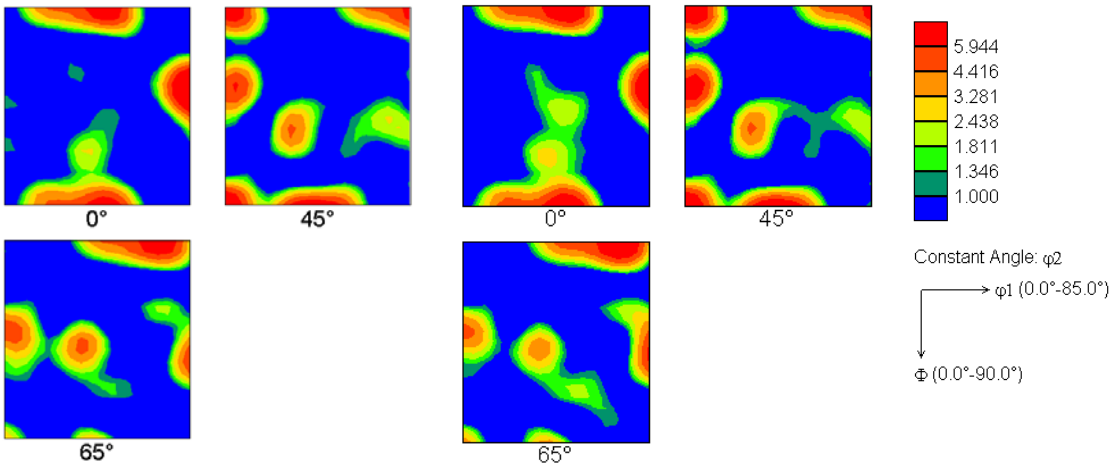

(a) 500^{0}C 1 s^{-1} (b) 400^{0}C 0.01 s^{-1}

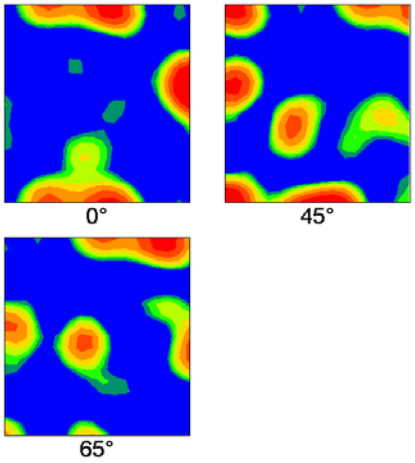

(c) 400^{0}C 1 s^{-1}

Figure 65: Simulated deformed AA 6063 ODF plots (φ_2-sections) at (a) 500^{0}C 1 s^{-1} (b) 400^{0}C 0.01 s^{-1} and (c) 400^{0}C 1 s^{-1}

Experimental results at different strain-rates and temperatures also allow the study of texture trends. At 1 s^{-1}, experimental results showed an increase in peak intensity at (50, 65, 65) and (55, 55, 45) with increase in temperature. In addition, experimental (45, 0, 0) and (45, 90, 0) peaks showed negligible change with temperature. Both these trends were also successfully captured by SRX simulations.

Simulated and experimental results at 400^{0}C showed a decrease in intensity near the (45, 0, 0) and (45, 90, 0) with increase in strain-rate. Experimental results also showed an increase in intensity near the (50, 65, 65) and (55, 55, 45) which was also captured by simulated results.

6.3.7 AA 6063 Experimental and Simulated Grain Size

Texture prediction is an effective tool as many mechanical properties are texture dependent. However, grain size also plays an important part in the final mechanical properties. Therefore it is important to be able to account for change in grain size after deformation. Many mechanical properties are directly related to grain size and it is commonly known that a decrease in grain size improves the strength (Hall-Petch effect) [26] and toughness of the material [172, 173]. Analytical models for recrystallization lack the capability of predicting the overall microstructure and grain size evolution (e.g. [109]). Various non-analytical non-coupled recrystallization models presented in literature have successfully predicted change in texture and grain size (e.g. [114, 136]). In this work, a complete through process model is presented that can predict the stress-strain response, texture and grain size evolution during compression.

Initial and final grain sizes were measured based on optical micrograph data. Figure 66 shows some of the optical micrograph data in the undeformed (Figure 66a) and deformed states at various temperatures and strain-rates.

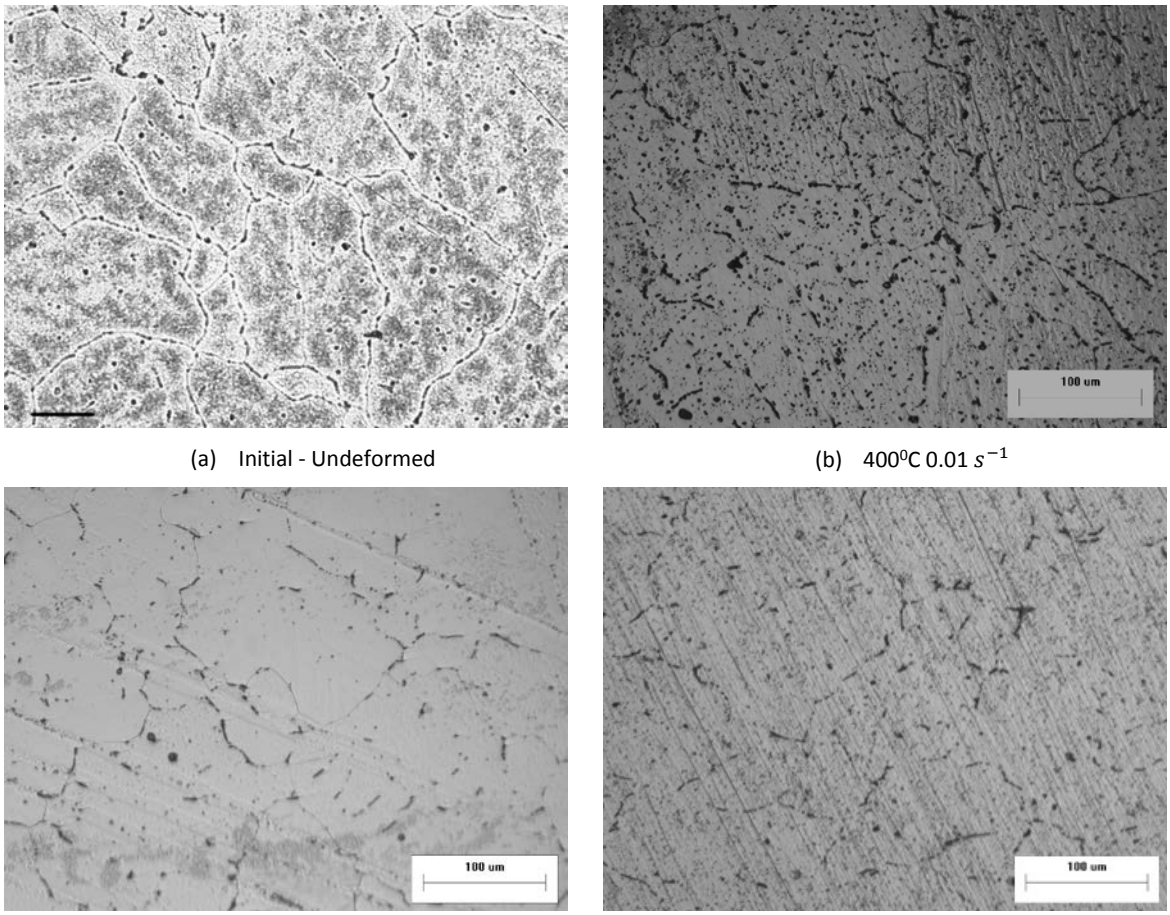

(a) Initial - Undeformed

(b) 400^{0}C 0.01 s^{-1}

(c) 600^{0}C 0.01 s^{-1}

(d) 400^{0}C 0.1 s^{-1}

Figure 66: (a) Initial micrograph (black line represents 50 µm) (b) Deformed micrograph at 400^{0}C 0.01 s^{-1} (c) Deformed micrograph at 600^{0}C 0.01 s^{-1} (d) Deformed micrograph at 400^{0}C 0.1 s^{-1}

In this work, change in average grain size is found using Equation 93. Equation 93 is based on the work by Raabe [109] and assumes 100% recrystallization. As the initial grain size is known, change in grain size (Δn^t) at time (t) is calculated as:

$$\Delta n^t = (\Delta V^t{}_{Rx})^{1/3} = \left[\Delta N^t exp\left(\frac{H_m}{kT}\right)\Delta P^t \Delta t\right]^{1/3} \quad \textbf{(93)}$$

Where $\Delta \mathrm{n}^{\mathrm{t}}$ is the change in grain size based on the pre-deformed sample, $\Delta \mathrm{V}^{\mathrm{t}}{}_{\mathrm{Rx}}$ is the volume fraction of recrystallized grains and N is the number of nuclei. Simulated and experimental results for the final average grain size are shown in Figure 67. Results show good agreement with experimental observations for most cases with minor deviations for 600^{0}C at 0.01 s^{-1} and 400^{0}C at 10 s^{-1}. Simulated results also predict the correct experimental trends and show an increase in grain size as strain-rate decreases and temperature increases.

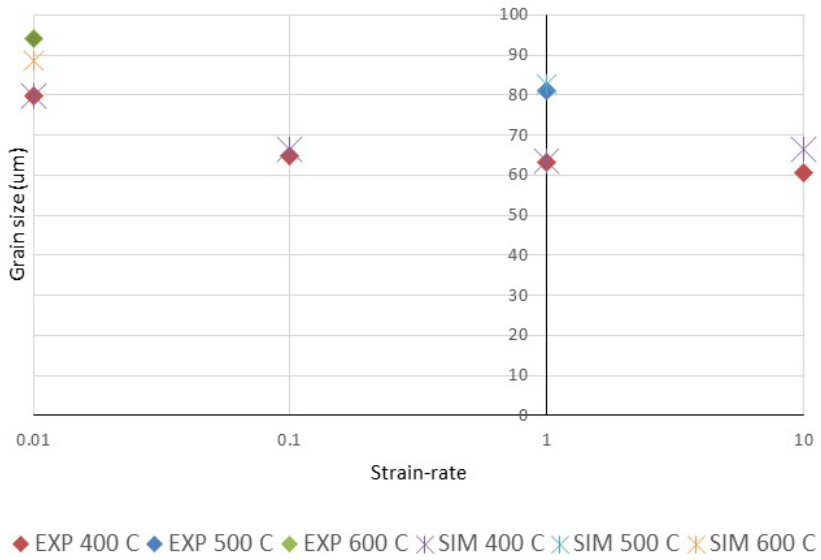

Figure 67: Experimental and simulated AA 6063 grain size predictions

6.3.8 Summary and Conclusions

In this section, a modified rate-dependent Taylor based crystal plasticity framework is presented that accounts for both the temperature and strain-rate effects. Temperature and strain-rate effects are accounted by incorporating them in the hardening and the elastic constants of the material. Proposed hardening model is calibrated, verified and validated with experimental stress-strain data on AA 6063 under hot compression. It is concluded that the proposed model can predict the stress-strain response of AA 6063 under compression from 400^0C to 600^0C at 0.01 s^{-1} to 10 s^{-1}.

To study the texture evolution, 2D XRD experiments were performed to capture the differences in texture at different temperatures and strain-rates. Results from optical microscopy were also used to measure grain size at different temperatures and strain-rates. It was concluded that the results from crystal plasticity simulations alone cannot capture the texture evolution during high temperature compression. Therefore, a new static recrystallization (SRX) model was developed to simulate the texture and grain size evolution during high temperature compression. Results from SRX model match the experimental texture trends under different temperatures and strain-rates. In addition, comparison of experimental and simulated grain size predictions show good agreement. It should be noted that the crystal plasticity model and the SRX model presented in this thesis serves as a stepping stone for optimizing the through process modelling of high temperature forming operations such as extrusion [85, 206].

Chapter 7 Future Work

Cold rolling simulations along with the grain analysis code presented in this thesis serve as a stepping stone for future work in grain analysis and other large strain problems. Similarly, static recrystallization code discussed in this thesis can be used to simulate various problems like annealing, etc. Some extensions to the current grain analysis code for large strain deformations and simulating recrystallization are mentioned below.

7.1 Crystal Plasticity Formulation

As CPFEM simulations are time consuming, it is of utmost importance to be able to model larger models to account for complete microstructural information. CPFEM model presented in this work captures the complete through thickness but is unable to capture the material in RD and ND and hence assumes an RVE in those directions. Extension of crystal plasticity framework to other computationally efficient methods like Fast Fourier Spectral methods [207], machine learning methods [208] would help in capturing the complete through thickness of the material in all directions without any assumptions.

7.2 Grain Analysis Code (gCode)

Asymmetric rolling is used extensively to increase formability of aluminum sheets [20]. Current methodology can be used to model asymmetric rolling and use the gCode to study the evolution of γ-fiber under various conditions to find the optimum roll speed for formability. In addition, current model lacks the ability to apply exact experimental velocities during simulation. Therefore, the current model can be extended to incorporate the input velocities to the CPEFG model from experimental DIC data.

Currently gCode lacks the capability to track texture evolution of individual texture components. Shear bands formation leads to material failure and are of great importance [209–211]. It is well known that formation of shear bands is heavily dependent on the starting texture and its neighborhood. Extension of gCode in this area would help in the prediction of shear bands and favorable and non-favorable orientations in this regard under different loading conditions.

7.3 Static Recrystallization (SRX) Code

SRX code presented in this thesis can be extended to CPFEM and CPEFG simulations with more microstructural information. Current code will need to be modified to a Cellular Automata probabilistic integration point based SRX model to model SRX using CPFEM/CPEFG. This would help in better predictions in texture and grain size. In addition, AA 6xxx and AA 7xxx alloys are precipitation hardened alloys (e.g. [212–214]) and it is well-known that particles can be a source of nuclei during recrystallization while certain precipitates can impede recrystallization [215]. Current SRX code does not account for the effect of precipitates. Therefore an extension of the SRX model to incorporate the effects of precipitates and particles would help in understanding their effect on the final material properties.

Current literature and proposed model lacks the effect of heating and cooling rates on texture and grain size during SRX. As material formability is directly affected by the final texture and grain size, it is of utmost importance to industry to be able to simulate the effect various heating rates on material texture and formability. This would also enable the study of various annealing processes on material texture and grain size.

References

[1] J. R. Davis, *Corrosion of aluminum and aluminum alloys*. ASM International, 1999.

[2] I. N. Fridlyander, V. G. Sister, O. E. Grushko, V. V. Berstenev, L. M. Sheveleva, and L. A. Ivanova, "Aluminum alloys: Promising materials in the automotive industry," *Metal Science and Heat Treatment*, vol. 44, no. 9–10. pp. 365–370, 2002.

[3] Ducker Worldwide, "2015 North American Light Vehicle Aluminum Content Study," 2015.

[4] A. I. Taub, P. E. Krajewski, A. A. Luo, and J. N. Owens, "The Evolution of Technology for Materials Processing over the Last 50 Years : The Automotive Example," *JOM*, vol. 59, no. 2, pp. 48–57, 2007.

[5] G. S. Cole and A. M. Sherman, "Light weight materials for automotive applications," *Mater. Charact.*, vol. 35, no. 1, pp. 3–9, 1995.

[6] K. Inal, P. D. Wu, and K. W. Neale, "Simulation of earing in textured aluminum sheets," *Int. J. Plast.*, vol. 16, pp. 635–648, 2000.

[7] K. K. Mathur and P. R. Dawson, "On Modelling and Development Of Crystallographic Texture In Bulk Forming Processes," *Int. J. Plast.*, vol. 5, pp. 67–94, 1989.

[8] U. Ali, A. Brahme, R. K. Mishra, and K. Inal, "Multi-scale Numerical Modeling of Rolling Using A Crystal Plasticity Based Element Free Galerkin Model," in *SPD 06*, 2014.

[9] H. R. Le and M. P. F. Sutcliffe, "Analysis of surface roughness of cold-rolled aluminium foil," *Wear*, vol. 244, no. 1–2, pp. 71–78, 2000.

[10] F. Roters, P. Eisenlohr, L. Hantcherli, D. D. Tjahjanto, T. R. Bieler, and D. Raabe, "Overview of constitutive laws, kinematics, homogenization and multiscale methods in crystal plasticity finite-element modeling: Theory, experiments, applications," *Acta Mater.*, vol. 58, no. 4, pp. 1152–1211, 2010.

[11] A. Brahme, M. H. Alvi, D. Saylor, J. Fridy, and A. D. Rollett, "3D reconstruction of microstructure in a commercial purity aluminum," *Scr. Mater.*, vol. 55, no. 1, pp. 75–80, 2006.

[12] D. Ghaffari Tari, M. J. Worswick, U. Ali, and M. A. Gharghouri, “Mechanical response of AZ31B magnesium alloy: Experimental characterization and material modeling considering proportional loading at room temperature,” *Int. J. Plast.*, vol. 55, pp. 247–267, 2014.

[13] C. P. Kohar, A. Zhumagulov, A. Brahme, M. J. Worswick, R. K. Mishra, and K. Inal, “Development of high crush efficient, extrudable aluminium front rails for vehicle lightweighting,” *Int. J. Impact Eng.*, vol. 95, pp. 17–34, 2016.

[14] P. D. Wu, K. W. Neale, E. Giessen, M. Jain, A. Makinde, and S. R. MacEwen, “Crystal plasticity forming limit diagram analysis of rolled aluminum sheets,” *Metall. Mater. Trans. A*, vol. 29, no. 2, pp. 527–535, 1998.

[15] E. D. Cyr, M. Mohammadi, R. K. Mishra, and K. Inal, “A Three Dimensional (3D) Thermo-Elasto-Viscoplastic Constitutive Model for FCC Polycrystals,” *Int. J. Plast.*, vol. 70, pp. 166–190, 2015.

[16] K. Inal, K. W. Neale, and A. Aboutajeddine, “Forming limit comparisons for FCC and BCC sheets,” *Int. J. Plast.*, vol. 21, pp. 1255–1266, 2005.

[17] J. Lévesque, K. Inal, K. W. Neale, and R. K. Mishra, “Numerical modeling of formability of extruded magnesium alloy tubes,” *Int. J. Plast.*, vol. 26, no. 1, pp. 65–83, 2010.

[18] M. Knezevic, B. Drach, M. Ardeljan, and I. J. Beyerlein, “Three dimensional predictions of grain scale plasticity and grain boundaries using crystal plasticity finite element models,” *Comput. Methods Appl. Mech. Eng.*, May 2014.

[19] J. Hirsch and K. Lücke, “Overview no. 76: Mechanism of deformation and development of rolling textures in polycrystalline f.c.c. metals—II. Simulation and interpretation of experiments on the basis of Taylor-type theories,” *Acta Metall.*, vol. 36, no. 76, pp. 2883–2904, 1988.

[20] S. Chen, X. Liu, and L. Liu, “Grain statistics effect on deformation behavior in asymmetric rolling of pure copper foil by crystal plasticity finite element model,” *Trans. Nonferrous Met. Soc. China*, vol. 25, no. 10, pp. 3370–3380, 2015.

[21] O. V. Mishin, B. Bay, and D. J. Jenson, “Through-Thickness Texture Gradients in Cold-Rolled Aluminum,” *Metall. Mater. Trans. A*, vol. 3A, pp. 1653–1662, 2000.

[22] J. Dolbow and T. Belytschko, “An Introduction to Programming the Meshless Element Free Galerkin Method,” pp. 1–41, 1998.

[23] Y. Y. Lu, T. Belytschko, and L. Gu, “A new implementation of the element free Galerkin method,” *Comput. Methods Appl. Mech. Eng.*, vol. 113, no. 3–4, pp. 397–414, 1994.

[24] H. J. Mcqueen, S. Spigerelli, M. E. Kassner, and E. Evangelista, *Hot deformation and processing of aluminum alloys*. 2011.

[25] Y. S. Sato and H. Kokawa, “Distribution of tensile property and microstructure in friction stir weld of 6063 aluminum,” *Metall. Mater. Trans. A*, vol. 32, no. 12, pp. 3023–3031, 2001.

[26] N. Hansen, “The effect of grain size and strain on the tensile flow stress of aluminium at room temperature,” *Acta Metall.*, vol. 25, no. 8, pp. 863–869, 1977.

[27] M. Hölscher, D. Raabe, and K. Lücke, “Relationship between rolling textures and shear textures in f.c.c. and b.c.c. metals,” *Acta Metall. Mater.*, vol. 42, no. 3, pp. 879–886, 1994.

[28] P. Yap, “Grid-based path-finding,” in *Conference of the Canadian Society for Computational Studies of Intelligence*, 2002, pp. 44–45.

[29] D. G. Tari and M. J. Worswick, “Experimental investigation of anisotropy evolution of AZ31 magnesium alloy sheets under tensile loading,” in *AIP Conference Proceedings*, 2011, vol. 1353, pp. 1547–1552.

[30] D. G. Tari, M. J. Worswick, and U. Ali, “Asymmetric Yield Locus Evolution for HCP Materials: A Continuum Constitutive Modeling Approach,” *Key Eng. Mater.*, vol. 554–557, pp. 1184–1188, 2013.

[31] W. Muhammad, M. Mohammadi, J. Kang, R. K. Mishra, and K. Inal, “An elasto-plastic constitutive model for evolving asymmetric/anisotropic hardening behavior of AZ31B and ZEK100 magnesium alloy sheets considering monotonic and reverse loading paths,” *Int. J. Plast.*, vol. 70, pp. 30–59, 2015.

[32] C. P. Kohar, M. Mohammadi, R. K. Mishra, and K. Inal, “Effects of elastic–plastic behaviour on the axial crush response of square tubes,” *Thin-Walled Struct.*, vol. 93, pp. 64–87, 2015.

[33] U. Ali and R. A. Fraser, “Numerical Modeling of Rear Subframe Under Different Loading Conditions,” *SAE Tech. Pap.*, Apr. 2013.

[34] P. Gujarati, “Different crystal structures of engineering materials,” 2012. [Online]. Available: http://www.indiastudychannel.com/resources/150693-Different-crystal-structures-of-engineering-materials.aspx.

[35] W. D. Callister, *Material Science and Engineering An Introduction*, Seventh Ed. Newyork, NY: Wiley, 2003.

[36] G. I. Taylor, “The Mechanism of Plastic Deformation of Crystals. Part I. Theoretical,” *Proc. R. Soc. A Math. Phys. Eng. Sci.*, vol. 145, no. 855, pp. 362–387, Jul. 1934.

[37] E. Schmid, “Yield Point of Crystals - Critical Shear Stress Law,” *Proc. Int. Cong. Appl. Mech.*, p. 342, 1924.

[38] G. I. Taylor, “Plastic Strain in Metals,” *J. Inst. Met.*, vol. 62, pp. 307–324, 1938.

[39] J. F. W. Bishop and R. Hill, “A theory of the plastic distortion of a polycrystalline aggregate under combined stresses,” *Philos. Mag. Ser. 7*, vol. 42, no. 327, pp. 412–442, 1957.

[40] G. Y. Chin and W. L. Mammel, “Generalization and Equivalence of the Minimum Work (Taylor) and Maximum Work (Bishop-Hill) Principles for Crystal Plasticity,” *Trans. Metall. Soc. AIME*, vol. 245, no. 6, pp. 1211–1214, 1969.

[41] J. Ascough, “A single step finite element analysis of the temperature distribution around a moving laser heat source,” *Opt. Lasers Eng.*, vol. 6, no. 3, pp. 137–143, Jan. 1985.

[42] R. J. Asaro and A. Needleman, “Texture Development and Strain Hardening In Rate Dependent Polyrystals,” *Acta Metall.*, vol. 33, no. 42, pp. 923–953, 1985.

[43] G. Sachs, “Zur Ableitung einer Filebedingung,” *Zeitschrift des Vereines Dtsch.*, vol. 72, pp. 734–736, 1928.

[44] A. Kochendorfer, *Plastiche Eigenschaften von Kristallen und Metallischen Werkstoffen*. Berlin: Springer, 1941.

[45] J. F. W. Bishop and R. Hill, “A theory of the plastic distortion of a polycrystalline aggregate under combined stresses,” *Philos. Mag.*, vol. 42, pp. 414–427, 1951.

[46] J. F. W. Bishop and R. Hill, “A theoretical derivation of the plastic properties of a polycrystalline face centered metal,” *Philos. Mag.*, vol. 42, pp. 1298–1307, 1951.

[47] H. Honneff and H. Mecking, “A Method for the Determination of the Active Slip Systems and Orientation Changes During Single Crystal Deformation,” in *Proceedings of ICOTOM 5*, 1978, pp. 265–275.

[48] G. R. Canova, U. F. Kocks, and J. J. Jonas, “Theory of Torsion Texture Development,” *Acta Metall. Sin. English Lett.*, vol. 32, pp. 211–226, 1984.

[49] E. Kröner, “Berechnung der Elastischen Konstanten des Vielkristalls aus den Konstanten des Einkristalls,” *Zeitschrift für Phys.*, vol. 151, pp. 504–518, 1958.

[50] R. Hill, “Continuum Micro-Mechanics of Elasto-Plastic Polycrystals,” *J. Mech. Phys. Solids*, vol. 13, pp. 89–101, 1965.

[51] J. D. Eshelby, “The Determination of the Elastic Field of an Ellipsoidal Inclusion, and Related Problems,” *Proceeding R. Soc. A Math. Phys. Eng. Sci.*, vol. 241, no. 1226, pp. 376–396, 1957.

[52] R. A. Lebensohn and C. N. Tome, “A self-consistent anisotropic approach for the simulation of plastic deformation and texture development of polycrystals: application to zirconium alloys,” *Acta Metall.*, vol. 41, pp. 2611–2624, 1993.

[53] R. A. Lebensohn, C. N. Tomé, and P. P. Castaneda, “Self-consistent modelling of the mechanical behaviour of viscoplastic polycrystals incorporating intragranular field fluctuations.,” *Philos. Mag.*, vol. 87, no. 28, pp. 4287–4322, 2007.

[54] H. Wang, B. Raeisinia, P. D. Wu, S. R. Agnew, and C. N. Tomé, “Evaluation of self-consistent polycrystal plasticity models for magnesium alloy AZ31B sheet.,” *Int. J. Solids Struct.*, vol. 47, no. 21, pp. 2905–2917, 2010.

[55] H. Wang, P. D. Wu, C. N. Tomé, and Y. Huang, “A finite strain elastic–viscoplastic self-consistent model for polycrystalline materials,” *J. Mech. Phys. Solids*, vol. 58, no. 4, pp. 594–612, 2010.

[56] R. A. Lebensohn and C. N. Tomé, “A self-consistent viscoplastic model: prediction of rolling textures of anisotropic polycrystals,” *Mater. Sci. Eng. A*, vol. 175, no. 1–2, pp. 71–82, 1994.

[57] A. Zamiri, F. Pourboghrat, and F. Barlat, “An effective computational algorithm for rate-independent crystal plasticity based on a single crystal yield surface with an application to tube hydroforming,” *Int. J. Plast.*, vol. 23, no. 7, pp. 1126–1147, 2007.

[58] I. Ulacia, C. P. Salisbury, I. Hurtado, and M. J. Worswick, “Tensile characterization and constitutive modeling of AZ31B magnesium alloy sheet over wide range of strain rates and temperatures,” *J. Mater. Process. Technol.*, vol. 211, no. 5, pp. 830–839, May 2011.

[59] K. Ghavam and R. Naghdabadi, “Constitutive modeling of temperature and strain rate dependent elastoplastic hardening materials using a corotational rate associated with the plastic deformation,” *Int. J. Plast.*, vol. 27, no. 9, pp. 1445–1455, Sep. 2011.

[60] F. Barlat, “Plastic Behaviour and Stretchability of Sheet Metals. Part I A Yield Function for Orthotropic Sheets Under Plane Stress Conditions,” 1986.

[61] J. Rossiter, A. Brahme, K. Inal, and R. K. Mishra, “Numerical analyses of surface roughness during bending of FCC single crystals and polycrystals,” *Int. J. Plast.*, vol. 46, pp. 82–93, 2013.

[62] J. Rossiter, A. Brahme, M. H. Simha, K. Inal, and R. K. Mishra, “A new crystal plasticity scheme for explicit time integration codes to simulate deformation in 3D microstructures: Effects of strain path, strain rate and thermal softening on localized deformation in the aluminum alloy 5754 during simple shear,” *Int. J. Plast.*, vol. 26, no. 12, pp. 1702–1725, 2010.

[63] U. Ali, A. P. Brahme, R. K. Mishra, and K. Inal, “New Methodology To Determine Stable Texture Components Under Cold Rolling In FCC Metals,” in *Light Metals 2016*, John Wiley & Sons Inc., 2016, pp. 159–162.

[64] U. Ali, A. Brahme, R. K. Mishra, and K. Inal, “Multi-Scale Modeling of Subgrain formation During Cold Rolling Using a Crystal Plasticity Based Element Free Galerkin Model,” in *TMS 2015*, 2015.

[65] D. Logan, *A First Course in the Finite Element Method*, Fourth Edi. Toronto, ON: Thomson, 2007.

[66] T. Belytschko, H. Chen, J. Xu, and G. Zi, “Dynamic crack propagation based on loss of hyperbolicity with a new discontinuous enrichment,” *Int J Numer Meth Eng*, vol. 55, pp. 1873–1905, 2003.

[67] J.-H. Song, P. Areias, and T. Belytschko, “A method for dynamic crack and shear band propagation with phantom nodes,” *Int J Numer Meth Eng*, vol. 67, pp. 868–893, 2006.

[68] U. Ali, “Numerical Modeling of Failure in Magnesium Alloys under Axial Compression and Bending for Crashworthiness Applications,” MASc thesis, University of Waterloo, Waterloo, ON, 2012.

[69] J.-H. Song, H. Wang, and T. Belytschko, “A comparative study on finite element methods for dynamic fracture,” *Comput. Mech.*, vol. 42, no. 2, pp. 239–250, 2007.

[70] T. Belytschko, Y. Lu, and L. Gu, “Element Free Galerkin Methods,” *Int. J. Numer. Methods Eng.*, vol. 37, pp. 229–256, 1994.

[71] G. Hu and P. Wriggers, “On the adaptive finite element method of steady-state rolling contact for hyperelasticity in finite deformations,” *Comput. Methods Appl. Mech. Eng.*, vol. 191, no. 13–14, pp. 1333–1348, 2002.

[72] J. Melenk and I. Babuska, “The partition of unity finite element method: Basic theory and applications,” *Comput. Methods Appl. Mech. Eng.*, vol. 39, pp. 289–314, 1996.

[73] T. Belytschko, Y. Krongauz, D. Organ, M. Fleming, and P. Krysl, “Meshless methods: An overview and recent developments,” *Comput. Methods Appl. Mech. Eng.*, vol. 139, no. 1–4, pp. 3–47, 1996.

[74] H. Moulinec and P. Suquet, “A fast numerical method for computing the linear and nonlinear mechanical properties of composites,” *C.R. Comptes Rendus la Acad. Sci. Paris Ser. II*, vol. 318, pp. 1417–1423, 1994.

[75] R. A. Lebensohn, “N-site modelling of a 3-D viscoplastic polycrystal using Fast Fourier Transform,” *Acta Mater.*, vol. 49, pp. 2723–2737, 2001.

[76] R. A. Lebensohn, C. N. Tome, and P. J. Maudlin, “Modelling Texture and Void Evolution in Polycrystals,” *Mater. Sci. Forum*, vol. 408, pp. 323–328, 2002.

[77] H. Bunge, “Zur Darstellung Allgemeiner Texturen,” *Z. Met.*, vol. 56, pp. 872–874, 1965.

[78] U. Kocks, C. Tome, and H.-R. Wenk, *Texture and Anisotropy: Preferred Orientations in Polycrystals and their Effect on Materials Properties*. Cambridge: Cambridge University Press, 1998.

[79] A. D. Rollett, “Texture Components and Euler Angles,” Class Notes, Department of Material Science and Engineering, Carnegie Mellon, Pittsburgh, PA, 2005.

[80] Y. Takahashi, K. Miyazawa, M. Mori, and Y. Ishida, “Quaternion representation of the orientation relationship and its application to grain boundary problems,” in *Trans. Japan Inst. Metals*, 1986, pp. 345–352.

[81] J. Cho, A. D. Rollett, and K. H. Oh, “Determination of a Mean Orientation in Electron Backscatter Diffraction Measurements of Average Orientations,” *Metall. Mater. Trans. A*, vol. 36, no. 12, pp. 3427–3438, 2005.

[82] J.-H. Cho, A. D. Rollett, and K. H. Oh, “Determination of volume fractions of texture components with standard distributions in Euler space,” *Metall. Mater. Trans. A*, vol. 35, no. 3, pp. 1075–1086, 2004.

[83] O. Engler, H. C. Kim, and M. Y. Huh, “Formation of {111} fibre texture in recrystallised aluminium sheet,” *Mater. Sci. Technol.*, vol. 17, no. 1, pp. 75–86, 2001.

[84] A. P. Brahme, “Modelling Microstructure Evolution during Recrystallization,” PhD Thesis. Carnegie Mellon University, Pittsburg, PA, 2005.

[85] K. Yoshida, T. Ishizaka, M. Kuroda, and S. Ikawa, “The effects of texture on formability of aluminum alloy sheets,” *Acta Mater.*, vol. 55, no. 13, pp. 4499–4506, 2007.

[86] D. J. Lloyd and L. R. Morris, “Luders band deformation in a fine grained aluminium alloy,” *Acta Metall.*, vol. 25, no. 8, pp. 857–861, 1977.

[87] P. D. Wu, D. J. Lloyd, A. Bosland, H. Jin, and S. R. MacEwen, “Analysis of roping in AA6111 automotive sheet,” *Acta Mater.*, vol. 51, no. 7, pp. 1945–1957, 2003.

[88] J. Rossiter, A. Brahme, K. Inal, and R. K. Mishra, “Distribution of stress triaxiality in face-centered cubic polycrystals under equibiaxial loading,” *Scr. Mater.*, vol. 65, no. 3, pp. 183–185, 2011.

[89] M. Cherkaoui and M. Berveiller, “Mechanics of Materials Undergoing Martensitic Phase Change: A Micro-Macto Approach for Transformation Induced Plasticity,” *J. Appl. Math. Mech.*, vol. 80, no. 4, pp. 219–232, 2000.

[90] E. Nakamachi, N. Tam, and H. Morimoto, “Multi-scale finite element analyses of sheet metals by using SEM-EBSD measured crystallographic RVE models,” *Int. J. Plast.*, vol. 23, no. 3, pp. 450–489, 2007.

[91] K. Inal, P. D. Wu, and K. W. Neale, “Instability and localized deformation in polycrystalline solids under plane-strain tension,” *Int. J. Solids Struct.*, vol. 39, no. 4, pp. 983–1002, Feb. 2002.

[92] A. J. Wilkinson and T. Ben Britton, “Strains, planes, and EBSD in materials science,” *Mater. Today*, vol. 15, no. 9, pp. 366–376, 2012.

[93] J. Rossiter, “Crystal Plasticity Based Modelling of Surface Roughness and Localized Deformation During Bending in Aluminum Polycrystals,” PhD Thesis. Univeristy of Waterloo, Waterloo, ON, 2015.

[94] S. Lichter and J. Chen, “Model for columnar microstructure of thin solid films,” *Phys. Rev. Lett.*, vol. 56, no. 13, pp. 1396–1399, 1986.

[95] D. Saylor, J. Fridy, B. El-Dasher, K. Jung, and A. Rollett, “Statistically representative three-dimensional microstructures based on orthogonal observation sections,” *Metall. Mater. Trans. A*, vol. 35, pp. 1969–1979, 2004.

[96] O. Diard, S. Leclercq, G. Rousselier, and G. Cailletaud, “Evaluation of finite element based analysis of 3D multicrystalline aggregates plasticity,” *Int. J. Plast.*, vol. 21, no. 4, pp. 691–722, 2005.

[97] G. Gottstein, *Physical foundations of material science*. Springer, 2004.

[98] P. Cotterill and P. R. Mould., *Recrystallization and grain growth in metals, Volume 266*. Surrey University Press London, 1976.

[99] E. Popova, “Crystal Plasticity Based Numerical Modelling of Dynamic Recrystallization in Magnesium Alloys,” PhD Thesis. University of Waterloo, Waterloo, ON, 2015.

[100] M. I. Bhatia, “Recrystallisation—Some applied aspects,” *Prog. Mater. Sci.*, vol. 52, no. 59–77, 1997.

[101] B. Radhakrishnan, G. B. Sarma, and T. Zacharia, “Modeling the kinetics and microstructural evolution during static recrystallization—Monte Carlo simulation of recrystallization,” *Acta Mater.*, vol. 46, no. 12, pp. 4415–4433, 1998.

[102] M. A. Martorano, H. R. Z. Sandim, M. A. Fortes, and A. F. Padilha, “Observations of grain boundary protrusions in static recrystallization of high-purity bcc metals,” *Scr. Mater.*, vol. 56, no. 10, pp. 903–906, 2007.

[103] X. Huang, K. Suzuki, and Y. Chino, “Static recrystallization and mechanical properties of Mg-4Y-3RE magnesium alloy sheet processed by differential speed rolling at 823K,” *Mater. Sci. Eng. A*, vol. 538, pp. 281–287, 2012.

[104] F. J. Humphreys and M. Hatherly, *Recrystallization and related annealing phenomena*. Elsevier Oxford, 2004.

[105] R. J. Asaro, *Advances in Applied Mechanics Volume 23*, vol. 23. 1983.

[106] H. C. H. Carpenter and C. F. Elam, “Crystal growth and recrystallziatoin in metals,” *Inst. Met.*, vol. 24, pp. 83–131, 1920.

[107] H. Alterthum, “Zur Theorie der Rekristallisation,” *Zeitschrift für Elektrochemie und Angew. Phys. Chemie*, vol. 28, no. 15–16, pp. 347–356, 1922.

[108] A. Rollett, “Overview of modeling and simulation of recrystallization,” *Prog. Mater. Sci.*, vol. 42, no. 1–4, pp. 79–99, 1997.

[109] D. Raabe, “A texture-component Avrami model for predicting recrystallization textures, kinetics and grain size,” *Model. Simul. Mater. Sci. Eng.*, vol. 15, no. 2, pp. 39–63, 2006.

[110] R. Sandstrom, “Subgrain growth occurring by boundary migration,” *Acta Metall.*, vol. 25, no. 8, pp. 905–911, 1977.

[111] R. Sandstrom and R. Lagneborg, “A model for hot working occurring by recrystallization,” *Acta Metall.*, vol. 23, no. 3, pp. 387–398, 1975.

[112] P. Anderson, D. J. Srolovitz, G. S. Crest, and P. S. Sahni, “Computer simulation of grain growth-I. kinetics,” *Acta Metall.*, vol. 32, no. 5, pp. 783–791, 1984.

[113] D. J. Srolovitz, G. S. Grest, M. P. Anderson, and A. D. Rollett, “Computer simulation of recrystallization-II. Heterogeneous nucleation and growth,” *Acta Metall.*, vol. 36, no. 8, pp. 2115–2128, 1988.

[114] E. Popova, Y. Staraselski, A. Brahme, R. K. Mishra, and K. Inal, “Coupled crystal plasticity – Probabilistic cellular automata approach to model dynamic recrystallization in magnesium alloys,” *Int. J. Plast.*, vol. 66, pp. 85–102, 2015.

[115] W. A. Johnson and R. F. Mehl, “Reaction kinetics in processes of nucleation and growth,” *Am. Inst. Min. Metall. Eng.*, vol. 135, pp. 416–442, 1939.

[116] M. Avrami, “Kinetics of phase change. I General theory,” *J. Chem. Phys.*, vol. 7, no. 12, pp. 1103–1112, 1939.

[117] M. Avrami, “Granulation, phase change, and microstructure kinetics of phase change. III,” *J. Chem. Phys.*, vol. 9, no. 2, pp. 177–184, 1941.

[118] A. N. Kolmogorov, “On the statistical theory of the crystallization of metals,” *Bull. Acad. Sci. USSR, Math. Ser.*, vol. 1, pp. 335–359, 1937.

[119] R. Sebald and G. Gottstein, “Modeling of recrystallization textures:: interaction of nucleation and growth,” *Acta Mater.*, vol. 50, no. 6, pp. 1587–1598, 2002.

[120] N. Metropolis and S. Ulam, “The monte carlo method,” *J. Am. Stat. Assoc.*, vol. 44, no. 247, pp. 335–341, 1949.

[121] R. B. Potts, “Some generalized order-disorder transitions,” *Proc. Cambridge Philosphical Soc.*, vol. 48, no. 1, pp. 106–109, 1952.

[122] E. Ising, “Beitrag zur Theorie des Ferro- und Paramagnetismus Dissertation,” *Zeitschrift für Phys.*, vol. 31, pp. 253–258, 1925.

[123] N. Metropolis, A. W. Rosenbluth, M. N. Rosenbluth, A. H. Teller, and E. Teller, “Equation of state calculations by fast computing machines,” *J. Chem. Phys.*, vol. 21, no. 6, pp. 1087–1092, 1953.

[124] E. A. Holm, “Modeling Microstructural Evolution in Single-Phase, Composite, and Two-Phase Polycrystals”; Ph.D. Thesis.,” PhD Thesis. University of Michigan, Ann Arbor, MI, 1992.

[125] H. Hallberg, “Approaches to modeling of recrystallization,” *Metals (Basel).*, vol. 1, no. 1, pp. 16–48, 2011.

[126] D. Fan and L.-Q. Chen, “Computer simulation of grain growth using a continuum field model,” *Acta Mater.*, vol. 45, no. 2, pp. 611–622, 1997.

[127] L.-Q. Chen, “Phase-Field Models for Microstructure Evolution,” *Annu. Rev. Mater. Res.*, vol. 32, pp. 113–140, 2002.

[128] M. A. Miodownik, “A review of microstructural computer models used to simulate grain growth and recrystallisation in aluminium alloys,” *J. Light Met.*, vol. 2, no. 3, pp. 125–135, 2002.

[129] V. Tikare, E. a. Holm, D. Fan, and L.-Q. Chen, “Comparison of phase-field and Potts models for coarsening processes,” *Acta Mater.*, vol. 47, no. 1, pp. 363–371, 1998.

[130] T. Takaki, Y. Hisakuni, T. Hirouchi, A. Yamanaka, and Y. Tomita., “Multi-phase- field simulations for dynamic recrystallization,” *Comput. Mater. Sci.*, vol. 45, no. 4, pp. 881–888, 2009.

[131] K. Kawasaki, T. Nagai, and K. Nakashima, “Vertex models for two-dimensional grain growth,” *Philos. Mag. B*, vol. 60, no. 3, pp. 399–421, 1989.

[132] K. Piekoś, J. Tarasiuk, K. Wierzbanowski, and B. Bacroix, “Generalized vertex model of recrystallization - Application to polycrystalline copper,” *Comput. Mater. Sci.*, vol. 42, no. 4, pp. 584–594, 2008.

[133] K. Brakke, *The Motion of a Surface by its Mean Curvature*. New Jersey: Princeton University Press, 1978.

[134] D. Weygand, Y. Bréchet, J. Lépinoux, and W. Gust, “Three-dimensional grain growth: A vertex dynamics simulation,” *Philos. Mag. B Phys. Condens. Matter; Stat. Mech. Electron. Opt. Magn. Prop.*, vol. 79, no. 5, pp. 703–716, 1999.

[135] D. Raabe, “Cellular automata in materials science with particular reference to recrystallization simulation,” *Annu. Rev. Mater. Res.*, vol. 32, pp. 53–76, 2002.

[136] H. Li, X. Sun, and H. Yang, “A multiscale three-dimensional cellular automata-crystal plasticity finite element model for predicting the interaction among heterogeneous deformation, DRX microstructural evolution and mechanical responses in titanium alloys,” *Int. J. Plast.*, 2016.

[137] F. Han, B. Tang, H. Kou, L. Cheng, J. Li, and Y. Feng, “Static recrystallization simulations by coupling cellular automata and crystal plasticity finite element method using a physically based model for nucleation,” *J. Mater. Sci.*, vol. 49, no. 8, pp. 3253–3267, Jan. 2014.

[138] D. Raabe and R. C. Becker, “Coupling of a crystal plasticity finite-element model with a probabilistic cellular automaton for simulating primary static recrystallization in aluminium,” *Model. Simul. Mater. Sci. Eng.*, vol. 8, no. 4, pp. 445–462, 2000.

[139] K. G. F. Janssens, “Random grid, three-dimensional, space-time coupled cellular automata for the simulation of recrystallization and grain growth,” *Model. Simul. Mater. Sci. Eng.*, vol. 11, no. 2, pp. 157–171, 2003.

[140] D. Raabe, “Introduction of a scalable three-dimensional cellular automaton with a probabilistic switching rule for the discrete mesoscale simulation of recrystallization phenomena,” *Philos. Mag. A*, vol. 79, no. 10, pp. 2339–2358, 1999.

[141] A. D. Rollett and D. Raabe, “A hybrid model for mesoscopic simulation of recrystallization,” *Comput. Mater. Sci.*, vol. 21, no. 1, pp. 69–78, 2001.

[142] H. Jin and D. J. Lloyd, “The different effects of asymmetric rolling and surface friction on formation of shear texture in aluminium alloy AA5754,” *Mater. Sci. Technol.*, vol. 26, no. 6, pp. 754–760, Jun. 2010.

[143] R. Hill and J. R. Rice, “Constitutive analysis of elastic-plastic crystals at arbitrary strain,” *J. Mech. Phys. Solids*, vol. 20, no. 6, pp. 401–413, Dec. 1972.

[144] D. Pierce, R. J. Asaro, and A. Needleman, “Material Rate Dependance And Localized Deformation In Crystalline Solids,” *Acta Metall.*, vol. 31, no. 12, pp. 1951–1976, 1983.

[145] J. L. Raphanel, G. Ravichandran, and Y. M. Leroy, “Three-dimensional rate-dependent crystal plasticity based on Runge-Kutta algorithms for update and consistent linearization,” *Int. J. Solids Struct.*, vol. 41, no. 22–23, pp. 5995–6021, 2004.

[146] R. W. Cahn, “A new theory of recrystallization nuclei,” in *Proceedings of the Physical Society. Section A*, 1950, pp. 323–336.

[147] G. Gottstein and L. S. Shvindlerman, *Grain boundary migration in metals: thermodynamics, kinetics, applications, Second Edition*. CRC Press, 2009.

[148] J. E. Bailey and P. B. Hirsch, “The recrystallization process in some polycrystalline metals,” *Proc. R. Soc. London. Ser. A. Math. Phys. Sci.*, vol. 267, no. 1328, pp. 11–30, 1962.

[149] W. Roberts and B. Ahlblom, “A nucleation criterion for dynamic recrystallization during hot working,” *Acta Metall.*, vol. 26, no. 5, pp. 801–813, 1978.

[150] A. Brahme, Y. Staraselski, R. K. Mishra, and K. Inal, “A New Model to Predict Grain Nucleation during Dynamic Recrystallization,” in *The 9th International Conference on Magnesium Alloys and their Applications*, 2012.

[151] J. F. Nye, “Some geometrical relations in dislocated crystals,” *Acta Metall.*, vol. 1, no. 2, pp. 153–162, 1953.

[152] A. Arsenlis and D. M. Parks, “Crystallographic aspects of geometrically-necessary and statistically-stored dislocation density,” *Acta Mater.*, vol. 47, no. 5, pp. 1597–1611, 1999.

[153] L. . Murr and D. Kuhlmann-Wilsdorf, “Experimental and theoretical observations on the relationship between dislocation cell size, dislocation density, residual hardness, peak pressure and pulse duration in shock-loaded nickel,” *Acta Metall.*, vol. 26, no. 5, pp. 847–857, 1978.

[154] W. T. Read and W. Shockley, “Dislocation models of crystal grain boundaries,” *Phys. Rev.*, vol. 78, no. 3, pp. 275–289, 1950.

[155] L. Edwards and M. Endean, *Manufacturing with Materials*. Milton Keynes: Open University Worldwide, 1990.

[156] J. Beddoes and M. J. Bibby, *Principles of Metals Manufacturing*. Burlighton, MA: Elsevier Butterworth-Heinemann, 1999.

[157] S. H. Lee and D. N. Lee, “Analysis of deformation textures of asymmetrically rolled steel sheets,” *Int. J. Mech. Sci.*, vol. 43, no. 9, pp. 1997–2015, Sep. 2001.

[158] C.-H. Choi, J.-W. Kwon, K. H. Oh, and D. N. Lee, “Analysis of Deformation Texture Inhomegeneity and Stability Condtion of Shear Components In F.C.C Metals,” *Acta Metall.*, vol. 45, no. 12, pp. 5119–5128, 1997.

[159] W. Mao and Z. Sun, “Inhomogeneity of rolling texture in Fe-28Al-2Cr alloy,” *Scr. Metall.*, vol. 29, no. 3, pp. 217–220, 1993.

[160] R. Roumina and C. W. Sinclair, “Deformation Geometry and Through-Thickness Strain Gradients in Asymmetric Rolling,” *Metall. Mater. Trans. A*, vol. 39, no. 10, pp. 2495–2503, 2008.

[161] K.-H. Jung, D.-K. Kim, Y.-T. Im, and Y.-S. Lee, “Crystal Plasticity Finite Element Analysis of Texture Evolution during Rolling of fcc Polycrystalline Metal,” *Mater. Trans.*, vol. 54, no. 5, pp. 769–775, 2013.

[162] J. C. Lin, “Prediction of Rolling Force and Deformation in Three-Dimensional Cold Rolling by Using the Finite-Element Method and a Neural Network,” *Int. J. Adv. Manuf. Technol.*, vol. 20, no. 11, pp. 799–806, 2002.

[163] Z. Chen, X. Zhang, C. Liu1, H. Cai, and F. Wang, “Computer Simulation of Rolling Textures Evolution of Pure Aluminum with Initial Texture,” *Mater. Trans.*, vol. 45, no. 9, pp. 2845–2850, 2004.

[164] L. Delannay and O. V. Mishin, “Crystal Plasticity Modeling of the Through-Thickness Texture Heterogeneity in Heavily Rolled Aluminum,” *Key Eng. Mater.*, vol. 554–557, pp. 1189–1194, Jun. 2013.

[165] N. Bozzolo, N. Dewobroto, H. R. Wenk, and F. Wagner, “Microstructure and microtexture of highly cold-rolled commercially pure titanium,” *J. Mater. Sci.*, vol. 42, no. 7, pp. 2405–2416, 2006.

[166] L. Delannay, P. J. Jacques, and S. R. Kalidindi, “Finite element modeling of crystal plasticity with grains shaped as truncated octahedrons,” *Int. J. Plast.*, vol. 22, no. 10, pp. 1879–1898, 2006.

[167] K. W. Neale, K. Inal, and P. D. Wu, “Effects of texture gradients and strain paths on localization phenomena in polycrystals,” *Int. J. Mech. Sci.*, vol. 45, no. 10, pp. 1671–1686, 2003.

[168] H. Jin and D. J. Lloyd, “The reduction of planar anisotropy by texture modification through asymmetric rolling and annealing in AA5754,” *Mater. Sci. Eng. A*, vol. 399, no. 1–2, pp. 358–367, Jun. 2005.

[169] K. Inal, P. D. Wu, and K. W. Neale, “Large strain behaviour of aluminium sheets subjected to in-plane simple shear,” *Model. Simul. Mater. Sci. Eng.*, vol. 10, no. 2, pp. 237–252, 2002.

[170] Y. Staraselski, A. P. Brahme, K. Inal, and R. K. Mishra, “Analytical estimation of distance–disorientation function of the material microstructure,” *Philos. Mag.*, vol. 93, no. 24, pp. 3314–3331, 2013.

[171] Z. Shan and A. M. Gokhale, “Representative volume element for non-uniform micro-structure,” *Comput. Mater. Sci.*, vol. 24, no. 3, pp. 361–379, 2002.

[172] Q. Cui and K. Ohori, “Grain refinement of high purity aluminium by asymmetric rolling,” *Mater. Sci. Technol.*, vol. 16, pp. 1095–1101, 2000.

[173] H. Jin and D. J. Lloyd, “The tensile response of a fine-grained AA5754 alloy produced by asymmetric rolling and annealing,” *Metall. Mater. Trans. A*, vol. 35, no. 13, pp. 997–1006, 2004.

[174] A. Azushima, R. Kopp, A. Korhonen, D. Y. Yang, F. Micari, G. D. Lahoti, P. Groche, J. Yanagimoto, N. Tsuji, A. Rosochowski, and A. Yanagida, “Severe plastic deformation (SPD) processes for metals,” *CIRP Ann. - Manuf. Technol.*, vol. 57, no. 2, pp. 716–735, Jan. 2008.

[175] M. Saravanan, R. M. Pillai, B. C. Pai, M. Brahmakumar, and K. R. Ravi, “Equal channel angular pressing of pure aluminium — an analysis,” vol. 29, no. 7, pp. 679–684, 2006.

[176] S. R. Kalidindi, B. R. Donohue, and S. Li, “Modeling texture evolution in equal channel angular extrusion using crystal plasticity finite element models,” *Int. J. Plast.*, vol. 25, no. 5, pp. 768–779, May 2009.

[177] P. D. Wu, Y. Huang, and D. J. Lloyd, “Studying grain fragmentation in ECAE by simulating simple shear,” *Scr. Mater.*, vol. 54, no. 12, pp. 2107–2112, Jun. 2006.

[178] M. Winning, G. Gottstein, and L. S. Shvindlerman, “Stress induced grain boundary motion,” *Acta Mater.*, vol. 49, no. 2, pp. 211–219, 2001.

[179] G. B. Sharma and P. R. Dawson, “Texture Predictions Using a Polycystal Plasticity Model Incorporating Neighbor Interactions,” *Int. J. Plast.*, vol. 12, no. 8, pp. 1023–1054, 1996.

[180] O. Engler, M. Crumback, and S. Li, “Alloy-dependent rolling texture simulation of aluminium alloys with a grain-interaction model,” *Acta Mater.*, vol. 53, no. 8, pp. 2241–2257, May 2005.

[181] S.-H. Choi and F. Barlat, “Prediction of macroscopic anisotropy in rolled aluminum-lithium sheet,” *Scr. Mater.*, vol. 41, no. 9, pp. 981–987, 1999.

[182] D. N. Lee and K. Kim, “Analysis of Deformation Textures of Asymmetrically Rolled Aluminum Sheets,” *Acta Mater.*, vol. 49, pp. 2583–2595, 2001.

[183] O. Engler, C. N. Tomé, and M.-Y. Huh, “A study of through-thickness texture gradients in rolled sheets,” *Metall. Mater. Trans. A*, vol. 31, no. 9, pp. 2299–2315, 2000.

[184] A. Styczynski, C. Hartig, J. Bohlen, and D. Letzig, “Cold rolling textures in AZ31 wrought magnesium alloy,” *Scr. Mater.*, vol. 50, no. 7, pp. 943–947, Apr. 2004.

[185] J. Hirsch and K. Lücke, “Overview no. 76: Mechanism of deformation and development of rolling textures in polycrystalline f.c.c. metals—I. Description of rolling texture development in homogeneous CuZn alloys,” *Acta Metall.*, vol. 36, no. 11, pp. 2863–2882, 1988.

[186] J. Hirsch, K. Lücke, and M. Hatherly, “Overview No. 76: Mechanism of deformation and development of rolling textures in polycrystalline f.c.c. Metals—III. The influence of slip inhomogeneities and twinning,” *Acta Metall.*, vol. 36, no. I, pp. 2905–2927, 1988.

[187] W. Truszkowski, J. Kr’ol, and B. Major, “Inhomogeneity of rolling texture in fcc metals.,” *Metall. Trans. A*, vol. 11, no. 5, pp. 749–758, 1980.

[188] W. Truszkowski, J. Krol, and B. Major, “On penetration of shear texture into the rolled aluminum and copper.,” *Metall. Trans. A*, vol. 13, no. 4, pp. 665–669, 1982.

[189] J. Kang, D. S. Wilkinson, M. Bruhis, M. Jain, P. D. Wu, J. D. Embury, R. K. Mishra, and A. K. Sachdev, “Shear Localization and Damage in AA5754 Aluminum Alloy Sheets,” *J. Mater. Eng. Perform.*, vol. 17, no. 3, pp. 395–401, Mar. 2008.

[190] J. Kang, D. S. Wilkinson, M. Jain, J. D. Embury, A. Beaudoin, S. Kim, R. K. Mishra, and A. Sachde, "On the sequence of inhomogeneous deformation processes occurring during tensile deformation of strip cast AA5754," *Acta Mater.*, vol. 54, no. 1, pp. 209–218, Jan. 2006.

[191] A. Pandey, A. S. Khan, E.-Y. Kim, S.-H. Choi, and T. Gnäupel-Herold, "Experimental and numerical investigations of yield surface, texture, and deformation mechanisms in AA5754 over low to high temperatures and strain rates," *Int. J. Plast.*, vol. 41, pp. 165–188, 2012.

[192] S. J. Hashemi, H. M. Naeini, G. Liaghat, R. A. Tafti, and F. Rahmani, "Forming limit diagram of aluminum AA6063 tubes at high temperatures by bulge tests," *J. Mater. Sci. Technol.*, vol. 28, no. 11, pp. 4745–4752, 2014.

[193] D. Li and A. Ghosh, "Tensile deformation behavior of aluminum alloys at warm forming temperatures," *Mater. Sci. Eng. A.*, vol. 352, pp. 279–286, 2003.

[194] J. Lemonds and A. Needleman, "Finite element analyses of shear localization in rate and temperature dependent solids," *Mech. Mater.*, vol. 5, no. 4, pp. 339–361, 1986.

[195] A. Staroselsky and B. N. Cassenti, "Combined rate-independent plasticity and creep model for single crystal," *Mech. Mater.*, vol. 42, no. 10, pp. 945–959, Oct. 2010.

[196] E. Cyr, M. Mohammadi, R. K. Mishra, and K. Inal, "A New Three Dimensional Thermo-Elasto-Viscoplastic Constitutive Model for FCC Polycrystals," in *TMS 2015*, 2015.

[197] T.-D. Nguyen, V.-T. Phan, and Q.-H. Bui, "Modeling of Microstructure Effects on the Mechanical Behavior of Ultrafine-Grained Nickels Processed by Severe Plastic Deformation by Crystal Plasticity Finite Element Model," *J. Eng. Mater. Technol.*, vol. 137, no. 2, p. 21010, 2015.

[198] B. L. Hansen, I. J. Beyerlein, C. a. Bronkhorst, E. K. Cerreta, and D. Dennis-Koller, "A dislocation-based multi-rate single crystal plasticity model," *Int. J. Plast.*, vol. 44, pp. 129–146, 2013.

[199] K. Inal, P. D. D. Wu, and K. W. W. Neale, "Finite element analysis of localization in FCC polycrystalline sheets under plane stress tension," *Int. J. Solids Struct.*, vol. 39, no. 13–14, pp. 3469–3486, Jun. 2002.

[200] Y. W. Chang and R. J. Asaro, "An Experimental Study of Shear Localization in Aluminum-Copper Single Crystals," *Acta Mater.*, vol. 29, pp. 241–257, 1981.

[201] U. F. Kocks and H. Mecking, “Physics and phenomenology of strain hardening: The FCC case,” *Prog. Mater. Sci.*, vol. 48, no. 3, pp. 171–273, 2003.

[202] Y. P. Varshni, “Temperature Dependence of the Elastic Constants,” *Phys. Rev. B*, vol. 2, no. 10, 1970.

[203] Y. Suzuki, V. R. Fanelli, J. B. Betts, F. J. Freibert, C. H. Mielke, J. N. Mitchell, M. Ramos, T. A. Saleh, and A. Migliori, “Temperature dependence of elastic moduli of polycrystalline β plutonium,” *Phys. Rev. B*, vol. 84, pp. 1–11, 2011.

[204] O. D. Slagle and H. A. McKinstry, “Temperature Dependence of the Elastic Constants of the Alkali Halides. I. NaCl, KCl, and KBr,” *J. Appl. Physics1*, vol. 38, 1967.

[205] R. Lowrie and A. M. Gonas, “Single-Crystal Elastic Properties of Tungsten from 24 ° to 1800 ° C,” *J. Appl. Phys.*, vol. 38, pp. 24–29, 1967.

[206] M. Arentoft, Z. Gronostajski, A. Niechajowicz, and T. Wanheim, “Physical and mathematical modelling of extrusion processes,” *J. Mater. Process. Technol.*, vol. 106, no. 1–3, pp. 2–7, Oct. 2000.

[207] R. A. Lebensohn, A. K. Kanjarla, and P. Eisenlohr, “An elasto-viscoplastic formulation based on fast Fourier transforms for the prediction of micromechanical fields in polycrystalline materials.,” *Int. J. Plast.*, vol. 32, pp. 59–69, 2012.

[208] H. F. Al-Harbi and S. R. Kalidindi, “Crystal plasticity finite element simulations using a database of discrete Fourier transforms,” *Int. J. Plast.*, May 2014.

[209] R. Abeyaratne and N.Triantafyllidis, “The Emergence of Shear Bands in Plane Strain,” *Int. J. Solids Struct.*, vol. 17, no. 12, pp. 1113–1134, 1981.

[210] L. Anand and W.A.Spitzig, “Initiation of Localized Shear Bands in Plane Strain,” *1Journal Mech. Phys. Solids*, vol. 28, pp. 113–128, 1980.

[211] Y. Wua, Y. Shena, P. Wu, K. Chen, Y. Yu, and G. He, “A two-step approach to predict shear band development with crystal plasticity finite element method (CPFEM),” *Int. J. Solids Struct.*, 2016.

[212] B. Langelier and S. Esmaeili, “The Effect of Zn Additions on Precipitation Hardening of Mg-Ca Alloys,” pp. 505–509, 2010.

[213] S. Pogatscher, H. Antrekowitsch, H. Leitner, T. Ebner, and P. J. Uggowitzer, “Mechanisms controlling the artificial aging of Al-Mg-Si Alloys,” *Acta Mater.*, vol. 59, no. 9, pp. 3352–3363, 2011.

[214] J. Buha, R. N. Lumley, and A. G. Crosky, “Secondary ageing in an aluminium alloy 7050,” *Mater. Sci. Eng. A*, vol. 492, no. 1–2, pp. 1–10, 2008.

[215] O. Engler and J. Hirsch, “Texture Control by Thermomechanical Processing of AA6xxx Al-Mg-Si Sheet Alloys for Automotive Applications - A Review,” *Mater. Sciance Eng. A*, vol. 336, no. 1–2, pp. 249–262, 2002.